UNIVERSITY OF CALIFORNIA, SAN DIEGO

High Power Metal-Contact and Capacitive Switches with Stress Resilient Designs

A dissertation submitted in partial satisfaction of the
requirements for the degree
Doctor of Philosophy

in

Electrical Engineering (Electronics Circuits and Systems)

by

Hosein Zareie

Committee in charge:

Professor Gabriel M. Rebeiz, Chair
Professor James Buckwalter
Professor Gert Cauwenberghs
Professor William Hodgkiss
Professor Daniel Sievenpiper

2013

The dissertation of Hosein Zareie is approved, and it is acceptable in quality and form for publication on microfilm and electronically:

_____

_____

_____

_____

_____

Chair

University of California, San Diego

2013

DEDICATION

To my Mother and Father Sakineh Esmaeilian and Mahmoud Zareie

To my Wife Asma Raoufizadeh

To my Brothers Ehsan and Milad

To my Grandmothers Bibi and Fatemeh

To my Aunt and Uncle Mahboobe and Mohammadreza

and

To my Whole Family

TABLE OF CONTENTS

LIST OF FIGURES

LIST OF TABLES

ACKNOWLEDGEMENTS

I would like to thank my advisor Prof. Gabriel M. Rebeiz for giving me an opportunity to join his research group and guiding me throughout my PhD studies. I worked with Professor Rebeiz on several RF-MEMS projects and also on RFIC projects alongside state-of-the art facilities and technology, accomplished co-workers, and knowledgeable faculty, all of which has equipped me with the tools to succeed. Due to his strong support and guidance, I could finish my Ph.D. studies in about three and a half years, and publish several papers in prestigious journals and conferences. It has been a great pleasure to know him and work with him, and it has been a great honor to be one of his students.

Next, I would like to thank my dissertation committee members, Professor Daniel Sievenpiper, Professor James Buckwalter, Professor Gert Cauwenberghs and Professor William Hodgkiss for their time, interest, and valuable remarks.

Also, I would like to thank my previous advisors, Professor Shoaei and Professor Mohajerzadeh, for their valuable support, advice, and encouragement.

Next, I would also like to express my gratitude to the staff of the Nano3 cleanroom facility at UCSD for all of the support that they have given me, including, Bernd Fruhberger, Larry Grissom, Ryan Anderson, Sean Parks, Xuekun Lu, and Maribel Montero. Also, I would like to thank the undergraduate interns who met me at odd hours of the night for dicing and SEM support.

Additionally, I must thank my fellow graduate students for their support and friendship. My thanks go to all of the TICS group including Samet Zihir, Mehmet Uzunkol, Yang Yang, Michael Chang, Chris Galbraith, Carson White, Byung-Wok Min, Sang-June Park, Jeonggeun Kim, Balaji Lakshminarayana, Mohammad El-Tanani, Tiku Yu, Sangyoung Kim, Kwangjin Koh, Isak Reines, Jason May, Alex Grichener, DongWoo Kang, Jung-Mu Kim, Yusuf A. Atesal, Berke Cetinoneri, Ramadan Alhalabi, Chirag Patel, Kevin Ho, Jennifer M. Edwards,Woorim Shin, Donghyup Shin, Ozgur Inac, Yi-Chyun Chiou, Chih-Chieh Cheng, Rashed Mahameed, Yu-Chin Ou and many thanks to Hojr Sedaghat Pisheh.

Completing my PhD. was not possible without help and sacrifice of my parents . My Mother Sakineh Esmaeilian was always supporting me through-out my studies and she has been a wonderful mother to me. My father Mahmoud Zareie Khabjani was always with me through the difficult times in my life and is an amazing father. I am

really thankful to my parents and I owe everything to them. I also want to thank my brothers Ehsan and Milad for all the good time and memories that we share together. Finally I want to thank all my family which was always supporting and encouraging me to complete my studies. Special thanks to my grandfather, my aunt, my uncle and to my grandmothers who always kept me in their prayers. Without my family, this work would have never been possible, and I would like to express my sincere thanks to them.

I would also like to thank my close-friend, Abbas Rahimi, for all his help and support, and my friends in the Islamic Educational Center of San Diego (IECSD) for making my life in San Diego more enjoyable.

Chapter 2 is mostly a reprint of material published in IEEE Transactions on Microwave Theory and Techniques, 2013; Hosein Zareie and G. M. Rebeiz. The chapter also includes some material from IEEE MTT-S International Microwave Symposium Digest, 2012; Hosein Zareie and G. M. Rebeiz. In both cases, the dissertation author is the primary author of the source material.

Chapter 3 is mostly a reprint of material submitted to IEEE Transactions on Microwave Theory and Techniques, 2013; Hosein Zareie and G. M. Rebeiz. The dissertation author is the primary author of the source material.

Chapter 4 is mostly a reprint of material submitted to IEEE Transactions on Microwave Theory and Techniques, 2013; Hosein Zareie and G. M. Rebeiz. The dissertation author is the primary author of the source material.

Chapter 5 in part is currently being prepared for submission to the IEEE Microwave and Wireless Components Letters, 2014; Hosein Zareie and Gabriel M. Rebeiz. The dissertation author is the primary author of this material.

Hosein Zareie
San Diego, CA
November 22, 2013

VITA

2006	B. S. in Electrical Engineering, Amir Kabir University of Technology (Tehran Polytechnic), Tehran, Iran
2009	M. S. in Electrical Engineering, University of Tehran, Tehran, Iran
2013	Ph. D. in Electrical Engineering (Electronics Circuits and Systems), University of California, San Diego

PUBLICATIONS

H. Zareie and G. M. Rebeiz,"High power RF MEMS switched capacitors using a thick metal process," *IEEE Transactions on Microwave Theory and Techniques*, vol. 61, no. 1 , pp. 453−463, Jan. 2013.

H. Zareie and G. M. Rebeiz,"Compact, High-Power SPST and SP4T RF MEMS Metal-Contact Switches," Accepted to *IEEE Transactions on Microwave Theory and Techniques*, November 2013.

M. A. Philippine, H. Zareie, O. Sigmund, and G. M. Rebeiz,"Experimental Validation of Topology Optimization For RF MEMS Capacitive Switch Design," *Journal of Micro Electro Mechanical Systems (JMEMS)*, vol. 22, no. 6, pp. , December 2013.

H. Zareie and G. M. Rebeiz,"High power ($>$ 10 W) RF MEMS switched capacitors," *IEEE Int. Microwave Symposium*, pp. 1-3, Montreal, Canada, June 2012.

M. A. Philippine, H. Zareie, O. Sigmund, G. M. Rebeiz, T. W. Kenny,"Topology Optimized RF MEMS Switches," Int. Conference on Solid-State Sensors, Actuators and Microsystems, pp. 2477-2480, Barcelona, Spain, June 2013.

ABSTRACT OF THE DISSERTATION

High Power Metal-Contact and Capacitive Switches with Stress Resilient Designs

by

Hosein Zareie
Doctor of Philosophy in Electrical Engineering (Electronics Circuits and Systems)
University of California San Diego, 2013
Professor Gabriel M. Rebeiz, Chair

This dissertation presents the design, fabrication and measurements of stress tolerant RF MEMS switches with high power handling and reliability. RF MEMS switched capacitors are developed that are capable of handling >10 W of RF power under hot switching conditions. A capacitance ratio of 5-7 has been achieved with high reliability and minimal dielectric charging. Also the Q of these devices was measured to be > 80 at 10 GHz in the maximum capacitance state.

SPST (single-pole single-throw) and SP4T (single-pole four-throw) RF MEMS metal-contact switches with high power handling and reliability have also been developed. The design is based on circular cantilevers that are anchored at the center and are attached together using a radial arc. This provides a compact SPST switch with multiple contact points and can easily be transformed to SPNT by dividing the membrane into several cantilevers each with its own actuation electrode. A power handling of > 10 W and > 2 W with high reliability has been measured for the SPST and SP4T switches, and with high reliability.

Furthermore the design of temperature resilient RF MEMS capacitive switches with the capacitance ratio of >30 have been achieved using the Raytheon process. The switch is used as a building block of different circuit configurations such as SPST, SPDT and a 2-bit X-band phase shifter with good performance.

Chapter 1

Introduction

1.1 MEMS

Micro-Electro-Mechanical-Systems (MEMS) devices have been developed for variety of applications such as chemical sensors, gas chromatography systems, pressure sensors, accelerometer gyroscope, etc.. (Fig. 1.1). These devices are fabricated using silicon micro-machining techniques and can be integrated with integrated circuits (ICs). The benefit of these microsystems compared to the conventional bulky counterparts are the low fabrication cost and very small feature size and sometimes better performances. The micro-electro-mechanical-systems used at high frequency are known as radio frequency (RF) MEMS and include the RF switches, varactors and inductors.

RF MEMS switches have excellent performance compared to the solid state switches and can be used in high frequencies due to their high isolation. Table 1 compares the performance of the RF MEMS switches with the solid state switches in terms of power consumption, reliability, power handling and switching time.

There are different actuation mechanisms for the MEMS switches: a) Electrostatic Actuation: This is the most commonly used and uses the electro static force that virtually consumes no DC power. b) Thermal actuation: This type of actuation usually uses the difference between the TCE (thermal expansion coefficient) of two different materials that are deposited on top of each other and can be moved by increasing the temperature. This actuation uses DC power to pass current through the resistive materials to generate the heat. c) Magnetic actuation: This type of actuation is based on the magnetic flux generated by using a current passing through a closed loop which

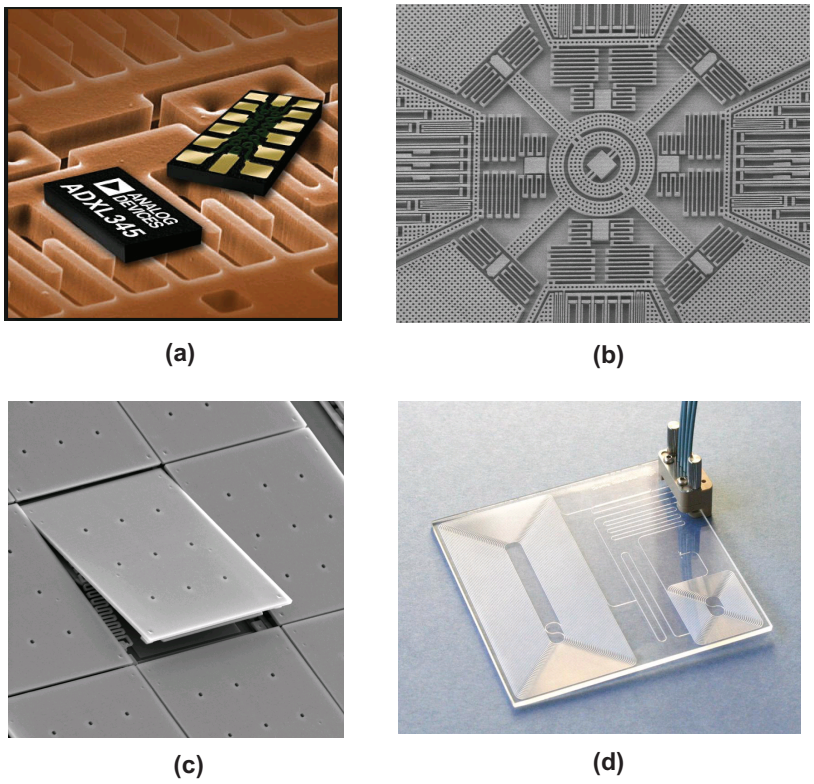

Figure 1.1: Different MEMS devices: (a) accelerometer sensor, (b) gyroscope, (c) micro mirror, (d) gas chromatography system.

Table 1.1: RF MEMS and solid state switches performances.

Parameter	RF MEMS	PIN	FET
Voltage (V)	20-80	+/-3-5	3-5
Current (mA)	0	3-20	0
Power consumption (mW)	0.05-0.1	5-100	0.05-0.1
C_{up} (fF)	1-10	40-80	70-140
Switching time	1-300μs	1-100ns	1-100ns
R_s (Ω)	0.5-2	2-4	4-6
Isolation	Very high	High	Medium
Loss (dB)	0.05-0.2	0.3-1.2	0.5-2.5
Power handling	<1	<10	<10
Third-order intercept point (dBm)	66-80	27-45	27-45

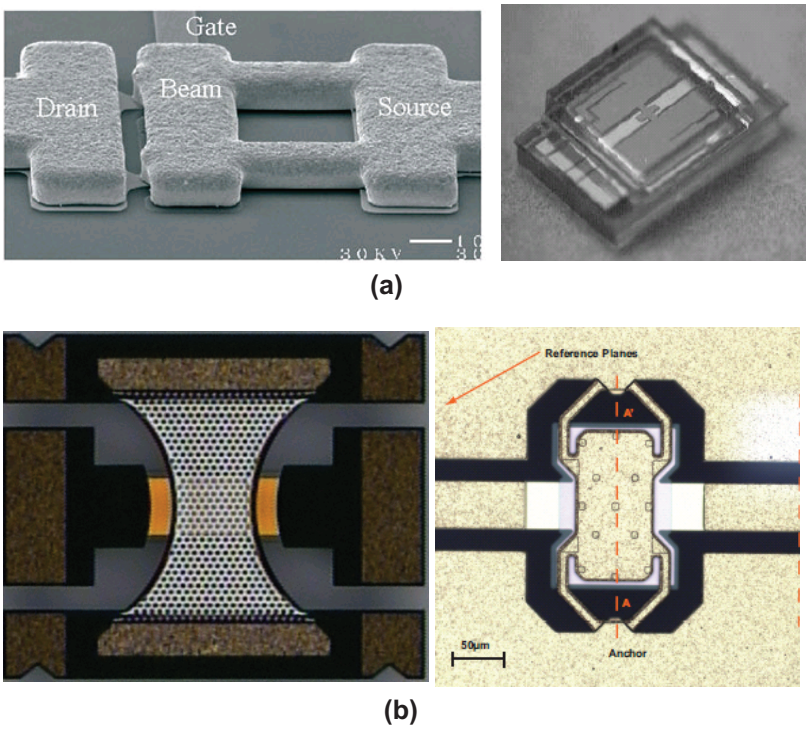

Figure 1.2: Different RF MEMS switches: (a) metal-contact switches, (b) capacitive switches.

applies force on a magnetic actuator. RF MEMS switches are divided in two different categories of metal-contact switches and capacitive switches (Fig. 1.2).

1.2 Metal-Contact RF MEMS Switches

Metal contact switches use an actuator to create an open/short circuit on the transmission line to act as a switch. These switches have superior performance in terms of linearity, power consumptions and insertion loss compare to micro-relays or solid-state switches [1–4]. They have a lot of potential for replacing conventional switches in switching networks and RF communication systems [5–8], and recently, several devices with excellent performance have been demonstrated [9–20]. Radant MEMS introduced a switch with high power handling capabilities [2, 4] and Omron demonstrated a switch with excellent reliability [9].

1.3 Capacitive RF MEMS Switches

Capacitive switches work by collapsing a MEMS beam on top of the dielectric which increases the capacitance between the RF line and the ground and therefore produces a near short circuit to the ground. The capacitive switches can be used in different categories such as an ON/OFF switch or switched capacitors which are employed for coarse tuning and also analog varactors which are used for fine tuning.

RF MEMS switched capacitors have been an active area for research over the past 10 years [1, 9, 21–23]. These devices have the potential to replace Schottky varactor diodes and switched capacitor banks using p-i-n diodes in tunable filters, antenna tuning networks, tunable antennas, and phase shifter circuits. They offer an acceptable capacitance ratio depending on the design (Cr=3-10), a very high Q (200-500 at 2-6 GHz), and are extremely linear devices generating very low IP2 and IP3 levels [1]. These devices have been developed for low and medium power applications, and recently integrated in a 0.18 μm or 0.35 μm CMOS back-end process [24–28].

1.4 Reliability and Power Handling

1.4.1 Metal-Contact Switches

The main challenges in RF MEMS metal contact switches are the reliability and power handling. Several devices have been recently developed with high contact and release forces using a 8-10 μm thick-metal process to provide lower contact resistance and improved reliability under high power conditions [11–13]. In order to increase the power handling capabilities, hard-metals contacts have been used which prevent the contact stiction under large current operation. Hard-metals such as Ruthenium have a high contact resistance under relatively low contact forces (< 0.2 mN) which increases the switch resistance and device insertion loss [1]. In order to reduce the insertion loss, a high contact force is required but this generally results in an increase in the device spring constant and also, an increase in the membrane thickness and area. One way to reduce the contact resistance is to provide multi-contact points in parallel which require less contact force per contact and still result in a low overall switch resistance. Using multiple contacts allows the fabrication of smaller size devices with relatively lower thickness and makes the switch compatible with silicon and GaAs MMIC metallization.

1.4.2 Capacitive Switches

The power handling of RF MEMS switched capacitors is first limited by the effective RMS voltage across the device in the up-state position that results in self-actuation, which occurs when the RMS RF voltage across the device is larger than the device actuation voltage [1]. For the special case of hot switching (continuous RF power), a limiting mechanism is "latching" of the MEMS beam in the down-state position, which occurs when the RMS RF voltage across the device is larger than the device release voltage [1]. Another limiting factor is the heat transfer characteristics of the RF MEMS device and its ensuing temperature rise both in the up-state and down-state positions under high power conditions [29–31]. One should also distinguish between high-voltage operation and high-power operation. Several MEMS devices are designed to handle high voltage levels using separate RF and DC electrodes [32], pull-up electrodes [33, 34], curled cantilevers [35, 36], or capacitive division [37], but they are all based on thin-metal structures and may not be able to handle the heat generation and temperature rise arising from high power operation. Mahameed et al. presented a temperature-

stable high-power switched-capacitor using the Chevron design with thick gold beams and angled actuators [38], and Palego et al. fabricated a switched capacitor also using a thick gold cantilever that can handle Watt-level power, but with a large drop in the release voltage for input power levels of > 2 W [39].

1.5 Description of the Dissertation

The goal of this dissertation is to design high power and reliable switches using RF MEMS technology. The switches have been designed and simulated using FEM methods and were optimized for RF performance. The switches were also fabricated using both thin metal and thick metal membranes and show excellent performances in terms of RF power handling and reliability.

Chapter 2 presents the design, simulation, fabrication and measurement of high power switched capacitors suitable for the tuning application(Cr=6.3). The design was optimized to achieve high power handling under hot switching conditions. The switch uses an angled anchor to achieve low sensitivity to both the residual stress and stress gradients. An array of dimples is used in order to minimize the contact area in the down-state position and reduce the dielectric charging.

Chapter 3 presents the design, simulation, fabrication and measurement of a stress gradient resilient structure which is capable of withstanding high stress-gradient values. The design employs four free cantilevers that are attached together using a central joint to minimize the deflection by increasing the stress gradients. The switch is also capable of handling high RF power >12 W under hot switching conditions.

Chapter 4 presents the design, simulation, fabrication and measurement of the high power RF MEMS metal contact switches using multiple contact points with medium contact force. The switch employs four cantilevers that are anchored in the middle and are tied together using a radial arc. The symmetry of the design creates virtual anchors along the symmetry planes which makes the device more resilient to the in-plane stress. The switch were implemented in SPST and SP4T configurations and show a high power handling of > 10 W and >2W for the SPST and SP4T switches respectively.

Chapter 5 presents the design, simulation and measurement of the temperature resilient RF MEMS capacitive switches using a thin metal membrane. The design uses a circular membrane that is anchored 90° apart and is separated from the anchors using 70° cutouts. The design was optimized to achieve low variations on the gap and the

spring constant by the increasing temperature due to the input RF power. Different circuit configurations such as SPST, SPDT and phase shifter are presented using the circular switch.

Chapter 6 presents the conclusions and future work.

Chapter 2

High Power RF MEMS Switch Capacitor Using a Thick Metal Process

2.1 Introduction

This chapter presents the design and characterization of a high-power RF MEMS switched capacitor. The switch is based on a 4 μm-thick metal plate and four symmetrical springs. The design has low sensitivity to residual stress and stress gradients. S-parameter measurements result in Cu=0.01 pF, Cd=0.63 pF (Cr=6.3), a power handling $>$ 10 W using hot switching conditions, and a switching time of $\sim$20 μs. The pull-down voltage (Vp = 50-55 V) and release voltage (Vr = 25-30 V) are stable to +/-4 V over 25-125°C. This chapter provides a complete thermo-mechanical design overview and simulations as well as measured RF characteristics. The switch is characterized at 10 GHz vs. power and temperature and can handle $\sim$10 W even under hot switching conditions. The design can be arrayed for N-bit switched-capacitor networks. Application areas are in high power phase shifters and tunable filters.

2.2 Switch Design

Fig. 5.1 presents a top view and cross-section of the high power switched-capacitor. The switch is fabricated using a 4 μm-thick electroplated gold beam and

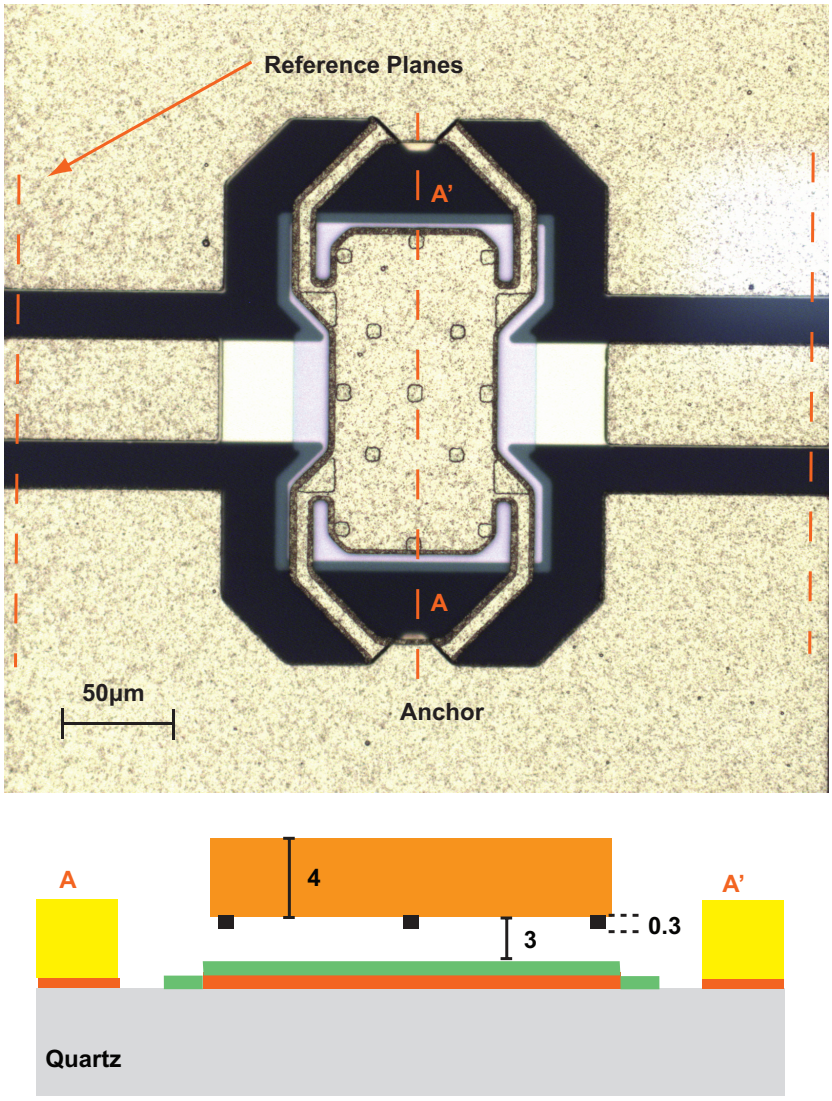

Figure 2.1: Top view and cross-section of the high power RF MEMS switched capacitor. All dimensions are in μm.

an air-gap of 3 μm. A number of 10×10 μm^2 gold dimples (0.3 μm thick) are used on the bottom of the beam to eliminate a direct contact with the dielectric and thus reduce the associated dielectric charging. The penalty paid is a decrease in the capacitance ratio, but most tunable filters, antenna impedance tuners and phase shifter designs require a capacitance ratio of 5-7 [40]. Therefore, this is an excellent compromise for tunable networks.

There are several important parameters in designing actuators for high-power RF applications. 1) efficient heat transfer to the anchor, 2) medium-value spring constant so as to result in Vp $\sim$ 50 V and a relatively high release voltage in order to prevent latching under high RF power, 3) a low inductance to ground ($<$ 15 pH) for 2-20 GHz operation, and last but not least, 4) low sensitivity to stress and temperature effects. The highest priority is given here to stability vs. process stress and stress gradient.

2.2.1 Mechanical Simulations

The switch consists of a rectangular membrane that is attached to two anchors using four symmetrical springs. The membrane stiffness (k=k_1+k_2) consists of a geometry dependent part (k_1) and a stress dependent part (k_2) [1]. In this design, the spring length was chosen to result in relatively low inductance to ground ($<$ 20 pH). Also, the Young modulus (E) of the electroplated gold is taken to be $\sim$35 GPa , which is lower than the standard values of sputtered gold as measured in [41]. Fig. 4.4 presents the deflection at the beam center together with the simulated stiffness and the k_2/k_1 ratio for different spring-anchor angles vs. residual in-plane stress values.

The 3-D FEM simulations show that the displacement is $<$ 0.2 μm for $\theta < 50^\circ$. For $25^\circ < \theta < 50^\circ$, the stiffness is almost the same for a stress $>$ 50 MPa. Also, the ratio of k_2/k_1 remains $<$ 50% for $\theta < 50^\circ$, which is important for stability vs. stress and temperature [1].

The simulated center plate profile for a residual stress of 100 MPa for different anchor angles and stress gradients are shown in Fig. 3.4. A stress gradient between +/-4 MPa/μm is typical for thick gold electroplated membranes in the UCSD process.

A large positive in-plane stress tends to deflect the membrane downwards, but a positive stress gradient tends to deflect the membrane upward, and this displacement is almost a linear function of the stress gradient [1]. As shown in Fig. 3.4, the displacement is less for +4 MPa/μm stress gradient by increasing θ but will be more for -4 MPa/μm.

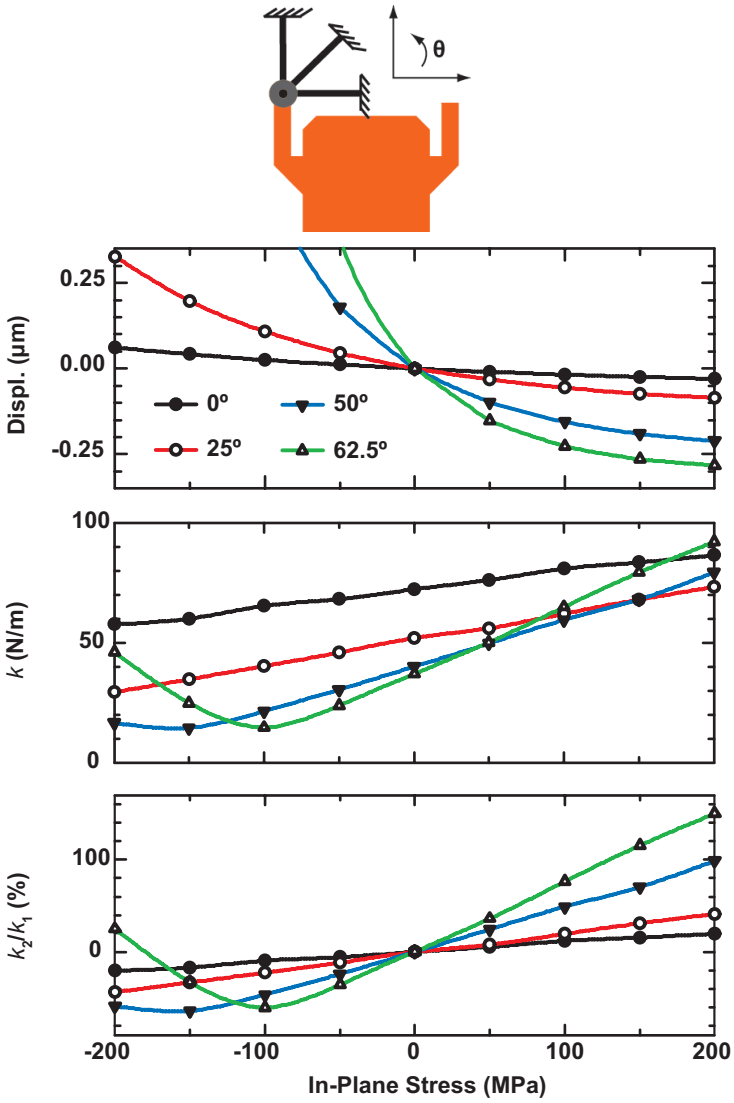

Figure 2.2: Simulated (a) center-plate displacement, (b) stiffness, and (c) k_2/k_1 vs. in-plane stress for different values of θ.

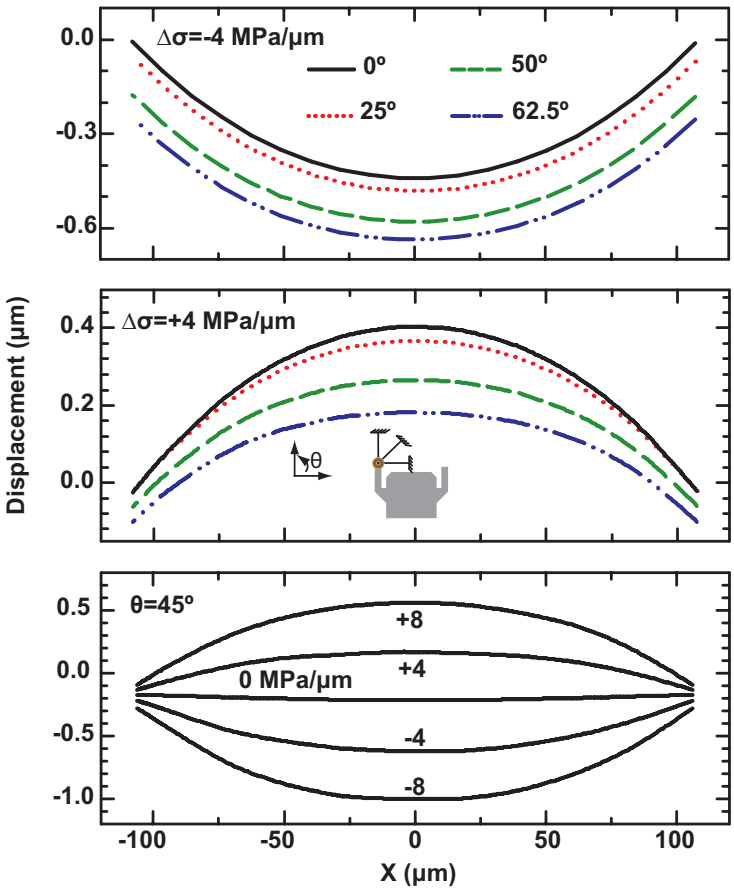

Figure 2.3: Simulated center plate profile vs. anchor angle and stress gradient for a residual stress of 100 MPa.

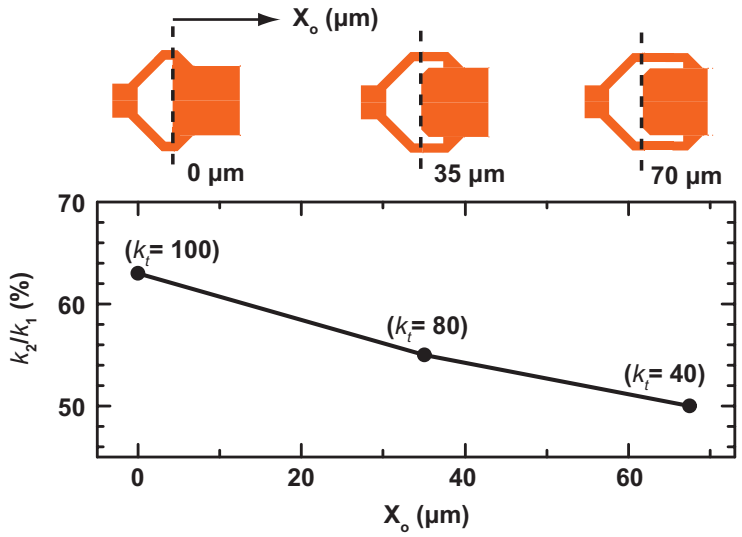

Figure 2.4: Simulated stiffness vs. X_o (spring attachment distance) for a residual stress of 100 MPa and $\Delta\sigma = 0$ MPa/μm.

On the other hand, k_2/k_1 also becomes high for large θ. The spring constant is weakly dependant on the stress gradient and is 60+/-5 (N/m) for stress gradients of -20 to +20 MPa/μm and for a wide range of θ values (25-50°). As seen from Fig. 4.4, increasing θ results in an increased k_2/k_1 and a larger displacement vs. in-plane stress. In order to balance the effects of the in-plane stress, the stress gradient variation and k_2/k_1, an anchor angle of $\theta = 45°$ is chosen in the final design.

The location of the spring-to-plate attachment is also optimized. In this case, the spring constant lowers as the spring attachments are moved to the center due to the change in the spring length, but also, k_2/k_1 decreases which is better for in-plane stress sensitivity (Fig. 2.4).

Fig. 2.5 presents the simulated center plate curvature for both X-Y directions of the membrane. As the attachments move toward the center, the membrane spring constant decreases and this results in more membrane deflection. X_o is therefore chosen to be 35 μm as a compromise between deflection, spring constant, and k_2/k_1 values. The final values are shown in Table 1.

2.2.2 Thermal Simulations

An increase in the ambient temperature lowers the in-plane stress for gold metal membranes since their thermal expansion coefficient (TCE) is higher than silicon

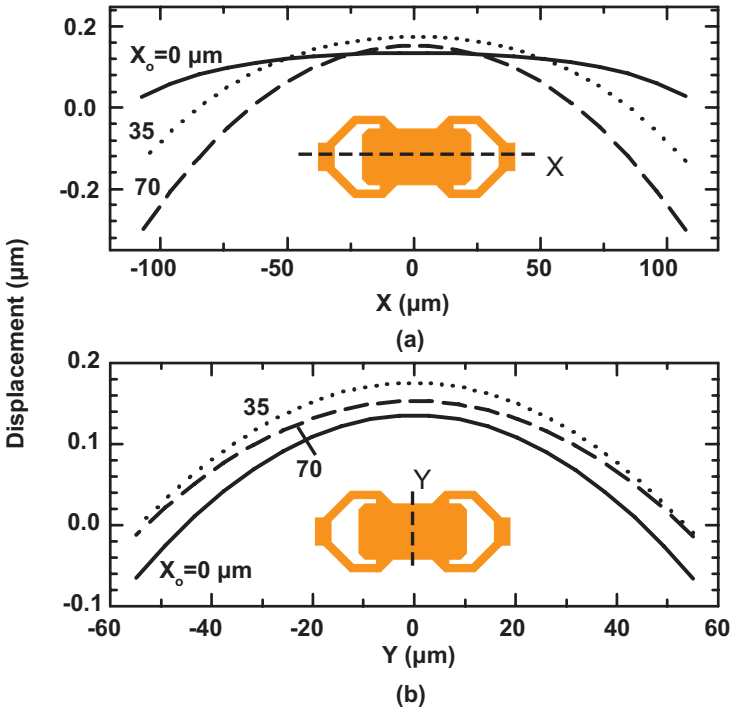

Figure 2.5: Simulated center place displacement in both X-Y directions for a residual stress of 100 MPa and $\Delta\sigma = +4$ MPa/μm.

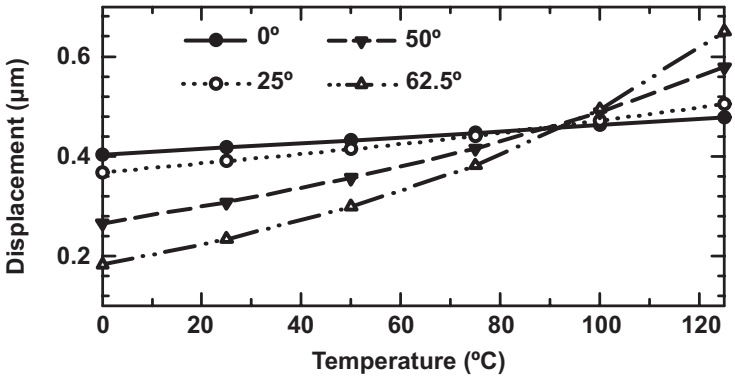

Figure 2.6: Simulated center-plate displacement vs. θ for a residual stress of 100 MPa.

or quartz substrates. The temperature change basically affects the k_2 part of the spring constant by changing the effective in-plane stress. In order to minimize the effect of temperature, the stress dependent part (k_2) should be smaller than the geometry dependent part (k_1) as chosen before.

Fig. 2.6 presents the simulated center-plate displacement vs. temperature for a residual stress of 100 MPa and no stress gradient. Since k_2/k_1 is higher for larger θ values, the center-plate displacement increases and shows more sensitivity to temperature as θ increases.

Fig. 2.7 presents the center-plate displacement vs. the temperature for $\theta = 45°$ and $\sigma = 100$ MPa for 0 and +/-4 MPa/μm stress gradients. For the zero stress gradient case, increasing the temperature results in lower in-plane residual stress and thus flattens the beam. At T > 100°C, the residual stress turns compressive and the displacement increases vs. temperature. For the case of +4 MPa/μm, the membrane displacement increases with temperature since the in-plane stress is decreasing and the effect of the stress gradient is more pronounced.

2.2.3 Thermal Simulations vs. RF Power

For high-power RF switches, the design should have a low thermal resistance so as to efficiently conduct the heat generated in the center plate to the anchors/substrate, and thus result in a low temperature rise on the membrane. Another important parameter is the minimization of non-uniform heating of the center plate, which can cause membrane deformation that will affect the spring constant and the resulting gap.

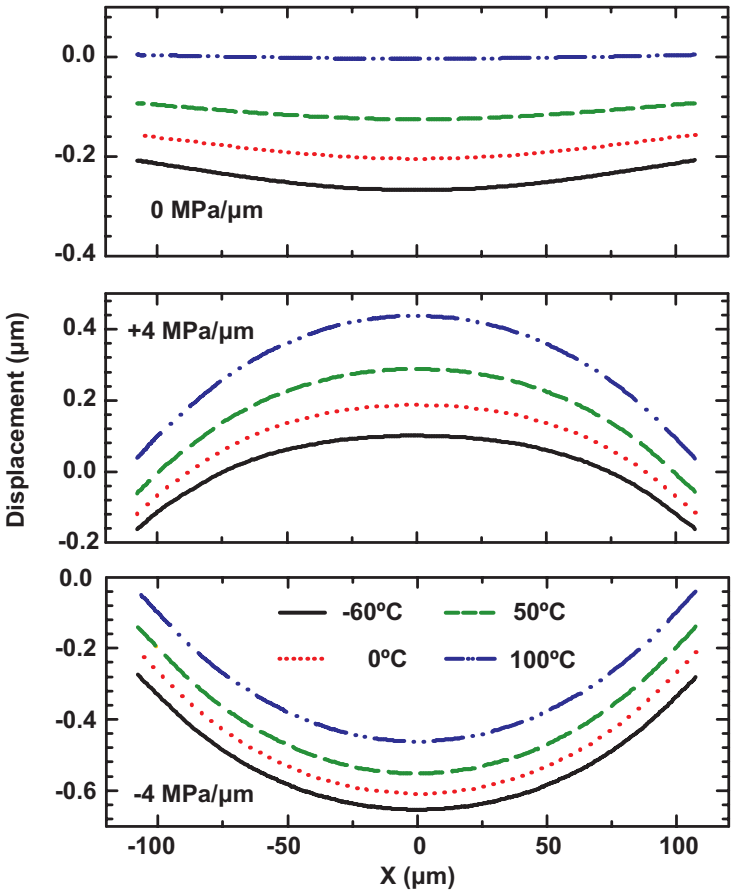

Figure 2.7: Simulated center plate profile for $\theta = 45°$ and a residual stress of 100 MPa, for 0 MPa/μm , +4 MPa/μm and -4 MPa/μm stress gradient.

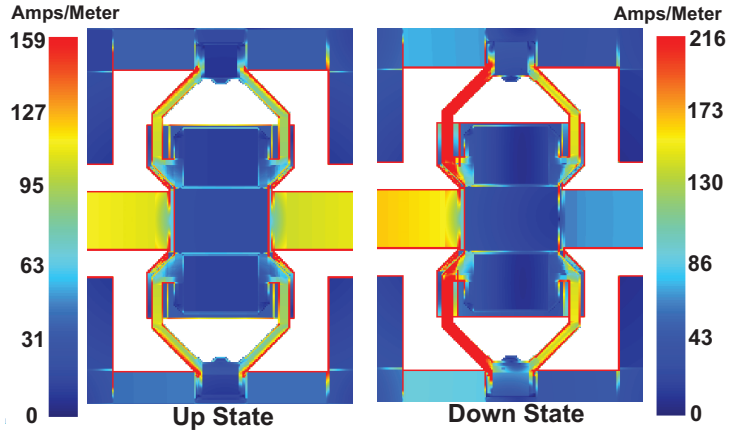

Figure 2.8: Simulated current distribution in the up and down-state positions.

The switched-capacitor is fabricated on a Quartz substrate in order to achieve a very low-loss, high-Q device. The switch is simulated vs. RF power using the method described in [31, 32, 42]. The RF power dissipated in the entire MEMS switch is first determined using simulated S-parameters as: Loss=1-$|S_{11}|^2$-$|S_{22}|^2$, and includes the loss in the transmission line, dielectric, substrate, and MEMS beam. To extract the loss in the MEMS beam alone, the switch is then simulated in a full-wave EM simulator (Sonnet) [43] with only the 4 μm-thick gold beam having a finite conductivity (σ_{beam} = 5×10^7 S/m), while all other metals and dielectrics are considered lossless. Sonnet also solves for the exact current distribution on the switch, both in the up-state and down-state positions (Fig. 5.4). The loss is then transferred into equivalent "heat strips" at the current concentration areas in the switch and the switch is simulated using Coventorware [44] to determine its temperature (Fig. 2.9). In the up-state position, and for the switch dimensions in Fig. 5.1 with Cu = 0.1 pF, simulations indicate that ~0.15% of the incident power is dissipated in the beam at 10 GHz, which results in a temperature increase of 30-115°C on a quartz substrate for an incident power of 5-20 W, respectively (Fig. 2.9). The thermal resistance for the membrane alone with anchors on an infinite heat sink is simulated to be 1100°C/W and increases to ~4000°C/W when the quartz substrate is taken into account. In the down-state position with Cd = 0.63 pF and a 0.3 μm gap between the RF line and the membrane, it is found that 0.28% of the power is dissipated in the beam and the increase in temperature is 15-65°C at 5-20 W, respectively. The thermal resistance for the membrane is simulated at 350°C/W and increases to ~1000°C/W with the quartz substrate.

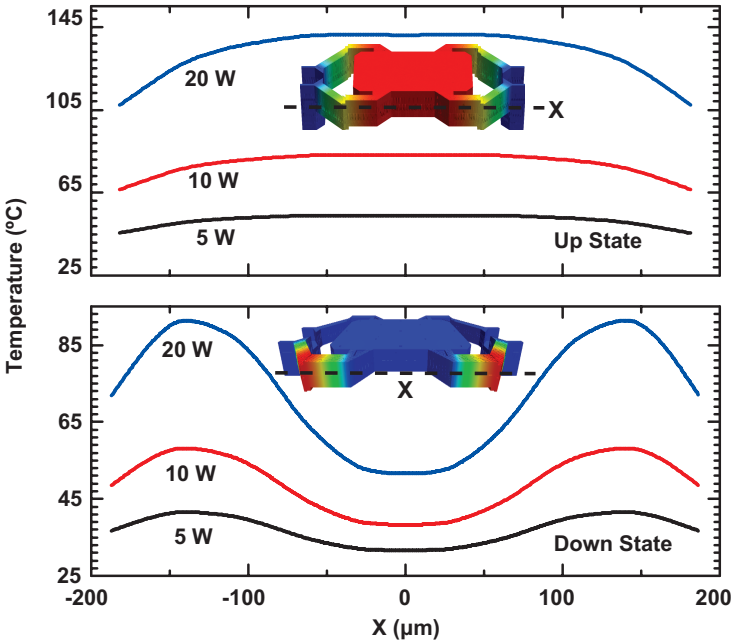

Figure 2.9: Thermal simulation for different RF powers in the up and down-state positions.

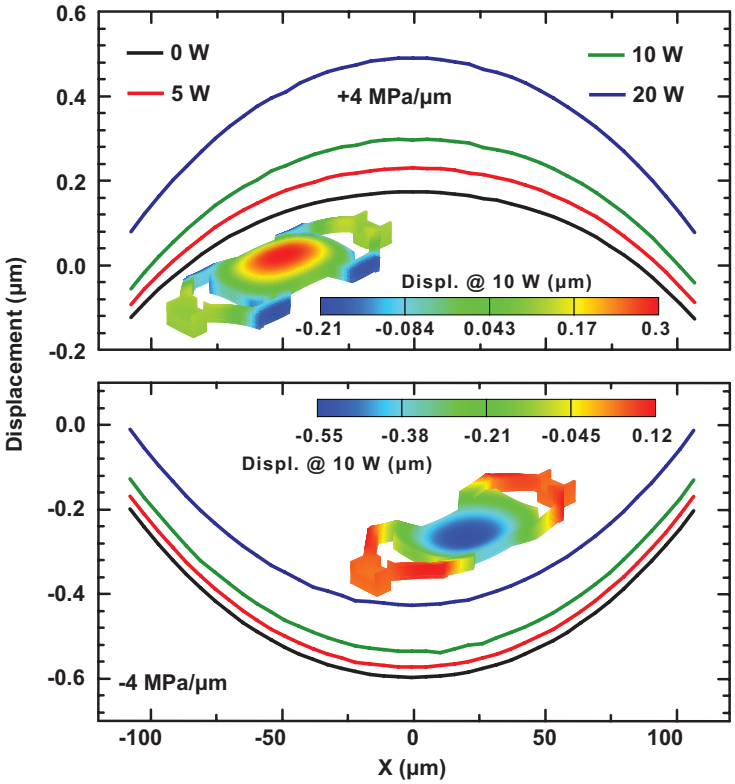

Figure 2.10: Simulated center plate profile in the up-state position for a residual stress of 100 MPa and a stress gradient of +/- 4 MPa/μm for different RF powers.

Table 2.1: Simulated parameters of RF MEMS switched capacitor.

Parameter	-4 MPa/μm	0 MPa/μm	+4 MPa/μm
k_1,k_2,k_t	47,24*,71	47,24*,71	47,24*,71
V_p (V)	42	47	52
V_r (V)	24	24	26
C_{up} (fF)	116	106	104
C_{down} (fF)	592	589	590
C_r	5.1	5.55	5.67
f_0 (kHz)	28.8	28.8	28.8
Q_m	2.04	2.04	2.04

*: Residual Stress=100 MPa.

The temperature rise in the down-state position is much lower than in the up-state position due to the array of 10×10 μm^2 dimples which reduce the switch thermal resistance by a factor of 4. Also, since the current is mostly concentrated at the input side of the membrane, the heating creates a non-uniform temperature profile across the membrane with the front-spring heating up to 50°C at 10 W and the back legs at room temperature. This has no effect on the down-state capacitance due to the large electrostatic force. The thermal time constants in the up and down-state positions are 258 μs and 82 μs, respectively. Fig. 2.10 shows the displacement of the beam for different incident RF powers. The membrane curvature increases by 0.1-0.3 μm for 10-20 W of input power due to the increase in temperature.

2.2.4 Vp, Vr and Capacitance Simulations

The actuation voltage is ∼45 V for a stress of 50 MPa and a stress gradient of 0 MPa/μm. The actuation voltage does not change much with inline stress and is 42-47 V for a residual stress of 0-100 MPa. The pull-in voltage of the switch is also simulated for the stress gradients of +/- 4 MPa/μm and varies by +/-5 V for any in-plane stress amount (Fig. 2.11). The design parameters result in the center part of the switch acting as a plate which is actuated to the down-state position in a planar fashion, thus improving the capacitance ratio. Fig. 3.7 presents the simulated capacitance vs. actuation voltage using Coventorware for various stress gradients.

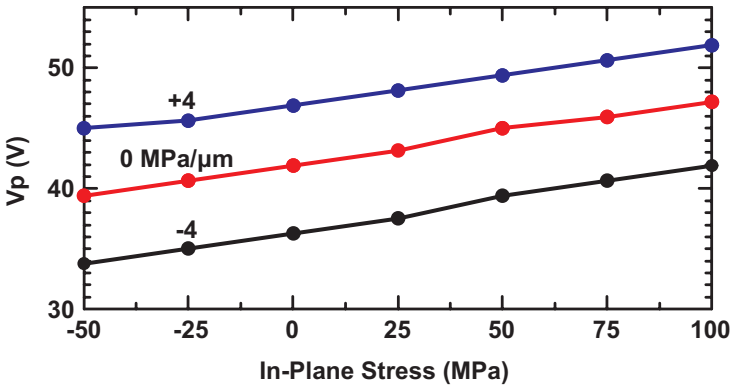

Figure 2.11: Simulated actuation voltage vs. different in-plane stresses for -4, 0, +4 MPa/μm stress gradients.

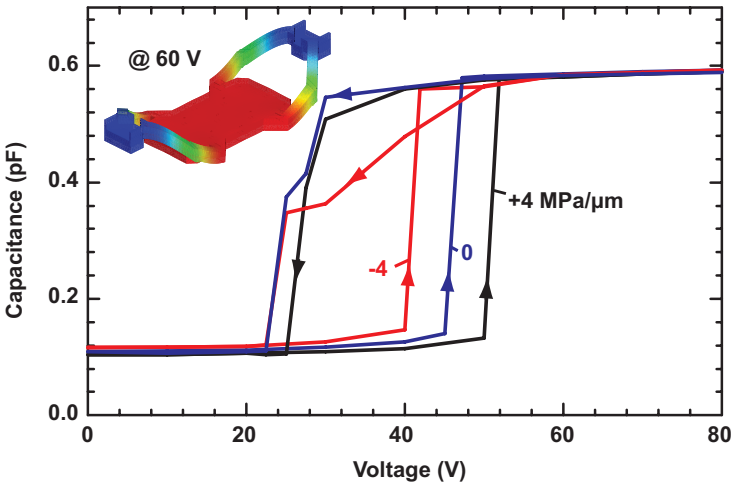

Figure 2.12: Simulated C-V curve for a residual stress of 100 MPa and different stress gradients/μm. The curve is given for both increasing and decreasing voltage.

The down-state capacitance does not change with the actuation voltage for V $>$ 60 V due to the flat membrane in the down-state position. Also, the down-state capacitance does not depend on the stress gradient, which results in a fixed capacitance ratio and makes it resilient to fabrication process variations. The switch is designed to handle a high RF power under hot switching conditions, and therefore, it is imperative to have an air gap in the down-state position, which increases the switch release voltage. The simulated release voltage is 21.8, 24.3, 26.2 V for an air-gap of 0.2, 0.3, and 0.4 μm, respectively. The associated down-state capacitance is 0.696, 0.583, 0.509 pF, resulting in a capacitance ratio of 5-7. As is well known, a fundamental compromise exists between the down-state capacitance and release voltage for switch designs having the same pull-down and RF electrodes: the higher the down-state capacitance, the lower the release voltage.

Table 1 presents the simulated mechanical and electrical characteristics of the high power switch. A change of +/-0.1 μm in the dimple height results in a down-state capacitance change of +/-16% for any stress gradient level. In the future, it may be better to use a grid of dielectric posts on the bottom electrode rather than dimples in the top plate for improved yield.

2.3 Fabrication

The switch is fabricated on a 500 μm quartz substrate using the UCSD fabrication process (Fig. 2.13). First, 0.5 μm of sputtered gold is deposited to form the bottom electrode (a).Then, 0.2 μm of Si_3N_4 is sputtered as a dielectric layer (b). A 2.7 μm PMMA layer followed by 0.3 μm of PMGI is used for the sacrificial layer (c). The dimples are first formed on the PMGI layer (d), and then a gold-plating seed layer is sputtered. Finally the beam is electroplated to a thickness of 4 μm (e) and the switch is then released in a critical point dryer system (f). Fig. 4.11 presents the 3-D profile using a Zygo interferometer. As is shown in Fig. 4.11, the membrane curvature is fitted to a stress gradient of -4 MPa/μm. The measured membrane thickness is 4.5 μm which increases the pull-down voltage.

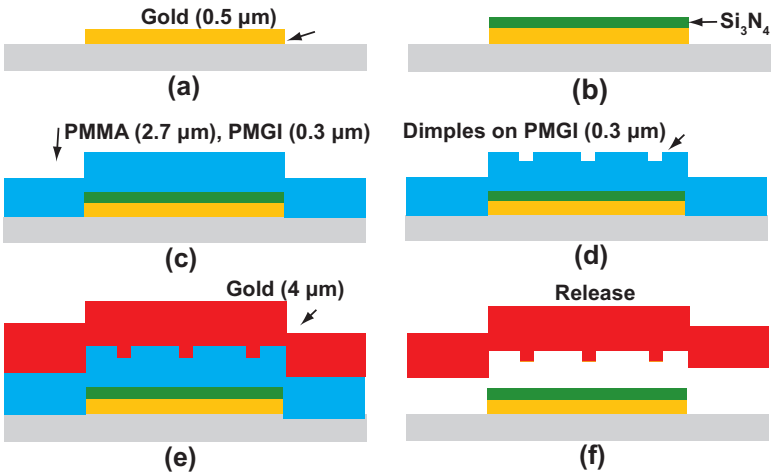

Figure 2.13: The UCSD thick-metal fabrication process.

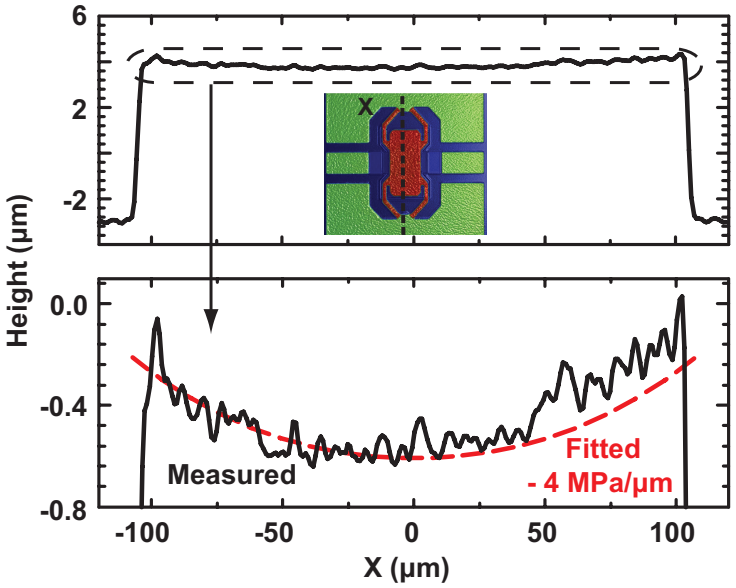

Figure 2.14: The fabricated switch profile done using Zygo measurements.

2.4 Measurements

2.4.1 S-Parameters

All measurements are done on unpackaged devices at room temperature and in a standard laboratory environment. The switch capacitance is determined after an SOLT calibration to the probe tips and by fitting the measured S-parameters to a transmission-line based on CLR switch model (Fig. 3.12). The extracted capacitances are Cu = 0.1 pF and Cd = 0.63 pF at 70 V (Cr = 6.3) and are in general agreement with simulations. The RF MEMS switch was also characterized using single port S-parameter measurements to determine its Q. The fitted Q is > 100 at 10 GHz in the down-state position without the transmission-line loss and shows very high ripple at f < 10 GHz. As is well known, S-parameter techniques result in a large error for Q > 80 [1], and a high-Q device should be measured using a loaded resonator technique for accurate values.

2.4.2 Vp, Vr and C-V

Fig. 4.14 presents the measured pull-in and release voltage vs. temperature. The chuck temperature was increased every 25°C up to 125°C and then decreased to room temperature. The measured voltages agree well with simulations and vary by +/-4 V over a 100°C temperature range. As seen in Fig. 16a,b some devices had a +/-3 V change in Vp, and some had a +/-5 V change. Note that due to the dimples and the air dielectric in the down-state position, very little charging is observed even at 125°C. Also note that the pull-down voltage increased to 55 V due to the increased thickness of the membrane. Fig. 4.14 shows the measured C-V curve for 25°C and 85°C. As predicted, the up and down-state capacitance values > 60 V are not dependant on temperature. The measurement also shows a symmetrical C-V curve for both positive and negative voltages [45, 46].

2.4.3 f_0 , Q_m , Switching time

The mechanical resonant frequency and Q_m were measured using a low frequency modulation signal applied on top of the RF carrier. The results were fitted to a second-order system with f_0 = 28 kHz and Q_m = 1.8, and agree well with simulations (Fig. 2.17). The switching time vs. voltage is shown in Fig. 17b. The pull-in time (t_{on}) is defined as the time it takes for the diode detector signal to reach 90% of its final value.

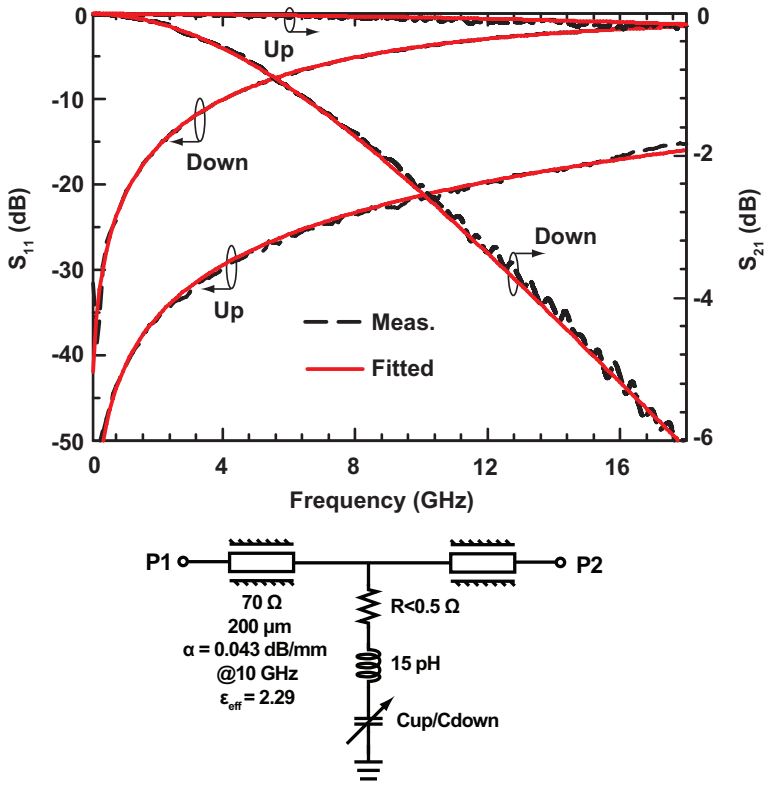

Figure 2.15: Measured and fitted S-parameters in a 2-port system, together with the CLR model.

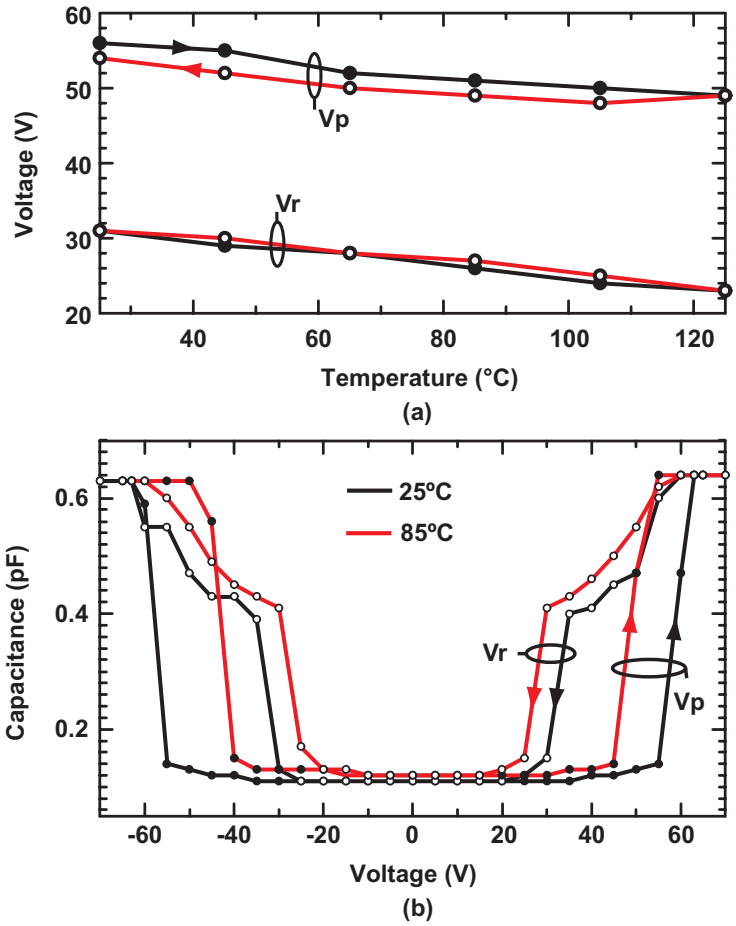

Figure 2.16: Measured pull-in and release voltages vs. temperature. (b) measured C-V curve for 25°C and 85°C.

The measured release time t_{off} is independent of the actuation voltage and is ~20 μs (not shown). The switching time can be approximated using the dynamic one dimensional (1-D) equation [1]:

$$m\frac{d^2x}{dt^2} + b\frac{dx}{dt} + kx + k_s x^3 = F_e + F_c \tag{2.1}$$

$$F_e = \frac{1}{2}\frac{\epsilon_0 A V^2}{(g_0 + \frac{t_d}{\epsilon_r} - x)^2} \tag{2.2}$$

$$F_c = \frac{C_1 A}{(g_0 - x)^3} - \frac{C_2 A}{(g_0 - x)^{10}} \tag{2.3}$$

where m = 1.75×10^{-9} kg is the membrane mass, b = 1.9×10^{-4} N s/m is the damping coefficient, k = 77 N/m, ks = 21×10^{12} N/m^3 is the nonlinear stretching spring constant [1], $g_0 = 3\times10^{-6}$ m is the gap, $t_d = 0.2\times10^{-6}$ m is the dielectric constant thickness, $\epsilon_r = 7$ is the dielectric constant and A = $26{,}400\times10^{-12}$ m^2. Fe is the electrostatic force and Fc represents the attractive van der Waals forces (first term) and the repulsive nuclear contact forces (second term) between the metal and dielectric layers. C1 = 10^{-80} Nm and C2 = 10^{-75} Nm^8 and are taken to improve the convergence of the numerical simulations. The above equation is solved using MATLAB [47] for the switching time vs. voltage for x = 0 to x = 2.7 μm (Fig. 2.17). The simulated release time is 20 μs which agrees well with measurements. The predicted Vp and Vr from the 1-D model are 48 V and 23 V, respectively. The difference between the 1-D model results and measurements is due to the model simplification especially in the down-state (release) condition since the device lifts off in a zipping fashion and not as a parallel plate.

2.4.4 RF Power Measurements

The power measurement setup is presented in Fig. 2.18 and employs a traveling-wave tube amplifier at 10 GHz. The cable and bias-T losses were normalized out of the measurements. At the output port, a back-to-back coax-to-waveguide transition was used to decouple the DC and step voltage leakages, which is then followed by an attenuator and a diode detector. The pull-in and release voltage vs. incident power at 10 GHz are shown in Fig. 2.18 (another switch was tested).

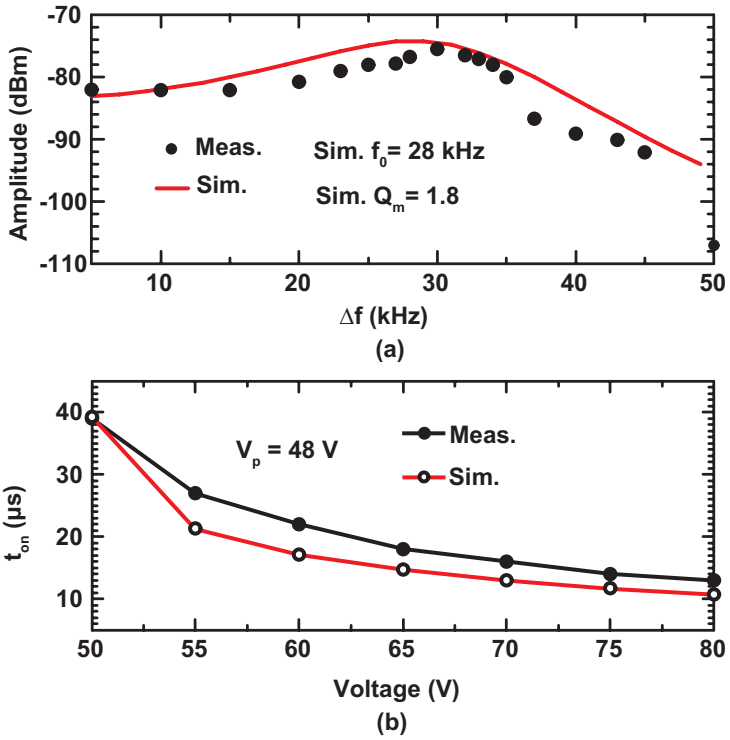

Figure 2.17: Measured f_0 and Q, and (b) measured and simulated switching time vs. voltage.

The pull-down and release voltage decrease by 8 V up to ∼10 W of incident power some due to temperature increase and some due to the additional force from the RF power. Note that the switched capacitor actuated well under hot-switching conditions since Vr remains > 15 V at ∼10 W. The switching time vs. power was also measured and simulated using the 1-D model (Fig. 2.19). As the input power increases, the amount of force applied by the RF signal to the membrane increases, and this adds an effective voltage to the DC actuation voltage and decreases the switching time. On the other hand, toff increases due to the latching of the switch in the down-state position by the force applied by the RF power. In the up-state position with S11 < -20 dB, the equivalent RMS RF voltage across the switch (Vrms) is added to the actuation DC voltage (Vact) and is:

$$V_{rms} = \sqrt{PZ_0} \tag{2.4}$$

$$V = \sqrt{{V_{act}}^2 + {V_{rms}}^2} \tag{2.5}$$

The second-order equation was solved with the same parameters mentioned before with x(t=0) = 0 m and x′(t=0) = 0 m/s. Also, as shown in Fig. 2.10, the gap increases by 50 nm for an input power of 10 W. In order to account for the effect of the heating on the air gap, an additional 5 nm was added to $g_0 = 3{\times}10^{-6}$ m for every 1 W increase in power. Fig. 19a presents the simulated 1-D model for the ton values vs. RF power. In the down-state position, the equivalent RMS RF voltage (Vrms) across the switch is:

$$V_{rms} = \sqrt{PZ_0}\,|1 + \Gamma| \tag{2.6}$$

$$\Gamma = \frac{\frac{1}{jC\omega} \,||\, Z_0 - Z_0}{\frac{1}{jC\omega} \,||\, Z_0 + Z_0} = 0.7\angle -45^o \; for \; C_d = 0.7pF \tag{2.7}$$

and V = Vrms since Vact = 0 for calculating the release time. The 1-D model simulation is done for the release time (t_{off}) with x(t=0) = -2.7 μm and x′(t=0) = 0 m/s vs. input RF powers and is shown in Fig. 19b. The difference between the simulation and the measurements for t_{off} is due to the simple 1-D model, which does not account for the bending of the membrane as it starts to separate from the bottom electrode.

2.4.5 Reliability Measurements

Reliability testing was done on unpackaged devices at room temperature and in a standard laboratory environment using the same approach in [48, 49] at 10 GHz with 100 mW of RF power (Fig. 2.20). The switches were actuated using a triangular pulse in the discharge mode for the first half hour to setup the initial pull-in and release voltage values and then they were actuated in the uni-polar mode. In the uni-polar mode, the switches were held in the down-state position for 97% of the period, released every few minutes for a very short time, and the pull-in and release voltages were recorded. This was done for two hours followed by the discharge mode for another half an hour. The reliability measurements exhibit excellent performance in terms of charging and creep. A change in the pull-in and release voltage of only 2 V is observed due to using dimples and eliminating the direct contact between the beam and the dielectric. The same measurements were repeated at 3 W of RF power and a noticeable effect on Vp is observed (Fig. 2.21). In this case, Vp changes from ∼55 V to 45 V after 2 hours of actuation in the uni-polar mode. The effect of the RF power on the reliability of capacitive RF MEMS switches and how it induces additional dielectric charging is now a topic of research [50, 51], and as of today, there are no clear explanations for this behavior. Note that the measurements were done under standard laboratory conditions, and packaged RF MEMS switches do not suffer from this extensive drift in Vp and Vr [50].

Another switch was actuated for 300 Million cycles using a saw-tooth bipolar pulse at 5 kHz for (8 hours) at 10 GHz with RF power of 100 mW (Fig. 2.22). Again, very little change in Vp is observed over 8 hours of periodic actuation.

2.5 Acknowledgments

Chapter 2 is mostly a reprint of the material as it appeared in the IEEE International Microwave Symposium, IMS 2012. and in the IEEE Transactions on Microwave Theory and Techniques, 2013; Hosein Zareie and Gabriel M. Rebeiz. The dissertation author is the primary author of this material.

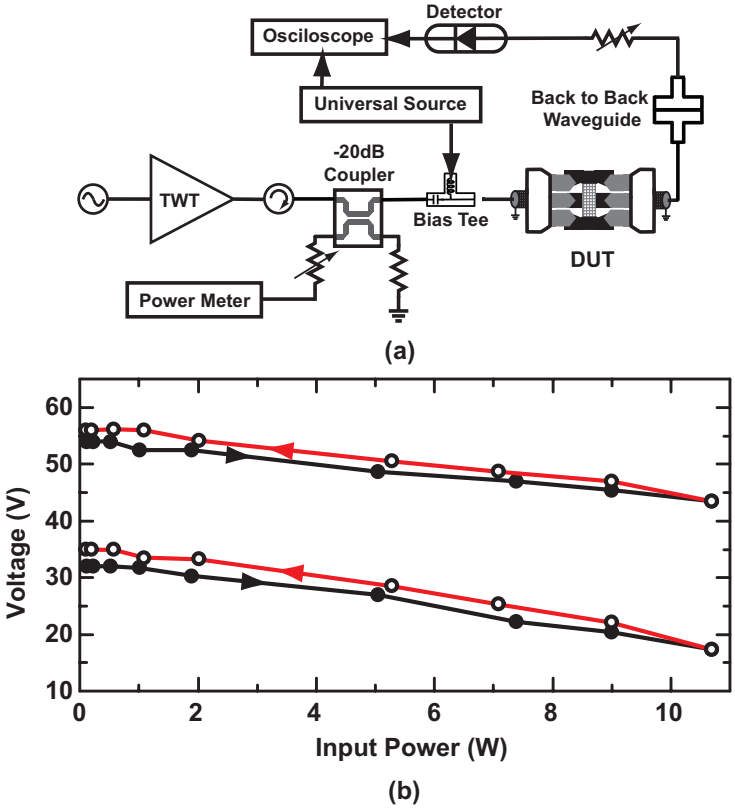

Figure 2.18: (a) High-power measurement setup, and (b), measured Vp and Vr vs. incident power level at 10 GHz.

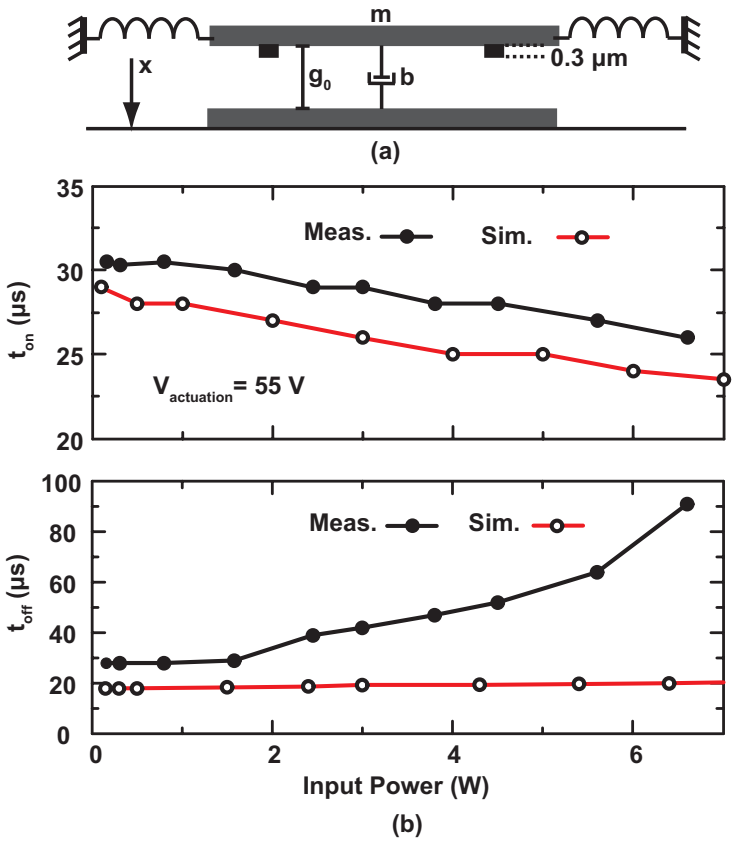

Figure 2.19: Measured t_{on} and t_{off} versus incident RF power. Simulations are obtained using a 1-D model.

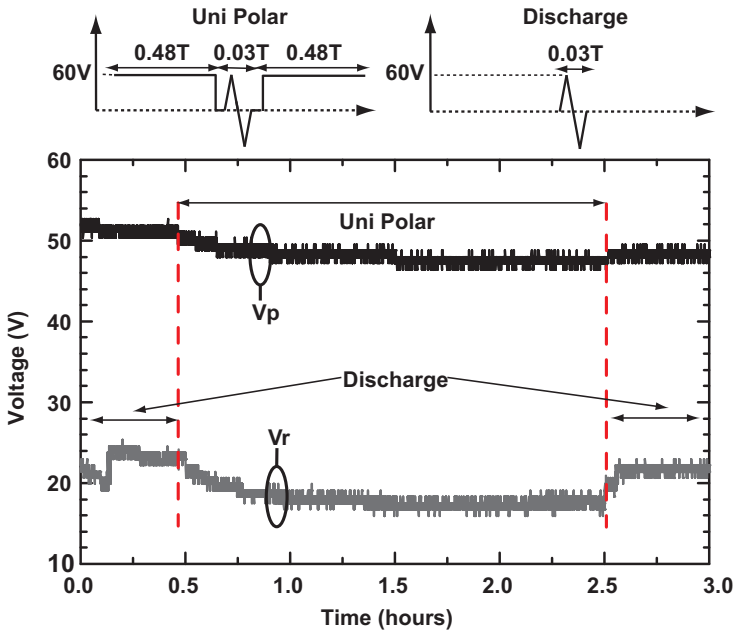

Figure 2.20: Measured Vp and Vr versus extended continuous actuation at 100 mW of RF power at 14 GHz.

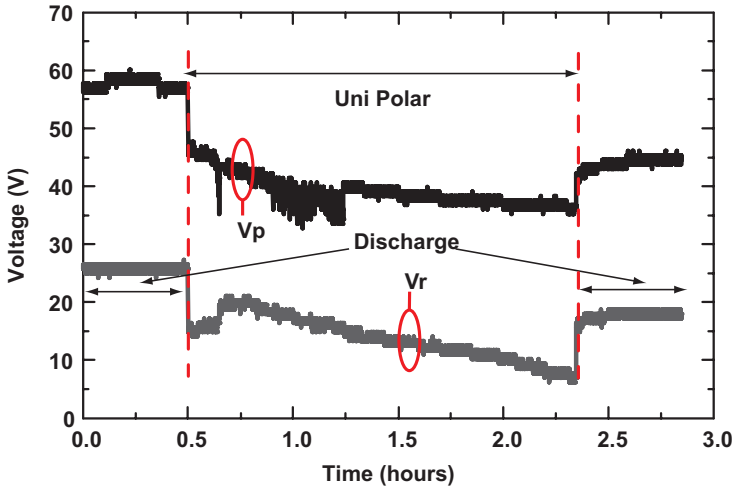

Figure 2.21: Measured Vp and Vr versus extended continuous actuation at 3 W of RF power at 14 GHz.

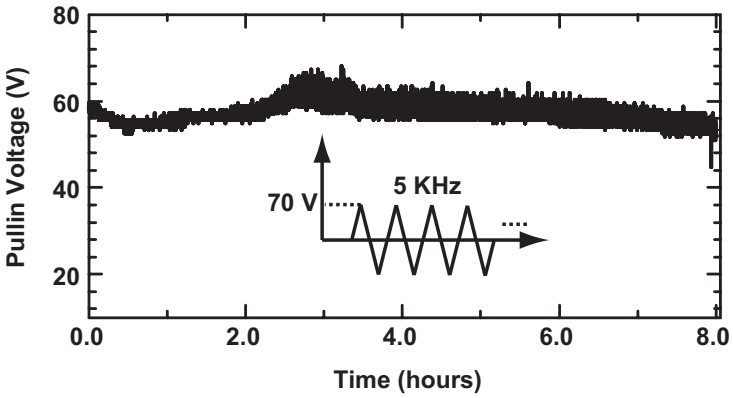

Figure 2.22: Reliability measurement for 300 million cycles (8 hours) at 10 GHz and 100 mW of RF power.

Chapter 3

A High Power Stress-Gradient Resilient RF MEMS Switch Capacitor

3.1 Introduction

There has been several attempts recently to build RF MEMS capacitive switches capable of handling an RF power in the 5-10 W level [39, 52]. These devices are suitable for tunable antennas, filters, and phase shifters used in defense and base-station applications. The power handling of RF MEMS capacitive switches is either limited by the effective RMS voltage across the device in the up-state position which results in a self-actuation condition, or latching in the down-state position for hot switching conditions [1]. Also, the design must be able to handle the temperature rise arising in the switch at high RF power without beam distortion. For high power designs, the voltage limitations are handled using a high Vp and Vr designs [52], separate RF and DC electrodes [32], capacitive division [37], curled/zipping cantilevers or a pull-up electrode which fixes the beam in the up-state position [34–36]. The temperature rise is generally handled using mechanical designs and thick electroplated beams for good heat transfer [38, 39, 52] or using large switches with separate RF and DC electrodes to direct the RF current to the anchors and not through the switch [32]. This chapter presents a novel high-power switch which is based on four cantilevers with a central joint (Fig. 5.1).

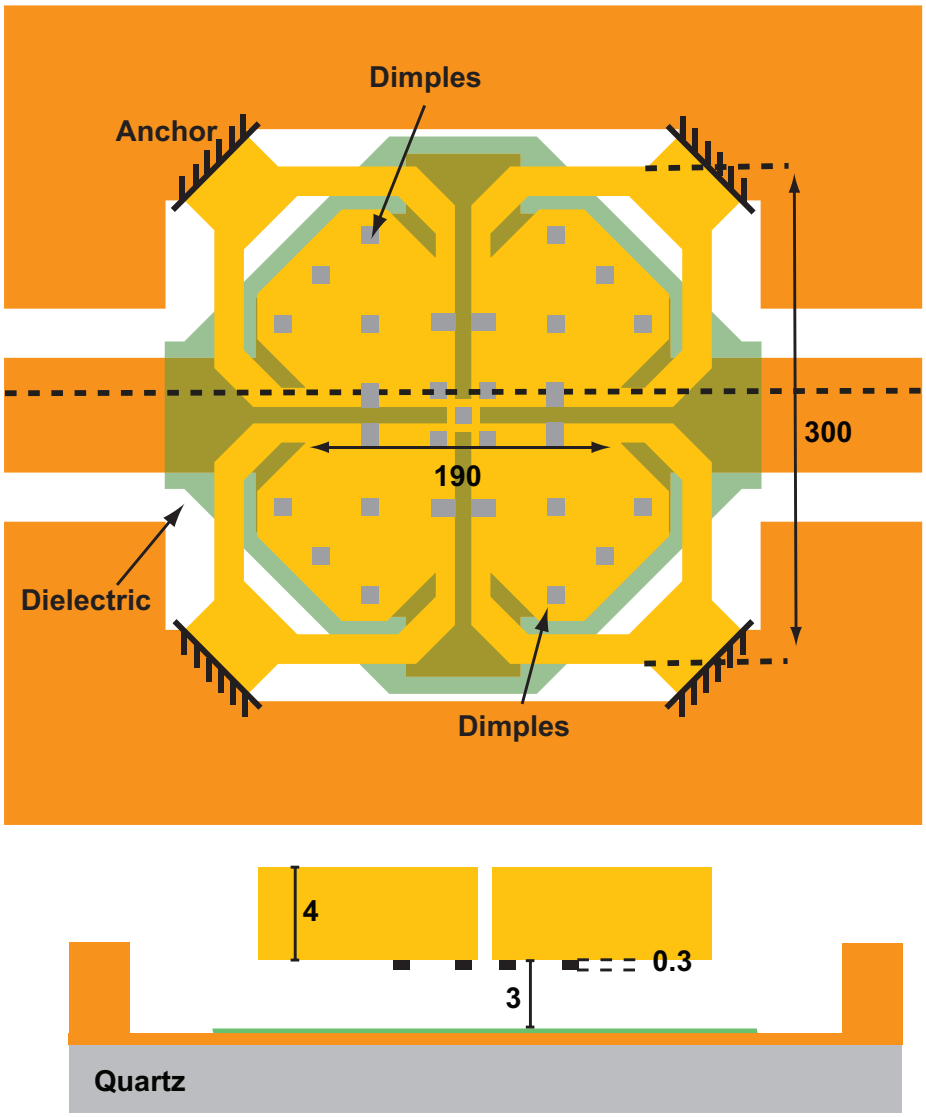

Figure 3.1: Top view and cross-section of the high power RF MEMS switched capacitor. All dimensions are in μm.

Mechanical analysis indicates that the design is very tolerant to stress gradients and results in a near constant Vp and Vr vs. temperature. It can also handle a large amount of RF power and temperature rise without beam distortion. The switch is characterized at 10 GHz and can handle 12 W under hot switching conditions.

3.2 Switch Design

The RF MEMS switch consists of 4 identical cantilever beams placed at the four corners of a square and each with its own set of anchor springs. However, in this design, the four beams are tied together at the center using a central joint. As will be seen below, this result in high stability to stress gradients since the cantilever tips are not floating but are anchored together with opposing moments resulting from stress gradients. The switch is fabricated using a 4.5 μm gold electroplated membrane with a 3 μm gap. The gap is chosen to be 3 μm so as to obtain a relatively high capacitance ratio. Also, 0.3 μm dimples are used in order to prevent the membrane from collapsing on the bottom electrode and this reduces the dielectric charging effect and greatly improves the switch reliability (at the expense of reducing the down-state capacitance).

3.2.1 Mechanical Simulations

Cantilevers are insensitive to bi-axial stress but are very sensitive to stress gradients due to their free-end condition. In fact, the tip displacement under stress gradient is proportional to L^2 where L is the cantilever length. One way to reduce the effects of the stress gradient is to tie four cantilevers instead of the full plate together using a central joint as shown in Fig. 3.2. The stress gradient tends to curl the cantilever beams upward or downward for positive or negative stress gradients. This creates opposite moments at each cantilever section, and in turn, tends to deflect the center joint in opposite directions. However, the smaller the joint and cantilever section sizes, the lower the radius of the curvature and overall displacement. The effect of the central joint on the switch spring constant and k_2/k_1 ratio is simulated using ANSYS 3-D software for a cantilever beam size of 190 μm (k_1 is the spring constant due to geometry with zero biaxial stress, and k_2 is the spring constant due to biaxial stress [1]). The curved anchors and their attachment to the cantilever beam are designed for stability vs. temperature as described in [52] (Fig. 3.2).

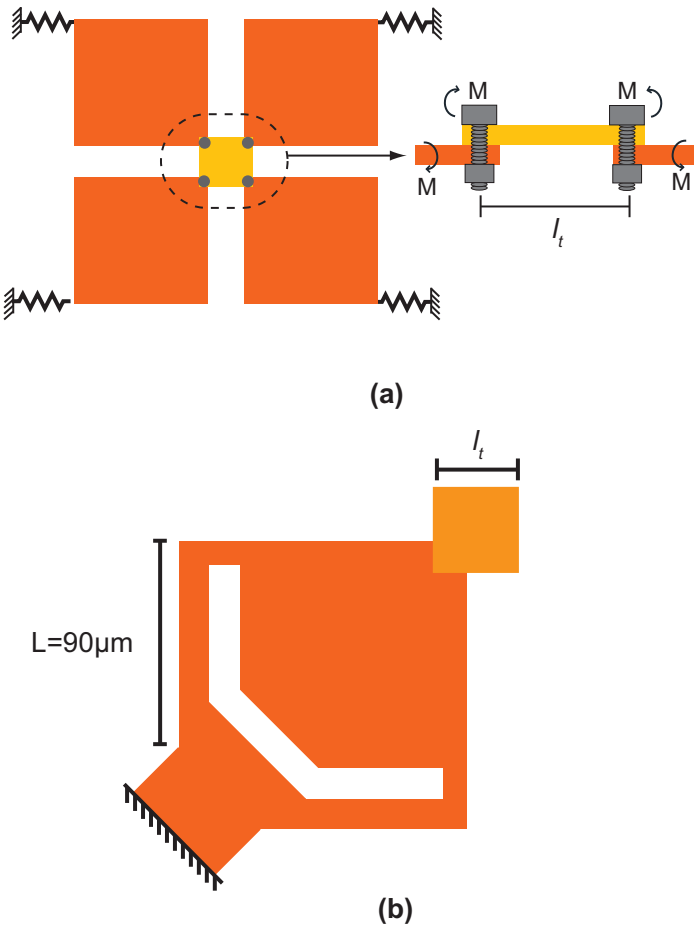

Figure 3.2: (a) Beam and joint configurations for the RF MEMS switch, (b) curled anchor topology, (c) internal bending moment of single element.

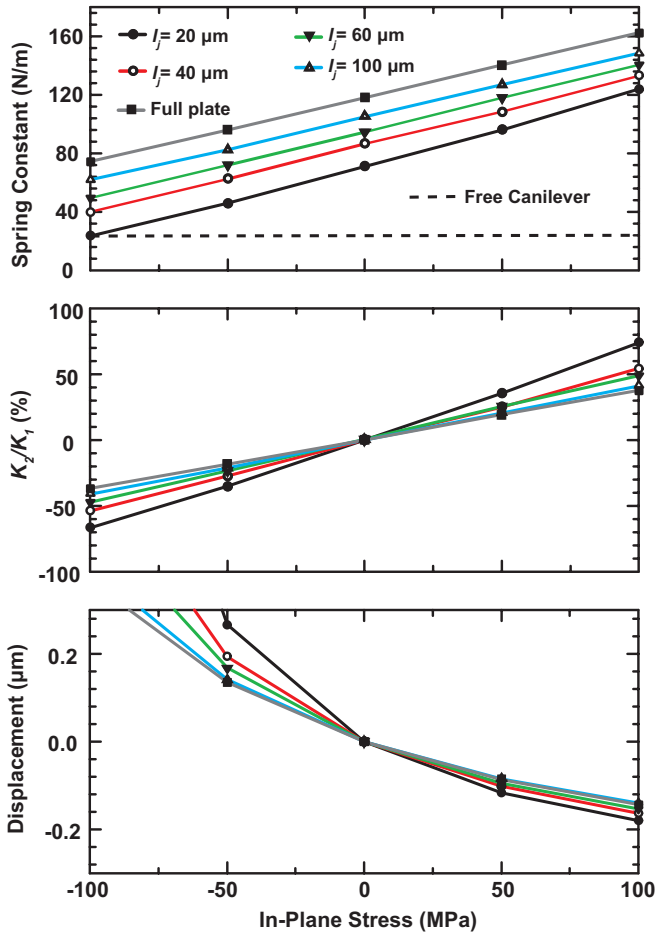

Figure 3.3: Simulated spring constant, center displacement, and k_2/k_1 ratio vs. in-plane stress for different joint dimensions.

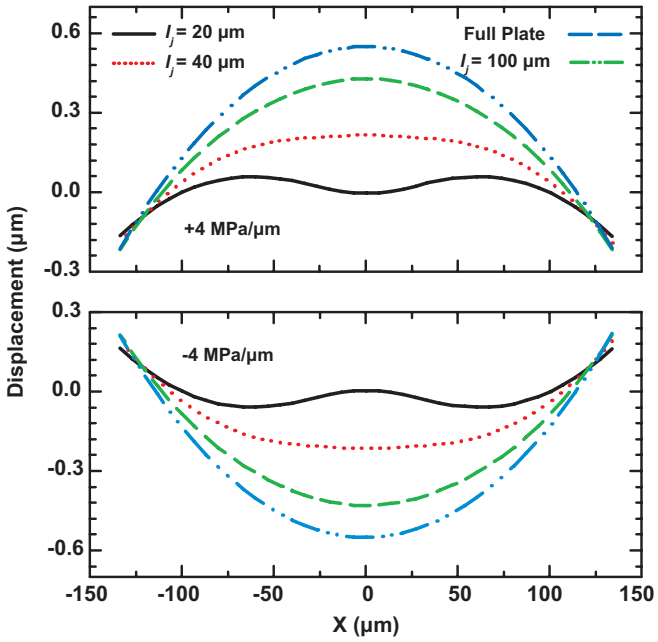

Figure 3.4: Simulated beam displacement for a biaxial stress of 0 MPa vs. different joint dimensions and stress gradient of +/- 4 MPa/μm.

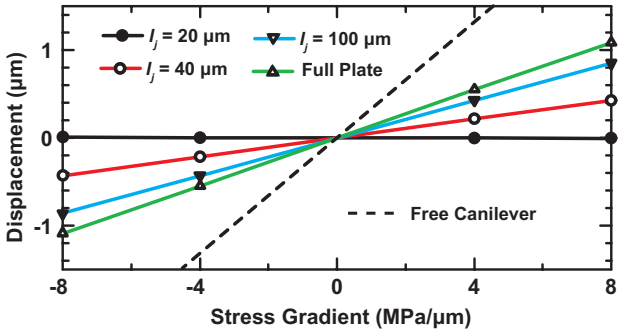

Figure 3.5: Simulated center displacement vs. stress gradient for different joint dimensions under zero in-plane stress.

Fig. 4.4 presents the spring constant, displacement at the center, and k_2/k_1 ratio vs. in-plane stress for different joint dimensions (l_j = 20-190 μm). Simulations are done for a gold beam with E = 35 GPA and υ = 0.4 [41]. Each cantilever is 90 μm long and note that for l_j = 190 μm (full-plate condition), the 4 cantilevers appear as a single square membrane and therefore has the highest spring constant and largest k_2/k_1 component.

The simulations show that the central joint does not have a significant effect on the center displacement vs. biaxial stress, but has a near-linear effect on its spring constant. Also, k_2/k_1 remains $<$ +/-50% for l_j = 20-60 μm for a biaxial stress of +/-100 MPa. A stress range of +/-100 MPa is taken since the electroplated gold at UCSD has a measured stress of ~50-100 MPa and a stress gradient of +/- 4 MPa/μm. Fig. 3.4 presents the center-plate displacement profile versus various joint dimensions and stress gradients. The full-plate design (l_j = 190 μm) results in the most deflection at the center, while l_j = 20-40 μm result in minimal center-plate deflection. The simulated displacement at the joint center versus stress gradient for zero biaxial stress is shown in Fig. 4.5. It is clear that l_j needs to be chosen as small as possible in order to reduce its curvature and which result in a flat beam vs. stress gradient. Note that an equivalent free cantilever is very sensitive to stress gradients.

Thermal simulations are also done using Coventorware [44] and are shown in Fig. 3.6. In this case, a +100 MPa biaxial stress and a -4 MPa/μm stress gradient are taken in the switch. Again, l_j = 20-40 μm show the best stability vs. temperature. A design with l_j = 40 μm is chosen for RF measurements since it has a higher spring constant than l_j = 20 μm and thus a higher restoring force.

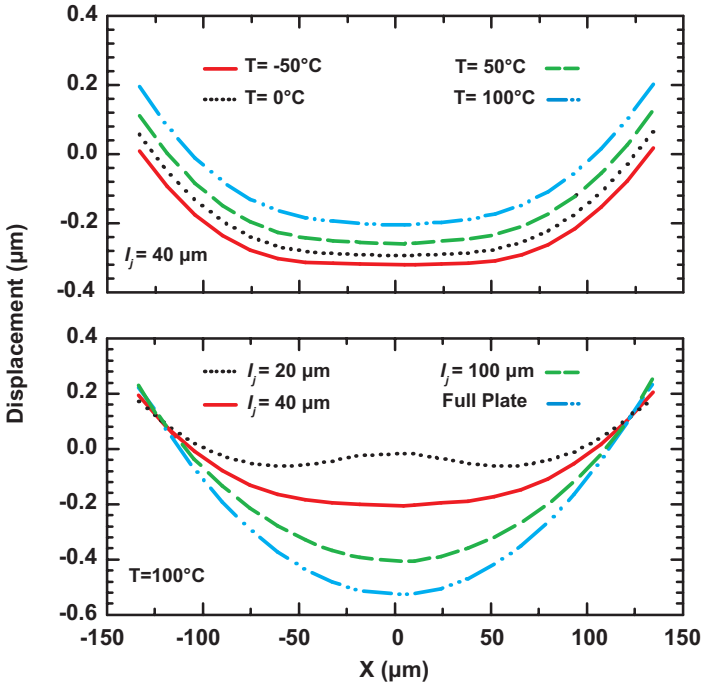

Figure 3.6: Thermal simulations for an in-plane stress of 100 MPa and a stress gradient of -4 MPa/μm.

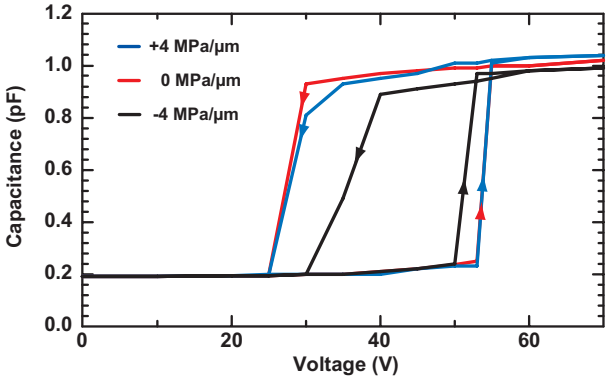

Figure 3.7: C-V simulation for 0 and +/- 4 MPa/μm stress gradients and an in-plane stress of 100 MPa for l_j = 40 μm.

Table 3.1: Simulated design parameters for the switch with l_j = 40 μm.

Parameter	-4 MPa/μm	0 MPa/μm	+4 MPa/μm
k_1,k_2,k_t	86,46*,132	86,46*,132	86,46*,132
V_p (V)	52.5	53.75	55
V_r (V)	33.75	28.75	28.75
C_{up} (fF)	0.19	0.19	0.19
C_{down} (fF)	0.99	1.02	1.04
C_r	5.21	5.36	5.47
f_0 (kHz)	31.8	31.8	31.8
Q_m	0.96	0.96	0.96

*: Residual Stress=100 MPa.

Note that the displacement will be positive if stress gradient of +4 MPa/μm is assumed, but the switch will always remain flat for l_j = 40 μm.

3.2.2 C-V Simulations

The C-V simulations are also done using Coventorware for l_j = 40 μm, a biaxial stress of 100 MPa, and stress gradients of 0 and +/- 4 MPa/μm (Fig. 3.7). The pull-down voltage is 52-55 V, and the up and down-state capacitance values are almost constant at ~0.2 pF and ~1 pF, respectively, and do not depend on the stress gradient. This again shows the flatness of the switch. Table 1 summarizes the simulated values for the switch with l_j = 40 μm.

3.2.3 Thermal Simulation vs. RF power

The switch current distribution and deflection are simulated vs. RF power using the method described in [31, 32, 42, 52]. The RF power dissipated in the MEMS switch is determined using S-parameters (Sonnet) [43] and is 0.36% at 10 GHz in the up-state position. Sonnet also solves for the exact current distribution on the switch, both in the up-state and down-state positions. This current is then transferred into equivalent heat strips at the current concentration areas in the switch, and the switch is simulated using Coventorware to determine its temperature rise and deflection. The switch temperature profile under a continuous RF power of 10 W in the up-state position (36 mW dissipated in the switch) is shown in Fig. 5.4. The switch is 75°C over the ambient temperature, and results in a deflection of -0.21 μm at the center of the switch, again under the conditions of an in-plane stress of 100 MPa and a stress gradient of -4 MPa/μm. Note that the deflection is similar to Fig. 3.6, except that in Fig. 3.6, an adiabatic temperature is taken, while in this case, a temperature gradient occurs on the switch, with the center being at 100°C and the anchors at 25-30°C. The capacitive switch can therefore handle 10 W without beam distortion and with planarity.

3.3 Fabrication

The switch is fabricated on a 500 μm quartz substrate using the UCSD fabrication process (Fig. 4.10). First, a 0.5 μm of sputtered gold layer is deposited to form the bottom electrode (a). Next, 0.2 μm of Si_3N_4 is sputtered as a dielectric layer (b). A 2.7 μm PMMA layer followed by a 0.3 μm of PMGI are used for the sacrificial layer (c). The dimples are formed on the PMGI layer using wet etching techniques (d), and a gold-plating seed layer is then sputtered. Finally the beam is electroplated to a thickness of 4 μm (e) and the switch is released using a critical point dryer system (f). Fig. 3.10 presents the micrograph of the fabricated switch. Fig. 4.11 presents the 3-D profile using a Zygo interferometer. The gold beam curvature is fitted to a stress gradient of -3 to -4 MPa/μm. The measured beam thickness is 4.5 μm instead of 4 μm and results in an increased spring constant and pull-down voltage.

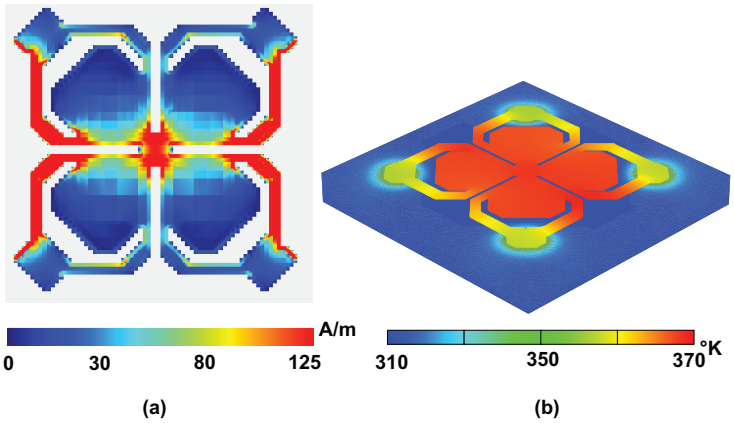

Figure 3.8: (a) Simulated current distribution, and (b) up-state thermal simulations at an incident RF power of 10W at 10 GHz.

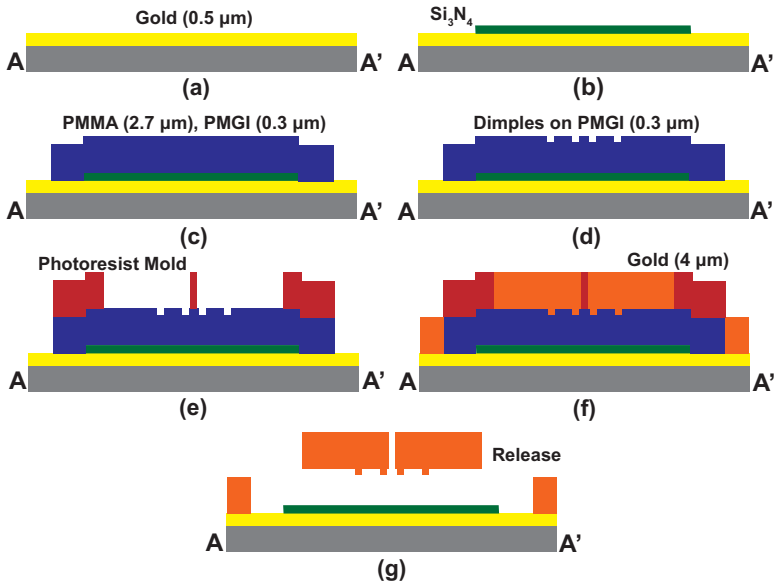

Figure 3.9: RF MEMS switched capacitor fabrication process.

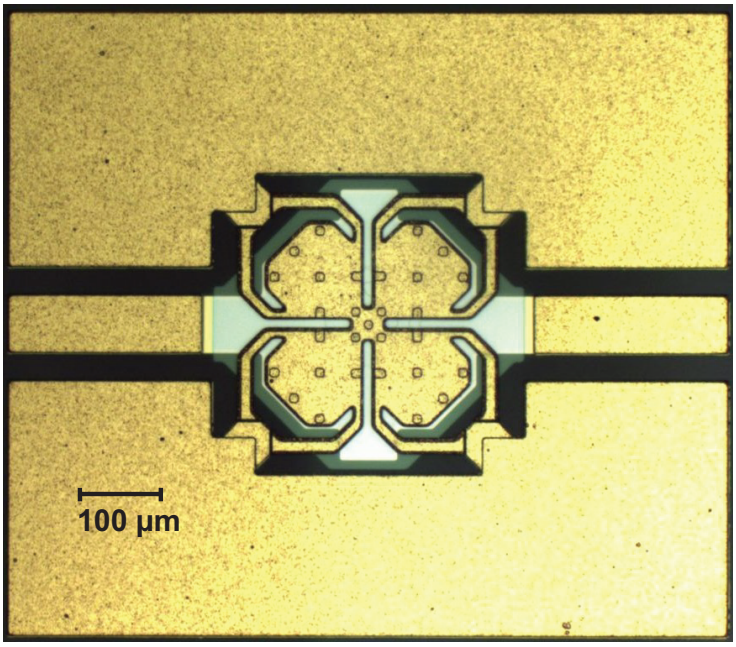

Figure 3.10: Micrograph of the RF MEMS switched capacitor.

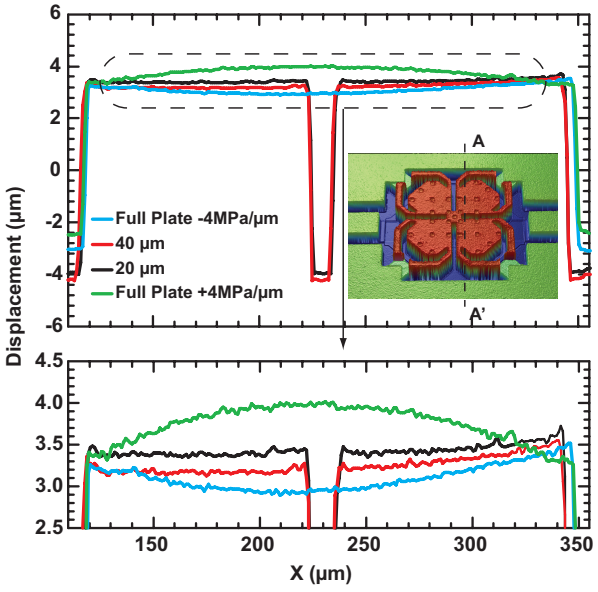

Figure 3.11: Measured switch 3-D Veeco profile for different joint dimensions.

3.4 Measurements

3.4.1 S-Parameters and Q

All measurements are done on unpackaged devices at room temperature and in a standard laboratory environment with a constant flow of dry nitrogen. The switch capacitance is determined after an SOLT calibration to the probe tips and by fitting the measured S-parameters to a transmission-line switch model based on CLR (Capacitance, Inductance, Resistance) components (Fig. 3.12). The extracted capacitances are Cu = 0.19 pF and Cd = 1 pF at 70 V (Cr = 5) and are in agreement with simulations.

The RF MEMS switch was also characterized using single port S-parameter measurements to determine its capacitance (Fig. 3.13) and Q (Fig. 3.14). The fitted Q is $>$ 50 at 8 GHz in the down-state position without the transmission-line loss and shows high ripple at f $<$ 8 GHz. This translates to an Rs $<$ 0.4 at 8 GHz for a 1 pF capacitor.

S-parameter techniques result in a large error for Q $>$ 80 [1], and a high-Q device should be measured using a loaded resonator technique for accurate values. Still, this measurements shows that the RF MEMS capacitor has a high Q up to 8 GHz even in the down-state position. The up-state position Q is so high that it cannot be measured using one-port S-parameters.

3.4.2 Vp, Vr and C-V

Fig. 3.15 presents the measured pull-in and release voltage vs. temperature. The chuck temperature was increased every 25°C up to 125°C and then decreased to room temperature. The measured voltages agree well with simulations and vary by +/- 2 V over a 100°C temperature range, showing the stability of the switch vs. temperature. Note that due to the dimples and the air dielectric in the down-state position, very little charging is observed even at 125°C.

Fig. 3.16 presents the measured C-V curve at 25°C. As predicted, the up and down-state capacitance values at $>$ 60 V are not dependent on the pull-down voltage. The measurement also shows a symmetrical C-V curve for both positive and negative voltages [45,46]. Again, this shows little charging in the switch due to the air gap in the down-state position.

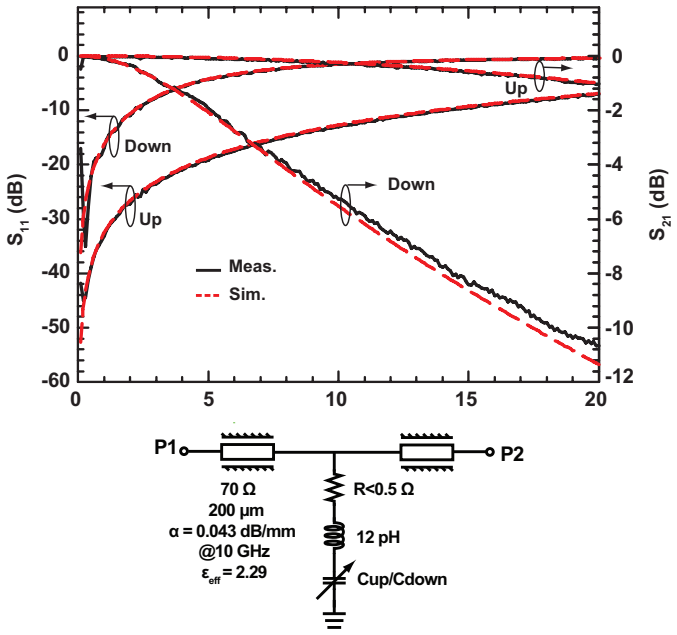

Figure 3.12: Measured and fitted S-parameters in a 2-port system, together with the CLR model.

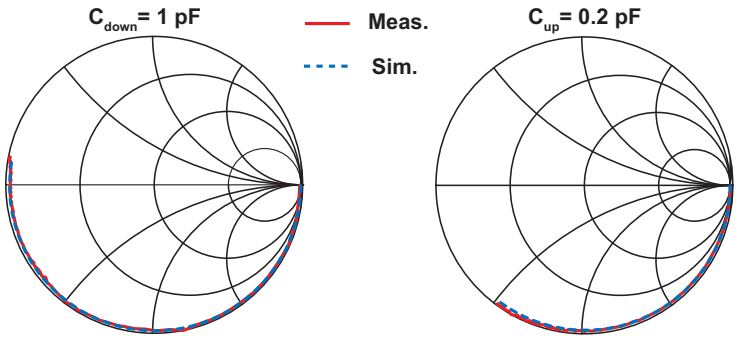

Figure 3.13: Measured and fitted S-parameters in a 1-port system.

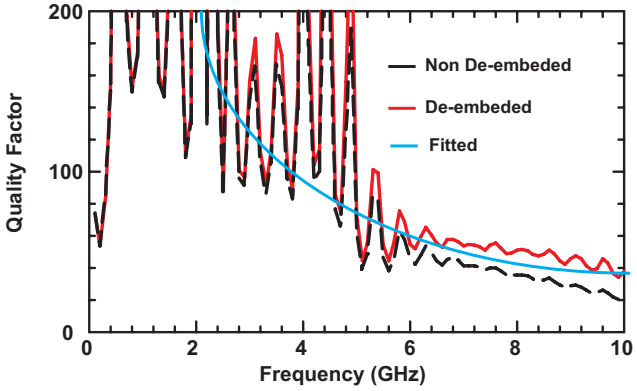

Figure 3.14: Q measurements using 1-port S-parameters.

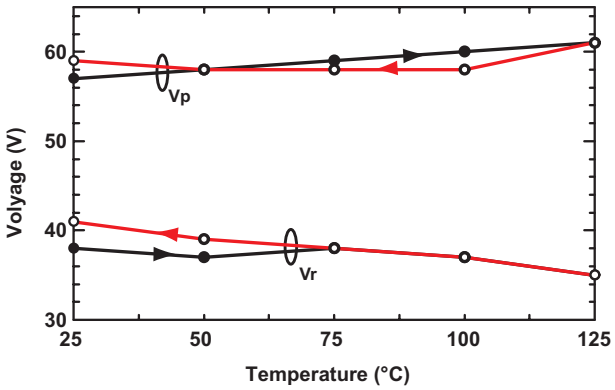

Figure 3.15: Measured pull-in and release voltages vs. temperature.

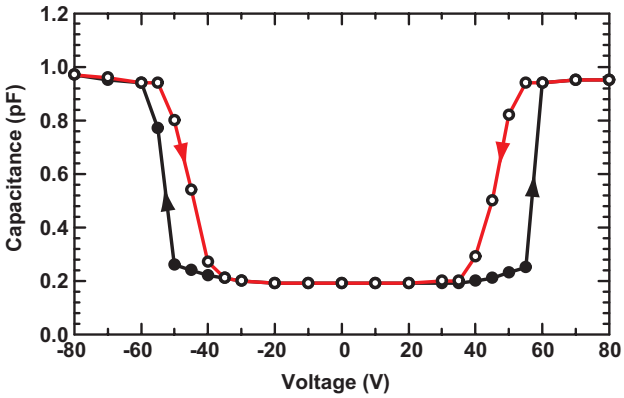

Figure 3.16: Measured C-V curve at 25°C.

3.4.3 Switching Time vs. RF Power

The switching time at V_{act} = 65 V is shown in Fig. 4.15 for both 100 mW and 2 W of input power. The pull-in time (t_{on}) is defined as the time it takes for the diode detector signal to reach 90% of its final value. The t_{on} time decreases with increasing RF power and this is due to a higher RMS RF voltage on the beam. Also, t_{off} increases at 2 W due to the voltage latching of the membrane to the bottom electrode in the down-state position.

3.4.4 RF Power Measurements

The power measurement setup is presented in Fig. 4.18 and employs a traveling-wave tube amplifier at 10 GHz. The cable and bias-T losses were normalized out of the measurements. At the output port, a back-to-back coax-to-waveguide transition was used to decouple the DC and step voltage leakages, which is then followed by an attenuator and a diode detector. The pull-in and release voltage vs. incident power at 10 GHz are shown in Fig. 4.18. The pull-down and release voltage decrease by 10 V and 20 V, respectively, up to ∼12 W of incident power due to temperature increase in the switch and to the additional force from the RF power. Note that the switched capacitor actuated well under hot-switching conditions since Vr remains > 15 V even at 12 W of RF power. No extensive reliability tests were done on this switch, but Fig. 4.18 was done over hours of time and thousands of switching cycles from 1 W to 12 W.

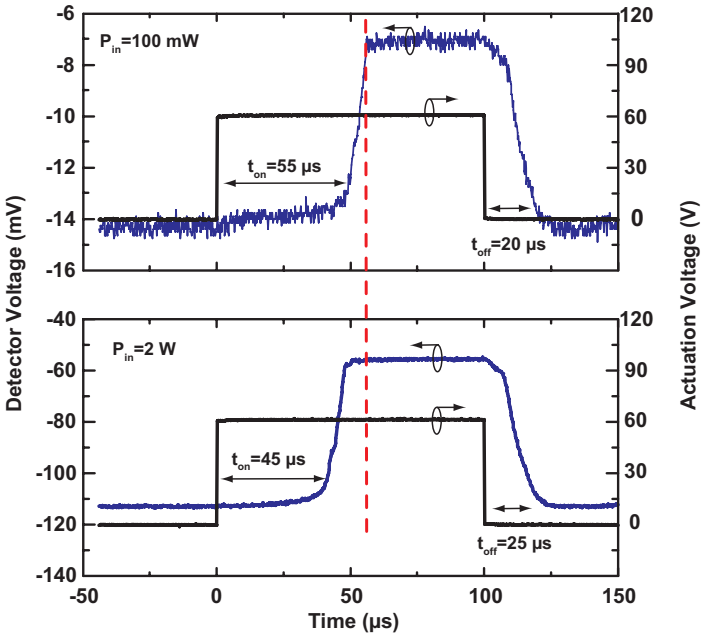

Figure 3.17: Measured switching time vs. voltage for 100 mW and 2 W of incident RF power.

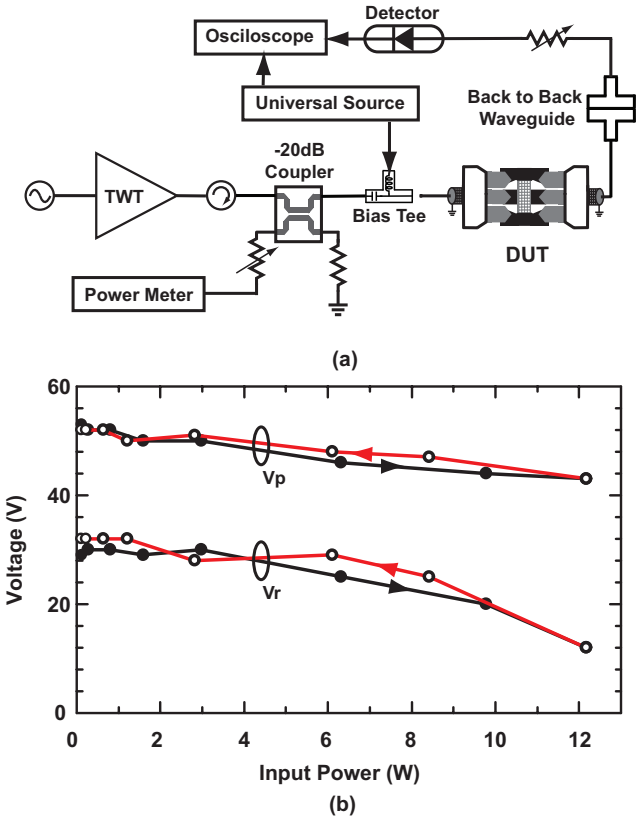

Figure 3.18: (a) High-power measurement setup and (b) measured Vp and Vr vs. incident power level at 10 GHz.

3.5 Acknowledgments

Chapter 3 is currently being prepared for submission to the IEEE Journal of Micro-Electro-Mechanical-Systems, JMEMS 2014; Hosein Zareie and Gabriel M. Rebeiz. The dissertation author is the primary author of this material.

Chapter 4

Compact, High-Power SPST and SP4T RF MEMS Metal-Contact Switches

4.1 Introduction

This chapter presents multiple-contact RF MEMS switches with medium contact and release forces that are capable of handling 20 W and > 2 W of RF power under cold switching conditions for SPST and SP4T configurations, respectively. The SPST design exploits spreading the RF current into 8 different contacts in parallel which lowers the current density on each contact. The switch topology is consists of 4 radial cantilevers that are anchored at the center and are attached together using a radial arc (Fig. 5.1). This introduces a sliding anchor along the symmetry planes which enhance the spring contact of the device by fixing the beam in the x-y directions and letting it only move in the z-direction. The contacts are Au-Ru so as to increase the power handling while still maintaining a switch resistance of ∼1-2 Ω.

4.2 SPST Design

Fig. 5.1 presents the top view and cross-section of the proposed RF MEMS metal-contact switch. The switch is fabricated using a 5 μm electroplated gold beam and a gap of 0.9 μm.

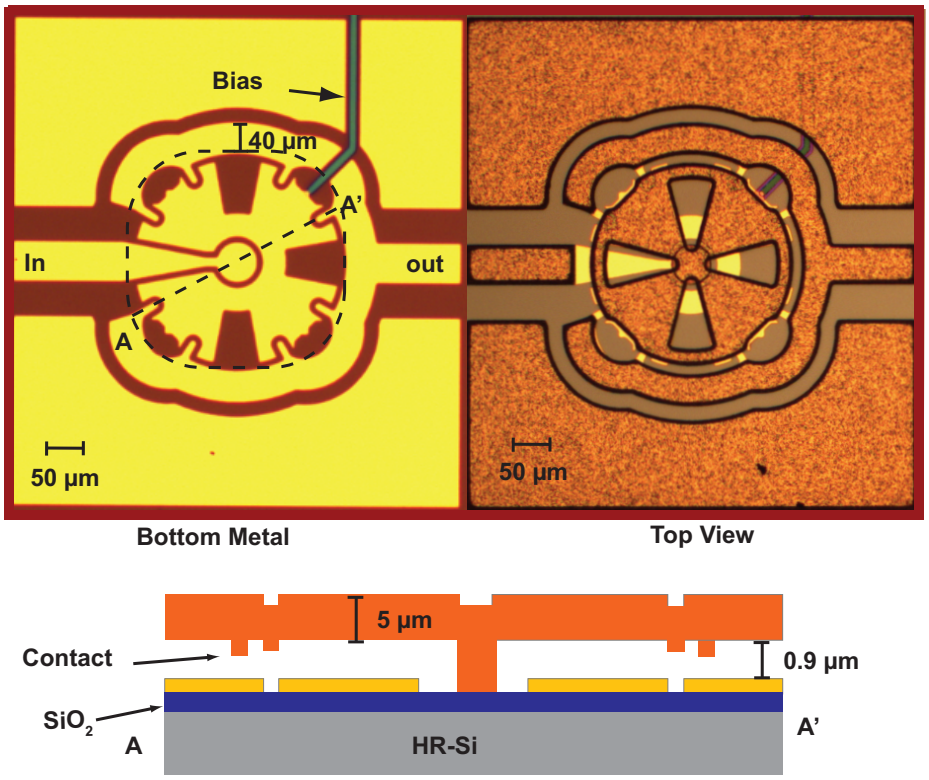

Figure 4.1: Top view and cross-section of the SPST metal contact switch. The switch area is $\sim$240$\times$240 μm^2.

The outputs of the radial cantilever sections are attached together resulting in an 8-contact design. The four radial cantilevers are connected together using a sliding anchor (Fig. 4.2). In this configuration, the cantilever beams are connected along symmetry planes, and the only allowable displacement is in the z-direction. The sliding anchor guarantees that no displacement can occur in the bi-axial directions due to symmetry which greatly improves the switch stability, and also the contact and release forces by increasing the spring constant. However, since the sliding anchor can freely move in the z-direction, this design does not offer improved stability to stress gradient effects.

4.2.1 Mechanical Simulations

The switch is designed in four different configurations (Fig. 4.3). The switch diameter is kept constant (D = 240 μm) and the connecting arcs are designed in order to provide different effective spring constants and actuation voltages.

The spring constant and tip displacement are simulated using Coventorware [44] versus the in-plane stress and are shown in Fig. 4.4 (simulations are done for a gold beam with E = 35 GPA and $\upsilon = 0.4$ [41].) The spring constant is based on a uniform force applied over the actuation electrode and with the displacement defined at the contact dimples. A spring constant of 550-750 N/M can be obtained with low sensitivity to in-plane stress for all designs. By contrast, the spring constant of the standard design (an equivalent cantilever) composed of 4 radial arcs and not connected together is 150 N/M (4×37.5 N/m), resulting in much lower contact and release forces. The spring constant of the standard design (no sliding anchors) can be increased to 750 N/M using a 8.5 μm thick beam, but this may not be compatible with top-metal (4-5 μm thick) CMOS fabrication techniques. The spring constant is almost independent of the in-plane stress since the beam is anchored at the center and resulting in a cantilever-type design while still providing high stiffness. Also, designs M1-M4 have the same tip displacement versus the in-plane stress. However since the beams are only fixed at the center and the sliding anchor allows free movement in the Z-direction, the displacement vs. stress gradient follows the cantilever-based equations as shown in Fig. 4.5 [1]. In most processes for gold and nickel plating, the stress gradient is positive [53], and therefore, this does not pose a problem.

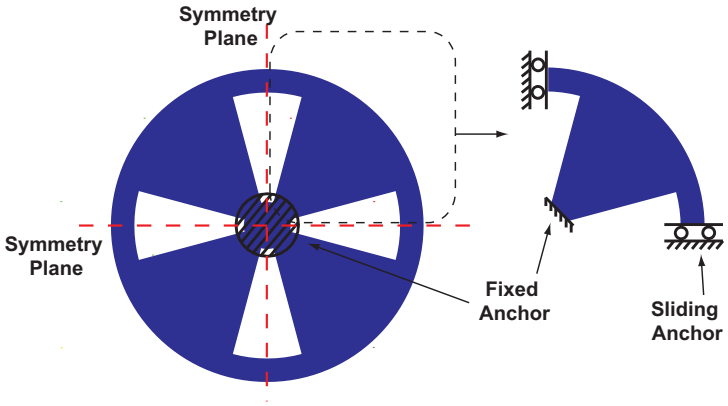

Figure 4.2: Switch connecting arcs and symmetry planes resulting in a sliding anchor.

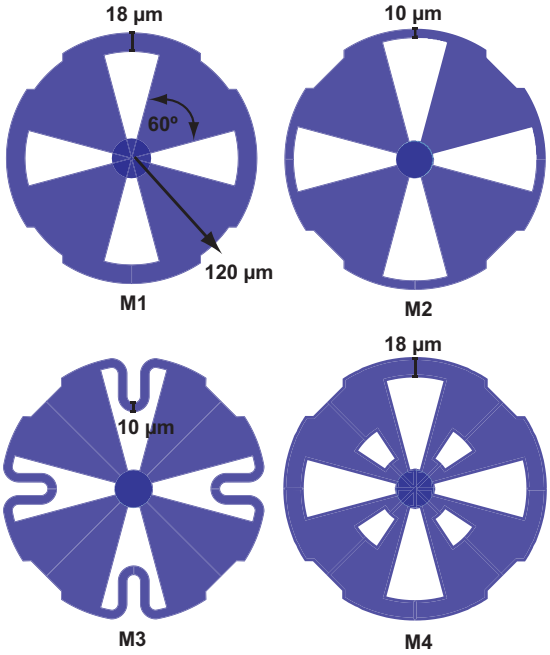

Figure 4.3: Different switch configurations for spring-constant simulations. (Radius is 120 μm).

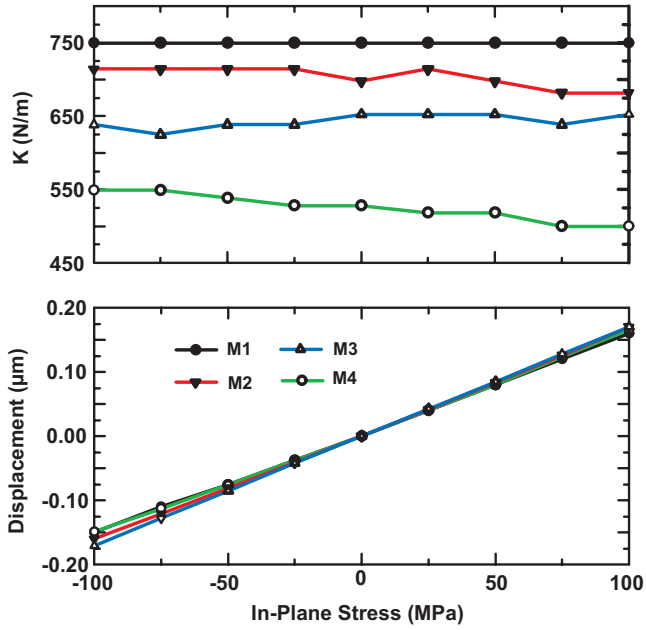

Figure 4.4: Simulated spring constant and tip displacement vs. biaxial stress for different designs.

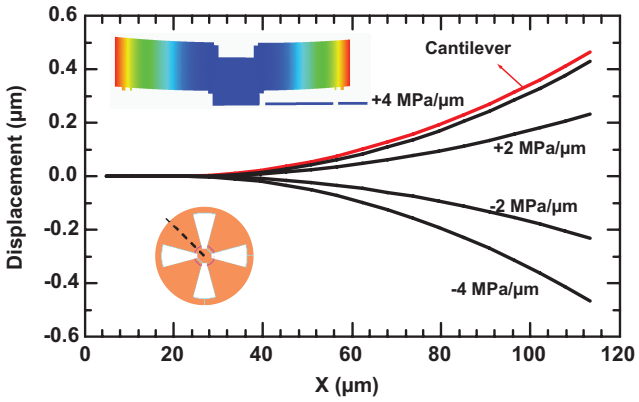

Figure 4.5: Simulated tip displacement for the M1 design and different stress gradients.

4.2.2 Contact and Release Force

The switch contact and release forces are simulated using Coventorware. The contact force is set by the dimple height since it determines the down-state gap and thus the down-state force. The dimple height also determines the switch deflection from the un-actuated position and together with the natural spring constant, will determine the release force [1]. The natural spring constant is based on a point-force applied at the dimple area divided by the displacement on the dimple. In this design, the dimple height is chosen to be 0.35 μm as a compromise between the contact and release forces. Fig. 4.6 presents the simulated contact and release force for the M1 design versus the voltage for and in-plane stress of 0 and 100 MPa and assuming a zero stress gradient. The release force is 0.2-0.3 mN per quadrant (two contacts) and the contact force is 0.3-0.7 mN at 70-90 V per quadrant. Fig. 6b presents the contact and release force vs. stress gradient for the M1 configuration. For a biaxial stress of 100 MPa and a stress gradient of +4 MPa/μm, which is typical of the UCSD fabrication process, one can operate at 80 V with almost the same contact and release force (0.4-0.5 mN per quadrant, and 1.6-2 mN for the SPST switch). Table 1 summarizes the design parameters of the various switch configurations. Sonnet EM Suite [43] is used for the up-state capacitance simulations, and all designs result in Cu $\sim$70 fF on a high-resistivity silicon substrate given mostly by the fringing fields between the beam and the output transmission-line.

Table 4.1: Simulated switch parameters for different anchor configurations.

Parameter	M1	M2	M3	M4
k	750	700	650	500
V_p (V)	55	53.5	50.5	49.7
V_r (V)	40.5	40.5	37.5	37.5
C_{up} (fF)	70	70	70	70
Contact force (mN)	0.68	0.68	0.71	0.74
Release force (mN)	0.43	0.4	0.36	0.29
f_0 (kHz)	135	122	112	120
Q_m	3.4	3.2	2.9	2.9

*: Residual Stress=100 MPa, +4 MPa/μm.

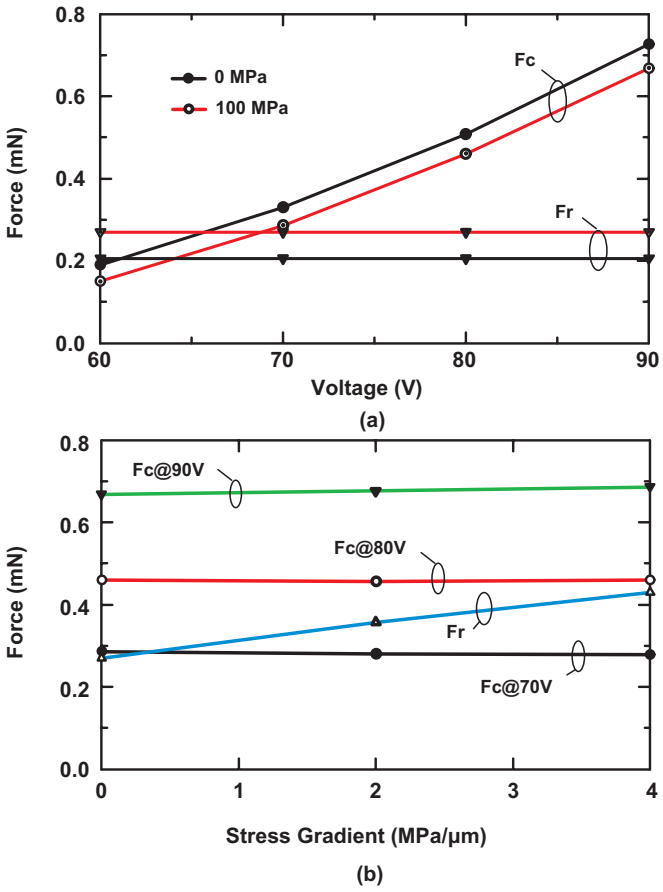

Figure 4.6: Simulated switch contact and release force per quadrant (two contacts) for the M1 configuration and (a) with zero-stress gradient, and (b) in-plane stress of 100 MPa vs. different stress gradients.

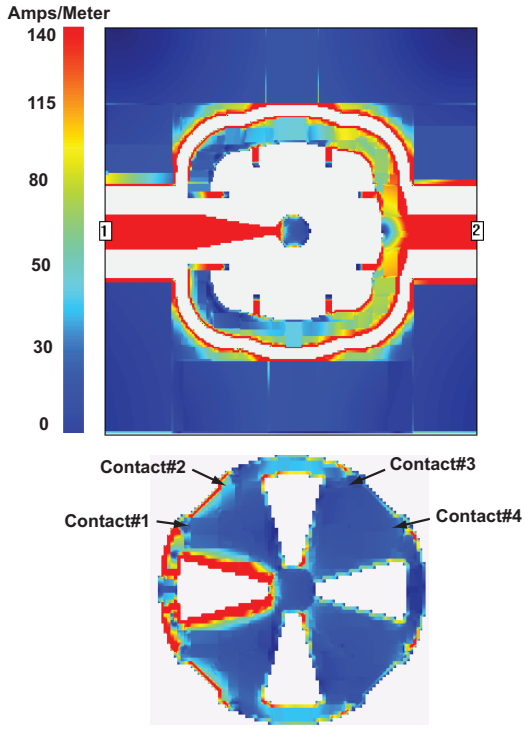

Figure 4.7: Simulated RF current distribution simulation of the switch using Sonnet at 2 GHz.

Table 4.2: Simulated contact current density

Current Density	Contact#1	Contact#2	Contact#3	Contact#4
4Ω @1GHz	132	136	138	132
8Ω @1GHz	132	136	137	130
4Ω @2GHz	136	134	137	137
8Ω @2GHz	132	135	137	130

4.3 RF Current Simulations

The SPST switch consists of four quadrants each having two-contacts resulting in an 8-contact design which increases the switch power handling and reliability. The RF current distribution at 2 GHz is simulated using Sonnet for a contact resistance of 4-8Ω (per contact) which results in a total switch resistance of 0.5-1Ω (Fig. 5.4). The simulated current for each contact for 10 mW of input power is shown in Table II (+/- 3% accuracy). It is seen that the current divides equally between all the contacts, and this results in uniform heat distribution over the entire switch and high power handling capabilities. Also, the switch is resilient to open-circuit failures since if a quadrant fails (pair of contacts), then the current will redistribute and still divide in a uniform fashion due to the 4-8Ω resistance for each contact. This allows for a potentially more reliable switch than a standard two-contact design.

4.4 Compact SP4T Switch

The mechanical design also allows that each of the four quadrants be actuated independently while the other quadrants remain in the up-state position (Fig. 4.8). The sliding anchor moves -0.25 μm when one quadrant is actuated in the down-state position since symmetry is broken (one quadrant is down while the other quadrants are up), but this does not cause the un-actuated quadrants to make a contact. The displacement of each contact under the actuation of one quadrant is shown in Table III. In this table, the 0 μm position is for the cantilever with no biaxial or in-plane stress, and the -0.55 μm position shows contact being made due to a dimple height of 0.35 μm. This property allows the construction of a very compact SP4T switch by using 4 independent actuation electrodes and output ports, each for one quadrant. The simulated contact and release forces are exactly as presented for one quadrant in Section II. The simulated up-state

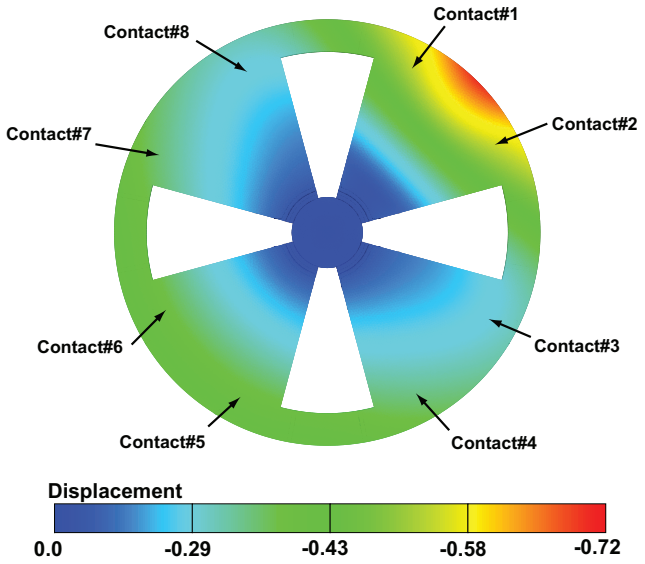

Figure 4.8: SP4T displacement when one quadrant is actuated: 100MPa in-plane stress and stress gradient of +4MPa/μm are used for simulations.

capacitance is Cu = 17 fF which is approximately 4 times lower than the SPST design. The SP4T will handle less power than the SPST design due to the use of only two contacts, but as will be seen in Section VI, it can still handle > 2 W of RF power with high reliability. The SP4T switch micrograph is shown in Fig. 4.9, and the entire switch occupies an area of $\sim$240$\times$240 μm^2.

4.5 Fabrication

The SPST and SP4T switches are fabricated on a 500 μm high-resistivity silicon substrate using the UCSD fabrication process (Fig. 4.10). First, 0.35 μm of sputtered gold is deposited to form the bottom electrode (a). Then, 0.1 μm of Ruthenium is sputtered for the bottom-contact formation. A 0.4 μm PMMA layer followed by 0.35 μm of PMGI is used for the sacrificial layer (c). The dimples are formed on the PMGI layer using wet-etching techniques (d), and then a gold-plating seed layer is sputtered. Finally the beam is electroplated to a thickness of 5 μm (e), and the switch is then released in a critical point dryer system (f). Pictures of the completed switches are shown in Figures 1 and 9 for the SPST and SP4T, respectively.

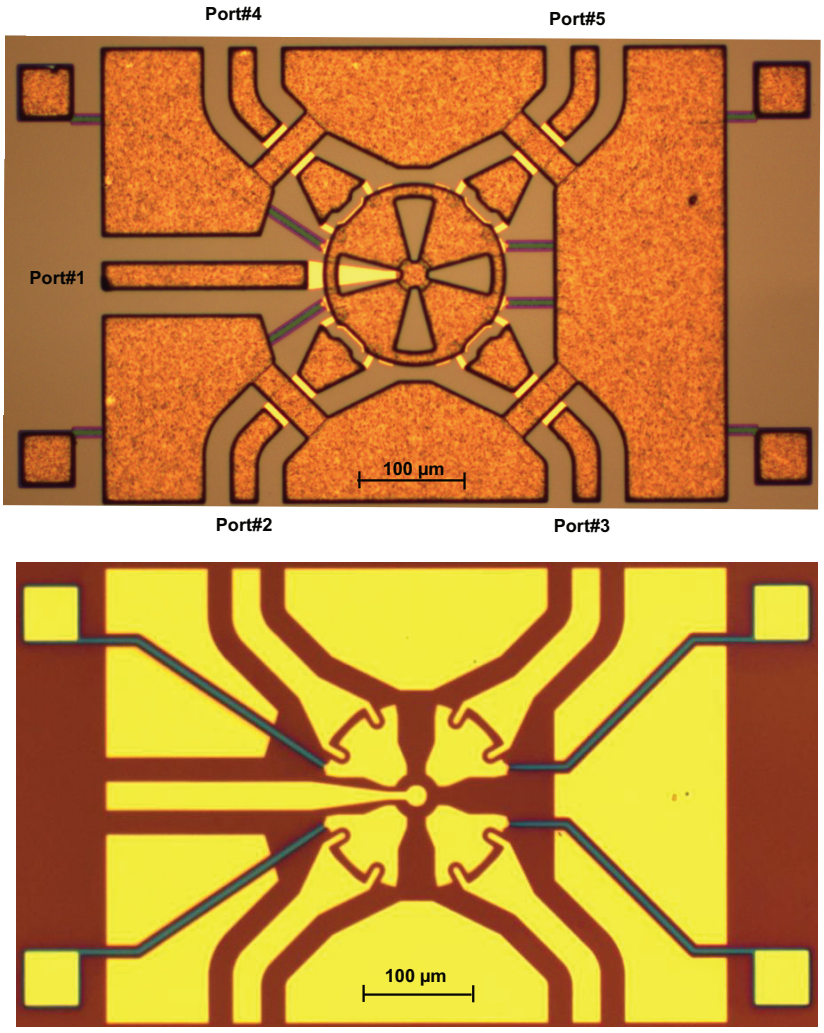

Figure 4.9: Micrograph of SP4T switch for the M1 design.

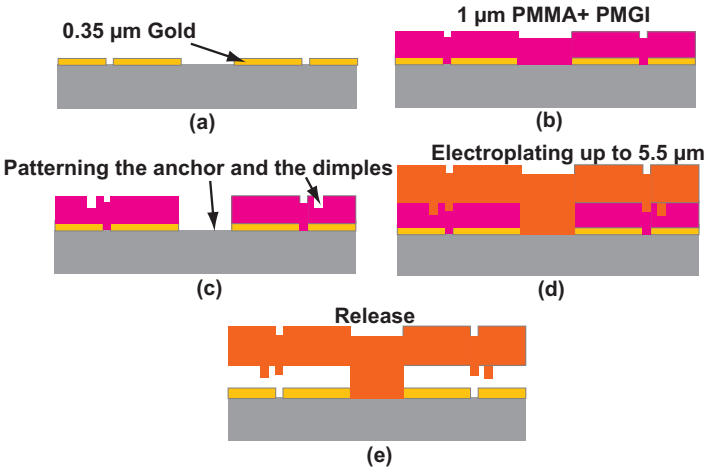

Figure 4.10: Fabrication process of the high-power SPST and SP4T RF MEMS metal contact switches.

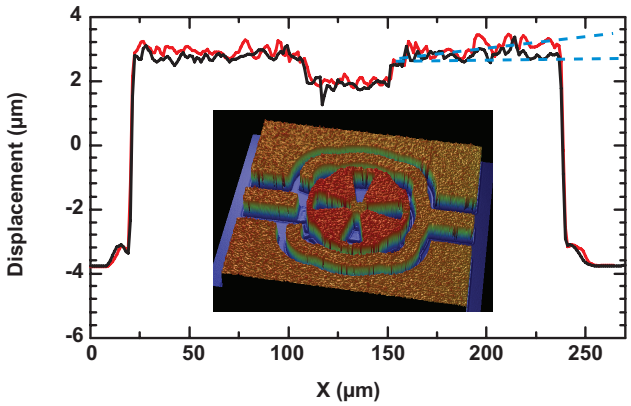

Figure 4.11: Measured 3-D profile of the SPST switch for both fixed anchor and sliding anchor for the M1 design.

Table 4.3: Simulated SP4T switch displacement for different quadrants.

Contact	Initial Position(μ)	Final Position(μ)
#1	0.62	-0.55(Contact)
#2	0.62	-0.55(Contact)
#3	0.62	0.28
#4	0.62	0.49
#5	0.62	0.58
#6	0.62	0.58
#7	0.62	0.49
#8	0.62	0.28

The 3-D profile of the fabricated switch is measured using veeco (Fig. 4.11). The displacement is fitted to a stress gradient of +4 MPa/μm which causes a deflection 0.4 μm in the upward direction. Note that if the sliding anchor is anchored, then the beam has virtually no deflection, but this design is sensitive to biaxial stress and temperature and is not considered in this work.

4.6 Measurements

4.6.1 S-Parameters

All measurements are done on unpackaged devices at room temperature and in a standard laboratory environment with flowing dry nitrogen. The switches are biased at 90 V for the on-state measurements and results in a resistance of 1-2Ω for the SPST switch, and 2-4Ω for the SP4T switch in the open environment. The resistance is dominated by contaminants and is not determined by the Au-Ru interface. The S-parameters are measured after an SOLT calibration to the probe tips and are presented in Fig. 4.12 and Fig. 4.13 for the SPST and SP4T designs, respectively. The losses include the input and output CPW lines ($\sim$150 μm line) on the high resistivity silicon substrate. The CPW lines account for $\sim$0.05-0.1 dB of the measured losses. The SPST switch shows a measured insertion loss $<$ 0.5 dB up to 14 GHz with an isolation of 20 dB at 2 GHz due to the large up-state capacitance (Cu = 70 fF). The SPST switch therefore should be placed in a series-shunt configuration for high isolation above 2 GHz. The SP4T

switch shows a measured insertion loss of < 0.8 dB with an isolation of 20 dB at 12 GHz resulting from the up-state capacitance per port (Cu = 17 fF). The isolation is 30-36 dB at 2-3 GHz, and the switch can be used up to 3 GHz without a series-shunt circuit. Measurements agree well with simulations.

4.6.2 Vp, Vr vs. Temperature

Fig. 4.14 presents the measured pull-in and release voltage for two different devices versus temperature for the SPST and SP4T designs. The chuck temperature was increased every 25°C up to 105°C and then decreased to room temperature. The beam in-plane stress turns compressive vs. temperature due to the different coefficient of expansion between the gold cantilever and the silicon substrate, and this deflects the beam downward and decreases the pull-in and release voltages. Still, a variation of $<$ 5-6 V is observed up to 105°C.

4.6.3 Switching Time and Mechanical Q

The switching time versus voltage is shown in Fig. 4.15 for the SPST and SP4T designs. The pull-in time (t_{on}) is defined as the time it takes for the diode detector signal to reach 90% of its final value.

The measured release time t_{off} is independent of the actuation voltage and is $\sim$2 μs (not shown). The measured mechanical resonant frequency and Q for the SPST switch is $\sim$115 kHz with a Q$\sim$3.4 (Fig. 4.15). The same measurements are obtained for the SP4T switch since it is identical to the SPST switch in the up-state positions. Measurements agree well with simulations obtained using the methods in [1].

4.6.4 Contact Resistance

The contact resistance for several SPST and SP4T switches were measured using a four-point probe (Fig. 4.16). The SPST design has a lower contact resistance due to the much higher contact force and 8 different contacts in parallel. Still, these measurements are limited by contaminants on the switch and not by the Au-Ru contact theory.

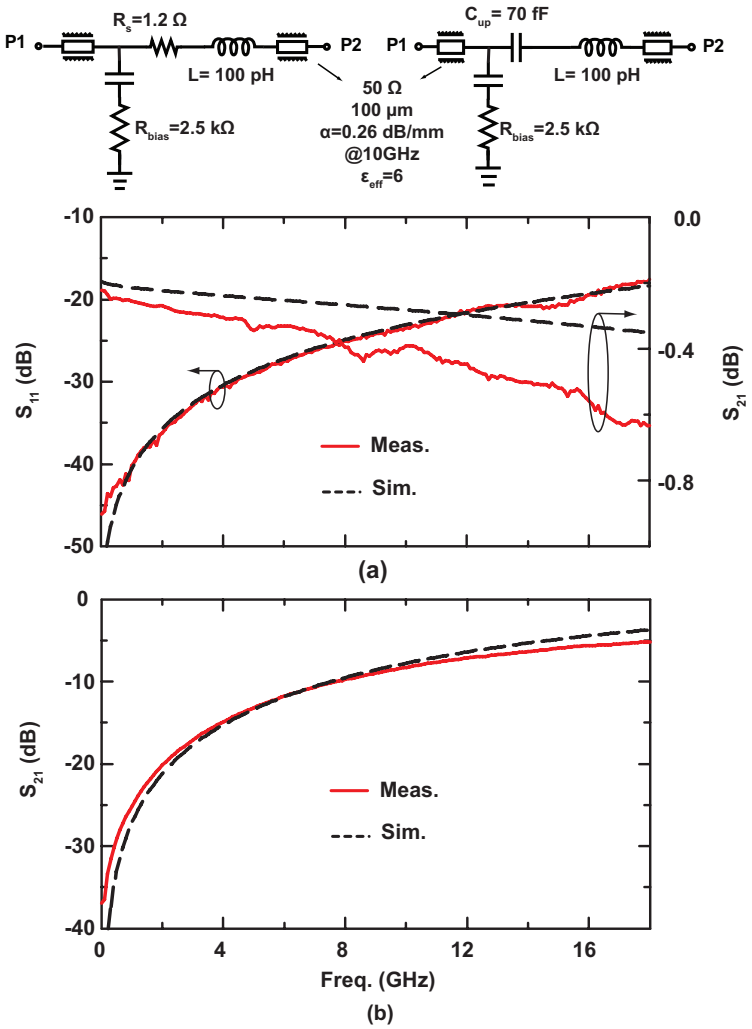

Figure 4.12: S-parameter measurements of the SPST switch: a) Down-state position (insertion loss state) and b) up-state position (isolation state).

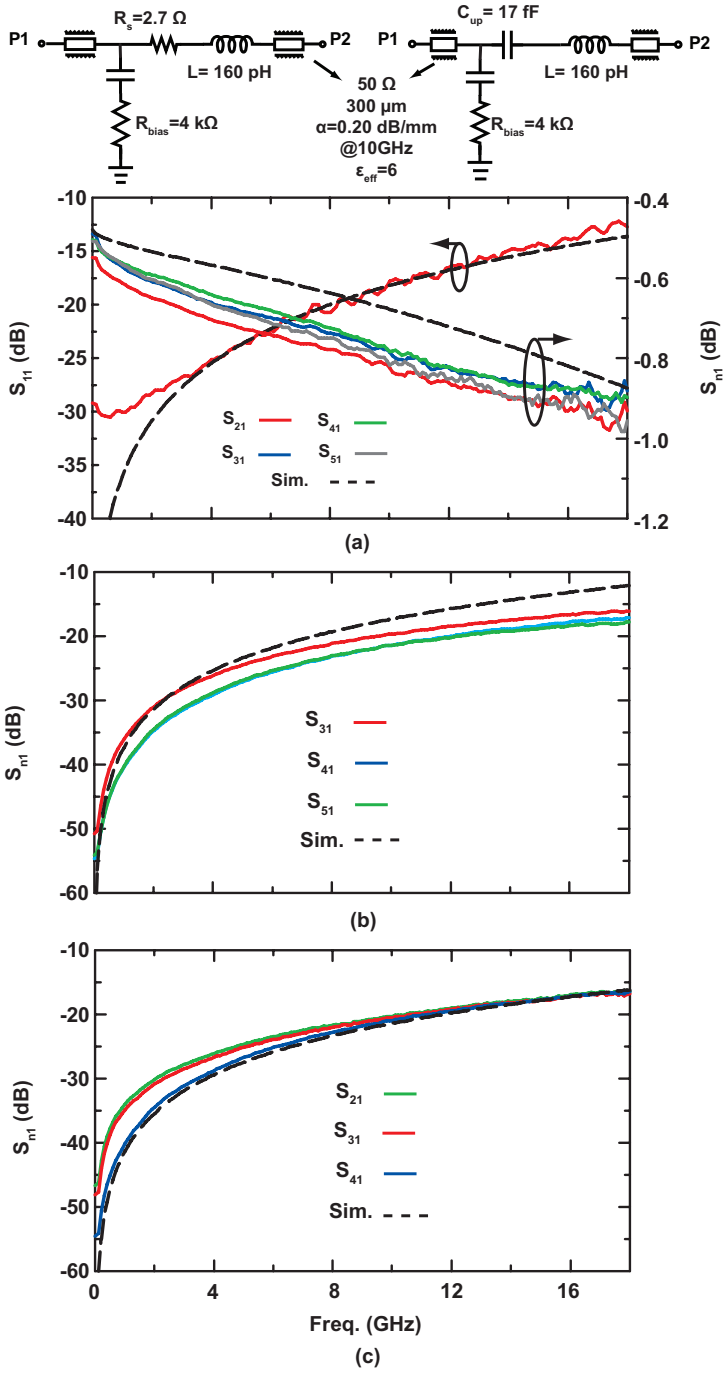

Figure 4.13: S-parameter measurements of the SP4T switch: a) Down-state position (insertion loss state) for each of the 4 quadrants, b) Up-state position (isolation state) when one quadrant is actuated and the other quadrants are non-actuated. See Fig. 4.9 for port definitions. Simulations are done using a ∼3 Ω switch resistance, c) same as b but using a different quadrant.

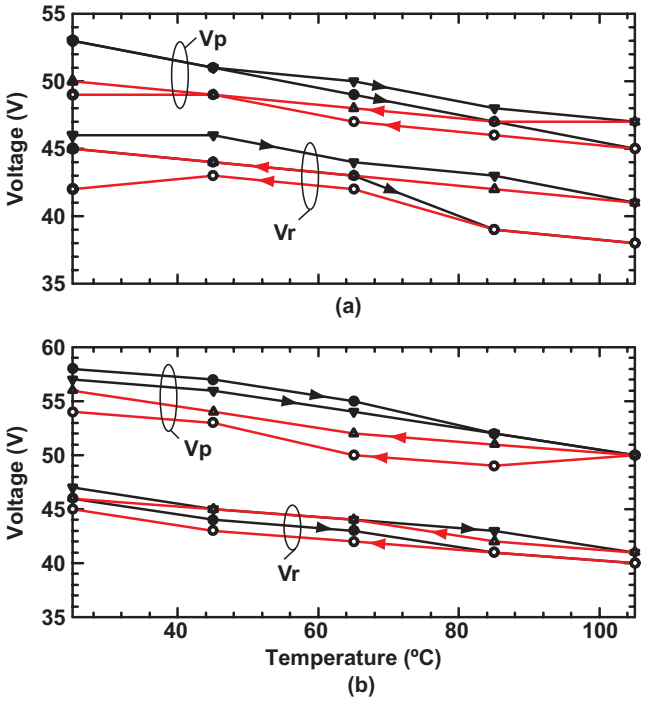

Figure 4.14: Measured (a) SPST and (b) SP4T pull-in and release voltage vs. temperature.

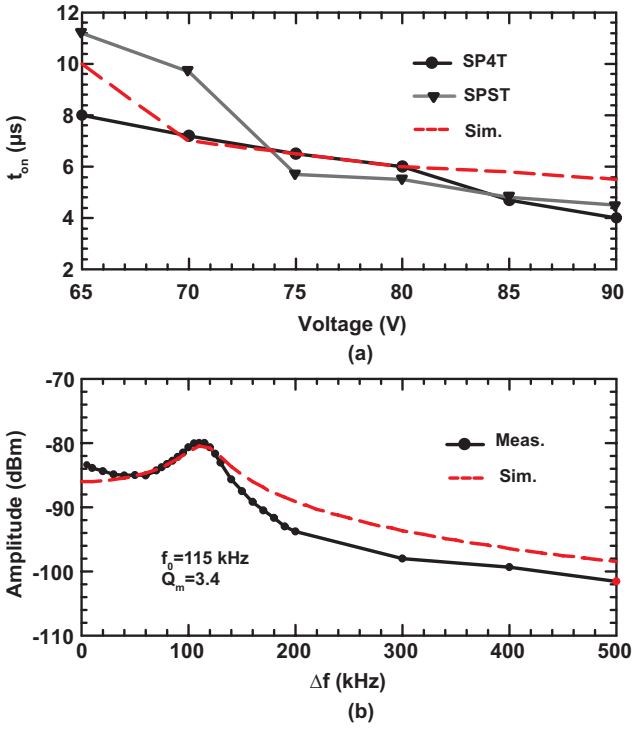

Figure 4.15: Measured (a) SPST and SP4T switching time vs. voltage, and (b) SPST mechanical resonant frequency and Q.

4.6.5 Linearity Measurements

The IP2 and IP3 values were measured for the SPST and SP4T switch using a two-tone test at f_1, f_2 of 1925 MHz and 1975 MHz respectively (IP3 values are independent of the separation frequency). Both switches result in an IP2 of 104 dBm and an IP3 of ∼70 dBm, and are limited by the GSG probe contact resistance with the gold transmission line, and by the CPW line on a high resistivity silicon substrate (Fig. 4.17). These values are very similar to those obtained in [1, 12] using a comparable test setup.

4.6.6 RF Power Handing Measurements

The measurement setup is presented in Fig. 4.18 and employs a power amplifier at 500 MHz. The cable and bias-T losses were normalized out of the measurements. All tests are done in cold-switch conditions at a 10 kHz switching rate. The SPST switch with its 8-contact points and a total contact force of 2.8 mN at 90 V (see Fig. 4.6) can handle 5-10 W up to 100 Million cycles (test stopped at 100M cycles and not due to switch failure), and ∼20 W up to 30 Million cycles (Fig. 4.18) (switch failed as an open circuit). At 10-20 W, the total RMS current in the SPST switch is 0.44-0.65 A_{rms}, and each contact is handling 55-85 mA_{rms}. Again, the measured contact resistance is determined mostly by contaminants since the switch is tested in non-hermetic conditions. The SP4T switch handles less RF power since each arm is actuated independently and the quadrant results in a 0.45-0.7 mN contact force at 80-90 V.

Still, the SP4T can handle an RF power of 2 W up to 100 Million cycles (test stopped at 100M cycles) and 5 W for ∼30 Million cycles (Fig. 4.18) (switch failed as an open circuit). Although one switch arm is shown in Fig. 4.18, the other arms resulted in the same results at 2 W power testing.

The SPST and SP4T switches were also tested at 100 mW to 1 W up to 100 Million cycles (test stopped with no switch failures) and these results are not shown for brevity.

4.6.7 Creep Measurements

Preliminary creep measurements were done on the SPST switch. In this case, the switch is actuated at 80 V and the Vp and Vr are measured every 1 second in a 30 ms time-frame using an up and down ramp voltage waveform [49, 52]. Measurements over 3 hours indicate very little change in Vp, but a large variation in Vr is observed which

can be the result of stiction due to the non-clean environment or due to surface charges trapped due to some residual humidity [54, 55] (Fig. 4.19). Further testing is required in a hermetic environment.

4.7 Acknowledgments

Chapter 4 is mostly a reprint of the material that has been accepted for publication in the IEEE Transactions on Microwave Theory and Techniques, 2014; Hosein Zareie and Gabriel M. Rebeiz. The dissertation author is the primary author of this material.

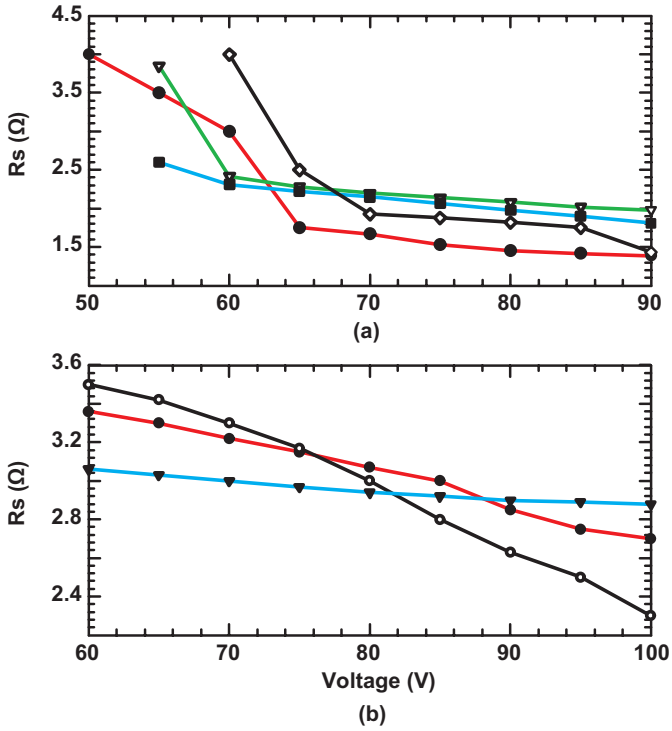

Figure 4.16: Measured (a) SPST and (b) SP4T contact resistance vs. actuation voltage using a four-point probe measurements method (several switches shown).

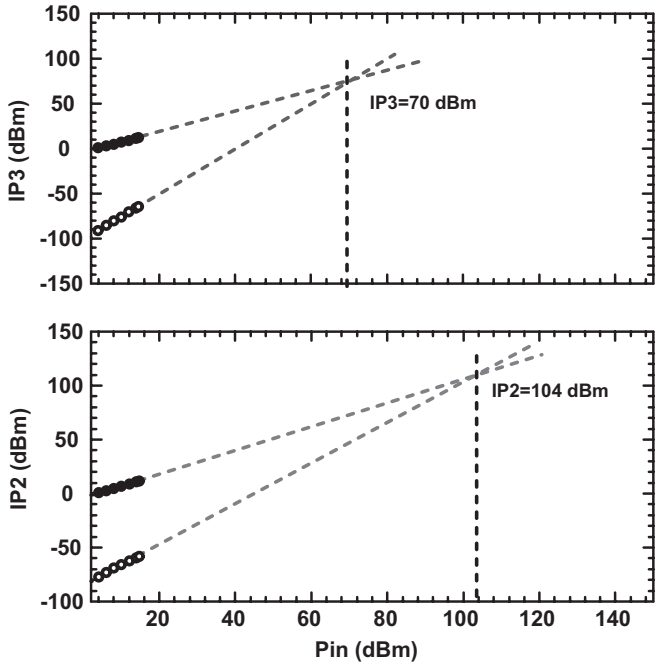

Figure 4.17: Measured SPST and SP4T linearity at 2 GHz.

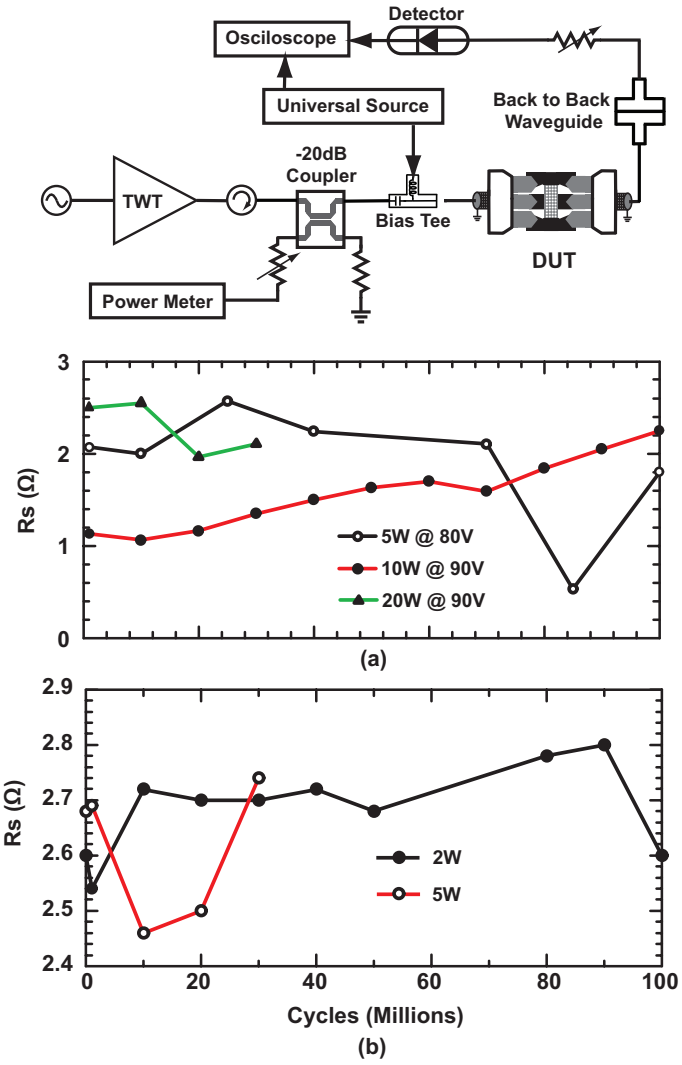

Figure 4.18: High-power measurement set-up, a) SPST and b) SP4T power handling experiments.

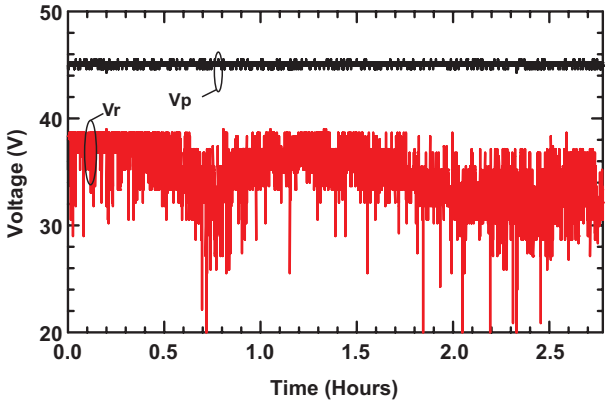

Figure 4.19: Measured Vp and Vr over 3 hours of constant actuation. Measurements are done every second in a 30 ms window.

Chapter 5

High Performance RF MEMS Capacitive Switches and Circuits using Thin Metal Process

5.1 Introduction

RF MEMS switches have been demonstrated in both capacitive and metal contact configurations. Capacitive MEMS switches have the potential to replaced the current semiconductor counterparts. These devices can be designed to obtain very high-Q values compared to other type of switches. These devices can be widely used in switch capacitor circuits for tuning applications with capacitance ratios of 3-10 or for switching applications with higher capacitance ratios. In this chapter, we introduce a thin film membrane capacitive switch which uses 0.5 μm and 0.75 μm membrane thicknesses in the Raytheon process. Although the thin membrane will degrade the switch thermal performance by increasing its thermal resistivity, we have tried to optimize the previous circular design introduced in [42] in order to obtain better thermal performance.

In this design the effort was to minimize the spring constant variation and the displacement over the actuation electrode with increasing temperature. Since the switch actuation voltage depends on the switch gap and the spring constant, this helps in maintaining the same actuation voltages as the membrane is heated. The switch top view is shown in Fig. 5.1. The membrane diameter is increased to 117 μm and the membrane thickness is increased to 0.75 μm compared to the original design [42] in

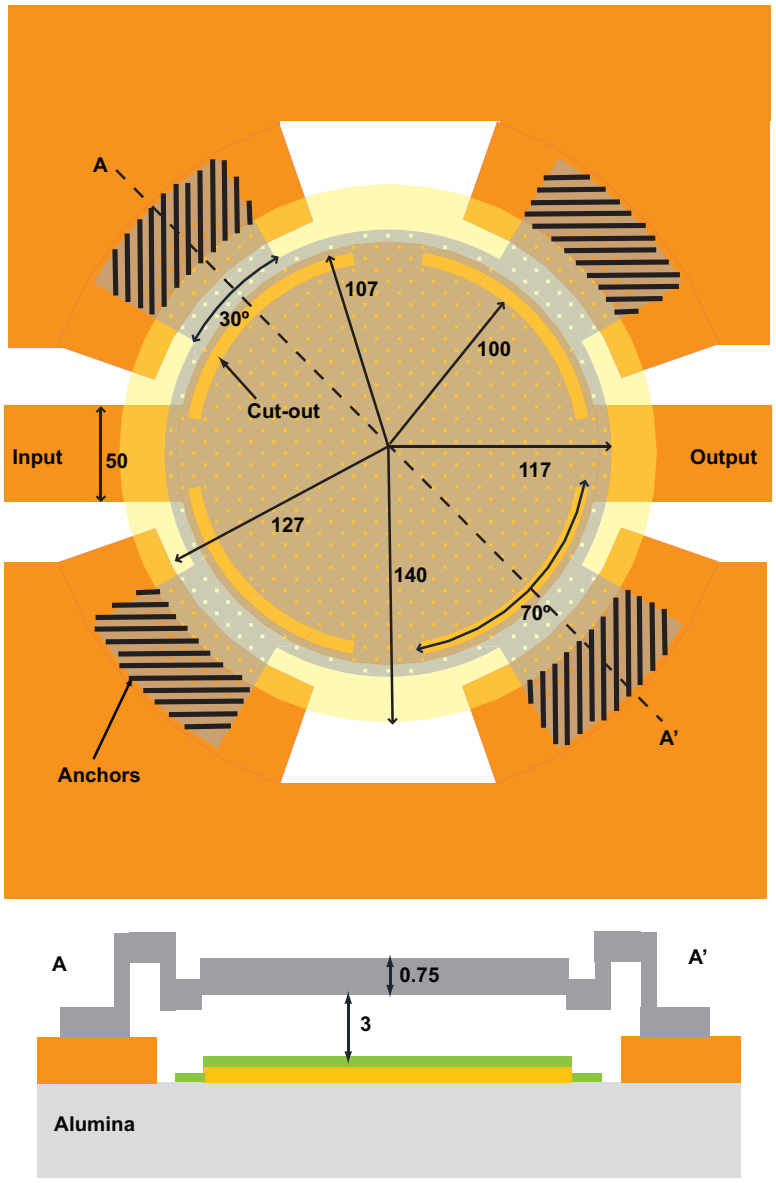

Figure 5.1: Top view of the high-power RF MEMS capacitive switch. All dimensions are in μm.

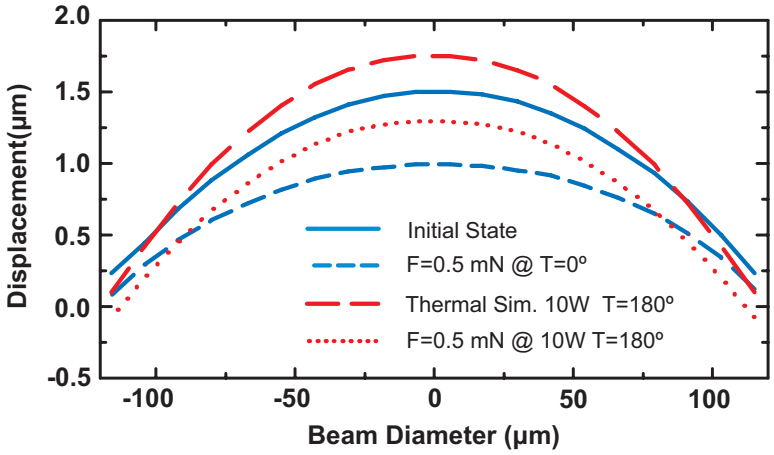

Figure 5.2: Simulated membrane displacement for 0.5mN of uniform force for both 27°C and 180°C.

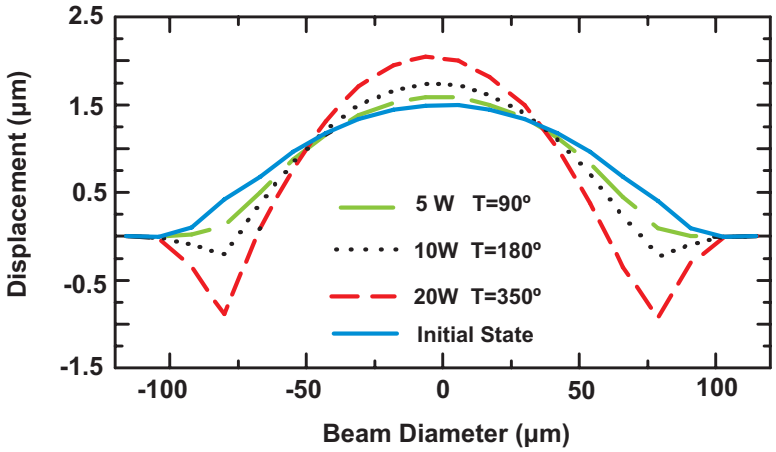

Figure 5.3: Beam displacement vs. different temperature values.

order to maintain nearly the same actuation voltage. The gap is 3 μm and the anchor area and the CPW lines have been electroplated to 2.7 μm to lower the loss.

5.2 Switch Design

5.2.1 Mechanical Analysis

The switch consists of a circular membrane that is anchored along its circumference at anchors placed 90° apart (Fig. 5.1). The anchors have been separated from the center part using 70° cut-outs. The cut-outs minimize the effect of the stress on the spring constants. The beam spring constant is composed of the geometry-dependent k_1 and stress-dependent part k_2. It can be shown that a longer difference between the cut-out and the anchor angle results in a lower k_2 value and will results in designs with less dependency on the residual stress and therefore temperature.

The distance between the cut-out and the anchor is an important parameter as the switch can be under a lot of temperature variations. If the distance is short, the displacement will move towards the center of the beam which contains the lower spring constant portion of the beam. By increasing the cutout-to-anchor distance, the displacement moves towards the edges which is beneficial in maintaining the same gap for constant pull-in voltages.

As shown in Fig. 5.2, the switch displacement under 0.5 mN force has been simulated using Coventorware. The displacement is almost the same for both 27°C and 180°C which shows almost the same spring constant. This will minimize the effect of the spring constant variation on the switch activation voltage which will increase the temperature range operation.

In order to simulate the switch behavior under RF power, the switch is first simulated using an EM simulator (Sonnet) to find the current distribution and the amount of heat dissipated. The equivalent heater is replaced in the current concentration areas with appropriate heat generation to find the temperature increase in the membrane as described in Chapter 2.

5.2.2 RF Power Analysis

The effect of the displacement as a function of temperature is shown in Fig. 5.3. The current distribution is shown in Fig. 5.4. The current is mostly concentrated in the

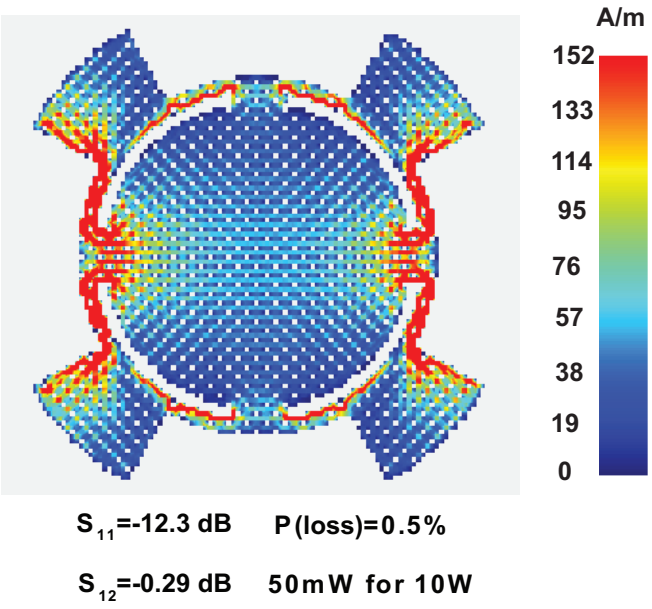

Figure 5.4: Simulated current distribution on the beam.

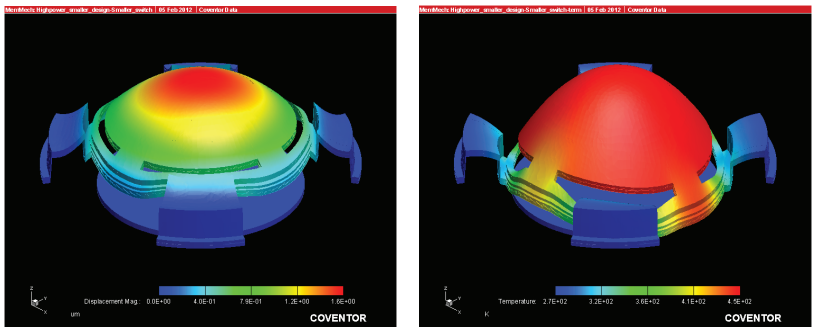

Figure 5.5: Simulated temperate profile of the beam.

input and output edges. The simulated S-parameters show that almost 0.5% of the power is dissipated in the membrane at 10 GHz. The switch has been simulated for different input power values and the resulting temperature profile of the switch for the case of P_{in}=10 W is shown in Fig. 5.5. The center part of the beam has the highest temperature and the only heat dissipation mechanism is through the narrow section behind the cutout to the anchors. By increasing this distance and also using a thicker beam the effective thermal resistivity of the switch is smaller and results in a lower temperature increase. A temperature increase of 180°C only moves the beam 0.2 μm upward which is less than 10% of the total gap.

5.3 Fabrication

The capacitive switches are fabricated on a 250 μm alumina substrate. First, 0.5 μm of sputtered gold is deposited to form the bottom electrode. Then, 0.28 μm of Si_3N_4 is sputtered for the dielectric formation. A 3 μm polyamide is used for the sacrificial layer and the aluminum membrane was deposited. The CPW lines were electroplated to a thickness of 2.7 μm and the switch is then released using dry etching techniques (Fig. 5.6).

5.4 Circuit Configurations

5.4.1 SPST Switch

The proposed switch was used as a building block of several circuits. The first circuit is a simple SPST switch (Fig. 5.7). The switch capacitance is determined after an SOLT calibration to the probe tips and by fitting the measured S-parameters to a transmission-line based on CLR switch model. The extracted capacitances are Cu = 0.05 pF and Cd = 1.8 pF at 30 V (Cr = 36). S-parameters measurements show that the switch can provide an isolation of 10 dB at 10 GHz (Fig. 5.8). The measured switch actuation voltage is ∼30 V and the release voltage is ∼10 V. Since the release voltage is relatively low, this switch can only be used for cold switching conditions i.e. when the RF power is OFF during switching.

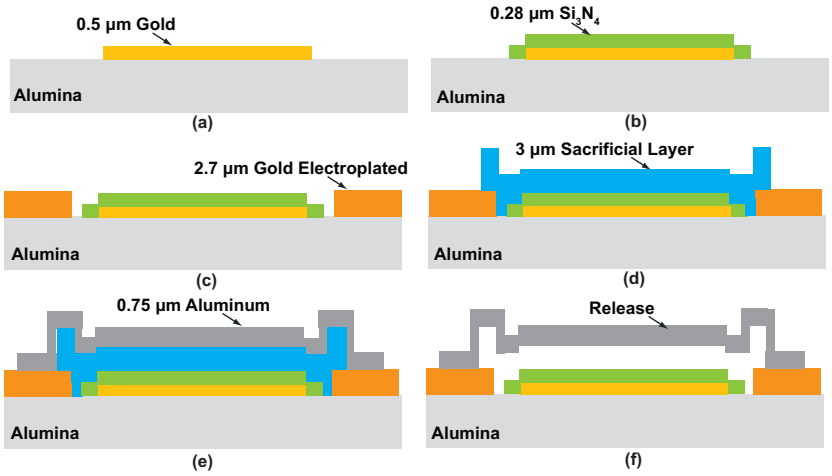

Figure 5.6: Raytheon fabrication process.

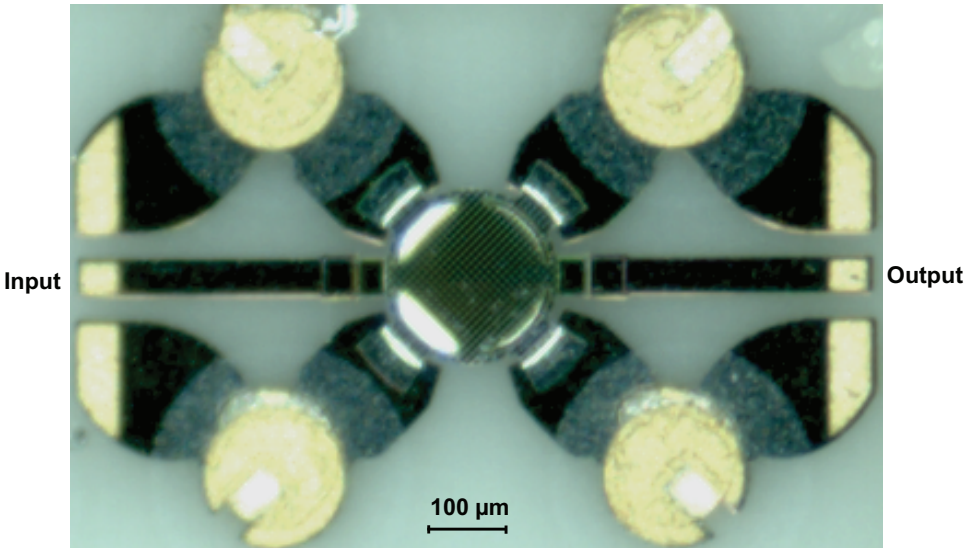

Figure 5.7: Micrograph of the SPST capacitive switch using the Raytheon process.

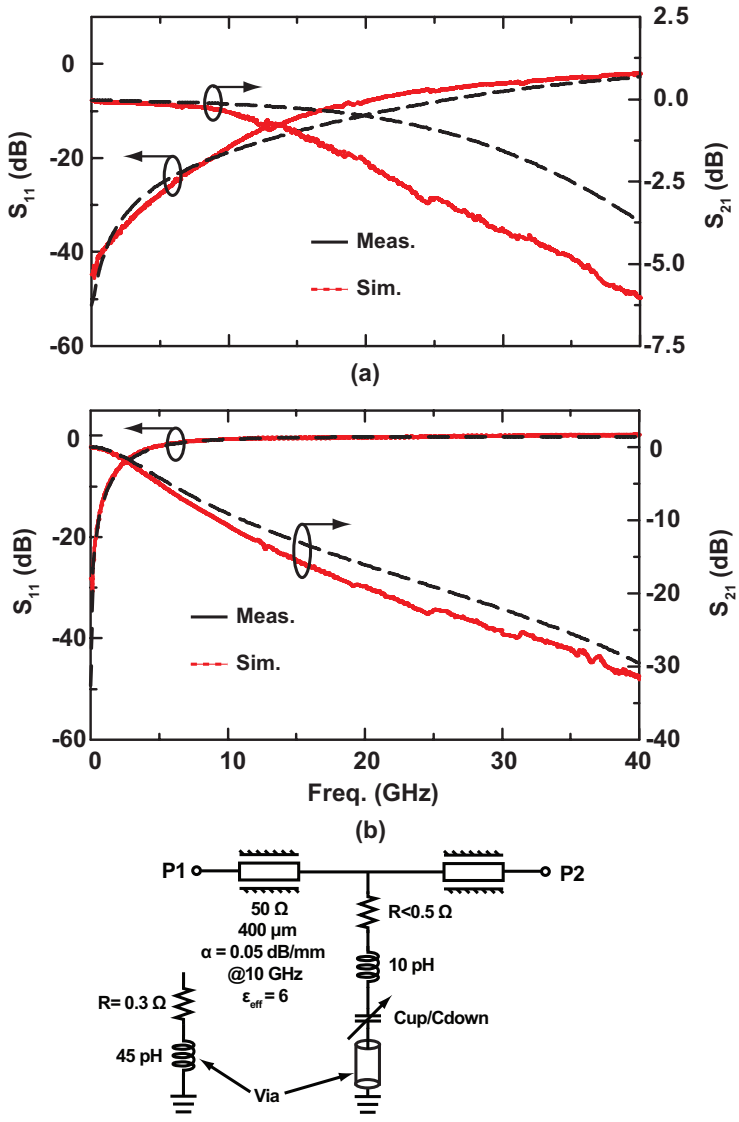

Figure 5.8: S-parameter measurements and simulation of the SPST capacitive switch.

5.4.2 SPDT Switch

The next circuit is the SPDT switch which is designed at a center frequency of 10 GHz (Fig. 5.9). The SPDT equivalent circuit is shown in Fig. 5.10. There are two MIM capacitors in the design of the SPDT switch which are used to isolate the two switches for biasing. There are also two $\lambda/4$ transmission lines in each section to provide an open circuit when the switch is down (short) to the other port. Fig. 5.11 shows the S-parameters simulation and measurement of the SPDT switch. Measurements show an isolation of $>$ 10 dB from 8-12 GHz and an insertion loss of $\sim$0.5 dB. The reason for the shifted frequency is that in the simulations the effective dielectric constant was assumed to be $\sim$3 instead of the nominal value of 7 which is the typical value for Si_3N_4. This lower dielectric constant is due to the dielectric roughness. The effective relative dielectric constant value was found to be between 1-2 which is lower than the simulated values and this causes the shift in center frequency.

5.5 Double-Series Switches

5.5.1 SPST Switches

Another way to improve the performance of the capacitive MEMS switches is through cascading them in a series configuration which divides the effective RMS voltage across them. The only downside of this approach is reducing the effective down-state capacitance by two. In order to increase the capacitance in the down-state position, two series switches can be placed in a shunt configurations as shown in Fig. 5.12. The S-parameters of the SPST double series switch is shown in Fig. 5.13 along with simulations.

5.5.2 SPDT Switches

The double series switch has also implemented in a SPDT configuration as shown in Fig. 5.14. The S-parameter were measured from 8-12 GHz and show an isolation $>$20 dB at the centner frequency and an insertion loss of $\sim$0.5 dB (Fig. 5.15). Again the shift in the design frequency is due to the lower effective dielectric constant of the Si_3N_4. The equivalent circuit model of the double series SPDT switch is similar to Fig. 5.10 except that there is no MIM capacitance included.

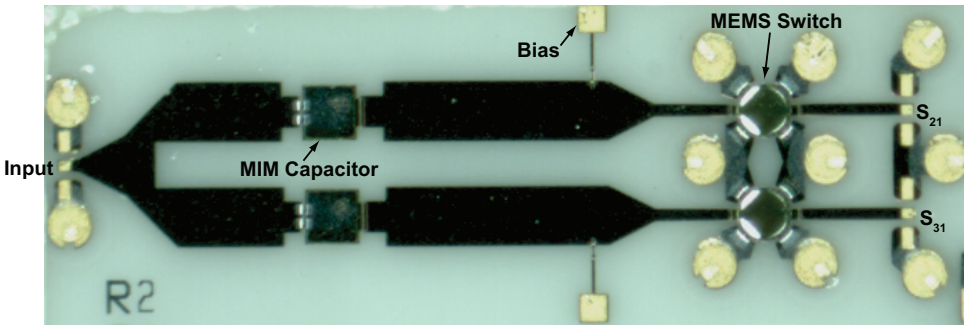

Figure 5.9: Micrograph of the SPDT capacitive switch using Raytheon process.

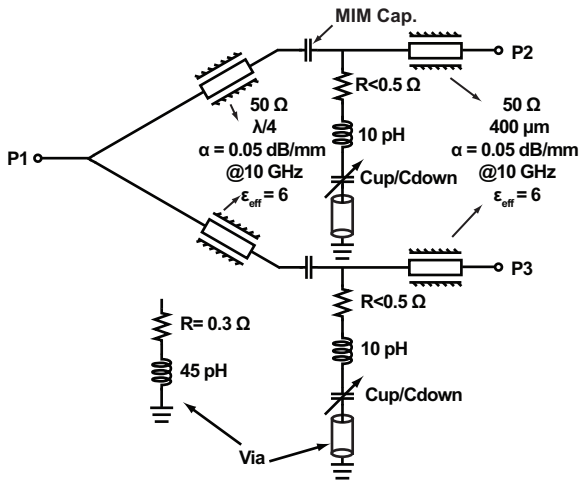

Figure 5.10: SPDT switch equivalent circuit model.

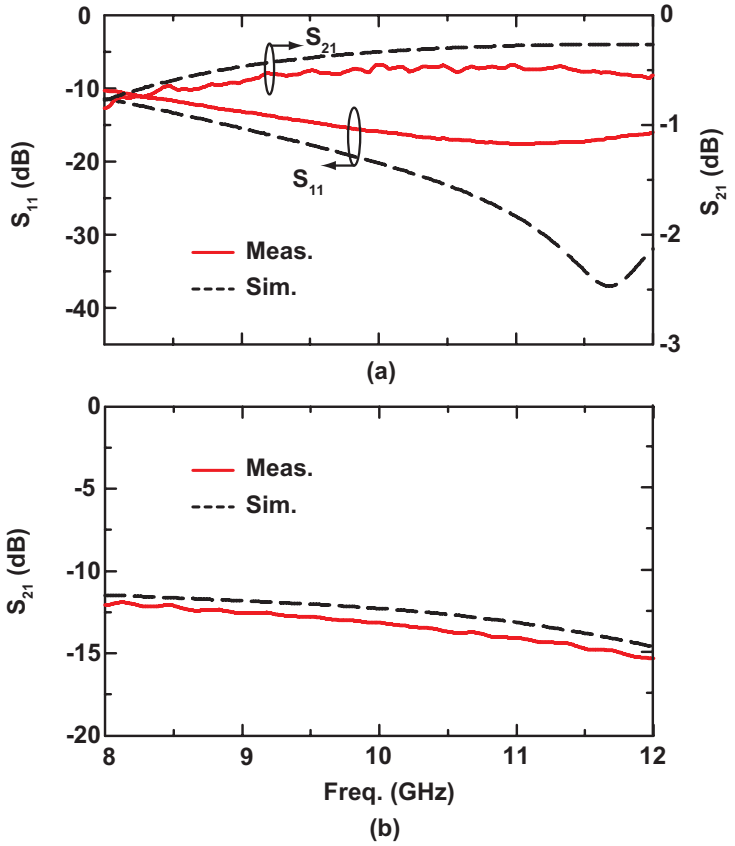

Figure 5.11: S-parameter measurements and simulation of the SPDT capacitive switch. (a) switch is ON, (b) switch is OFF.

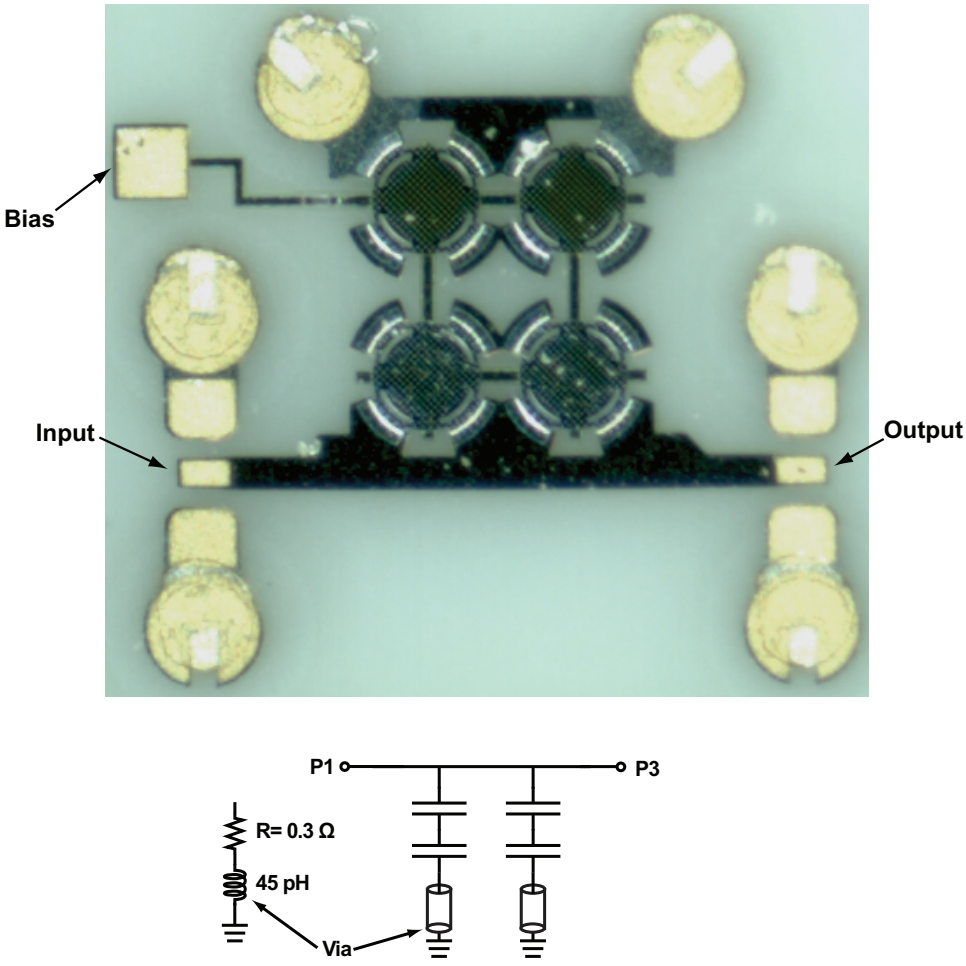

Figure 5.12: The micrograph of the double-series SPST switch.

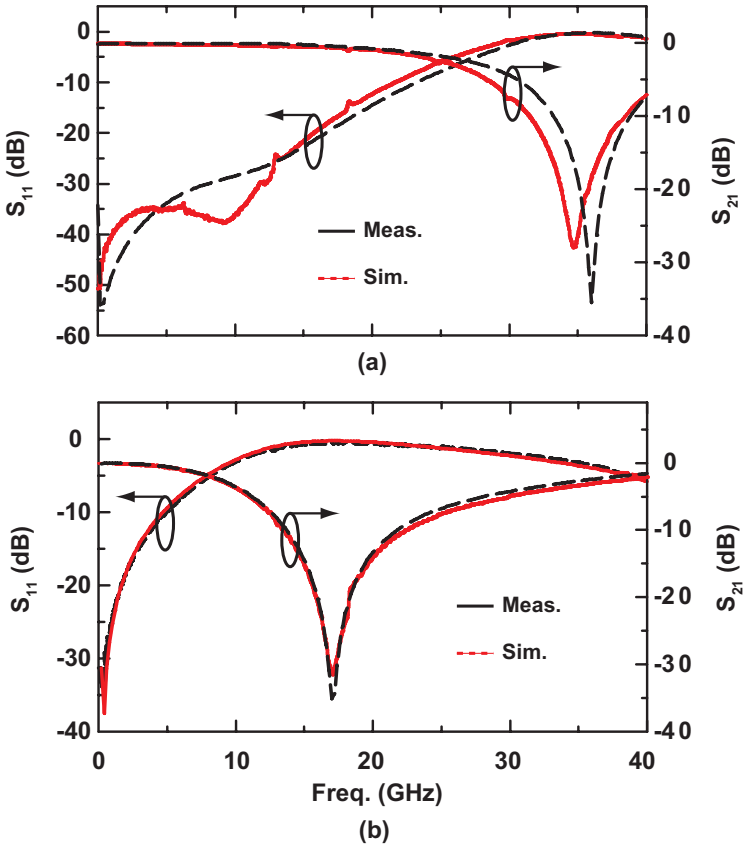

Figure 5.13: S-parameter measurements and simulations of the double-series SPST switch. (a) switch is ON, (b) switch is OFF.

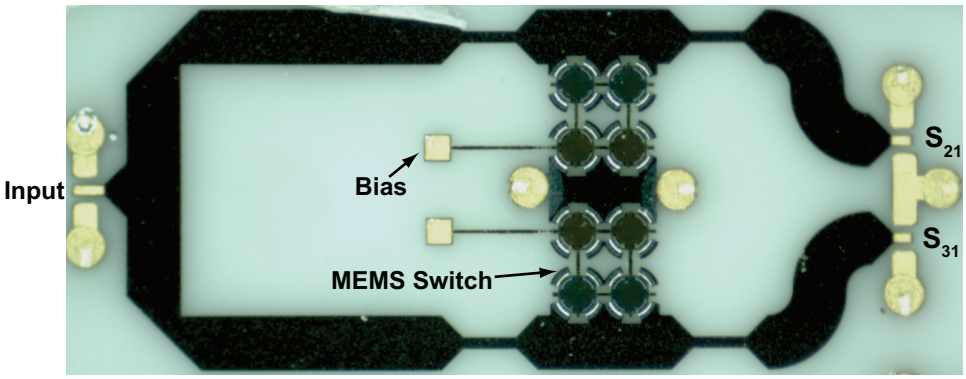

Figure 5.14: Micrograph of the double-series SPDT switch using Raytheon process.

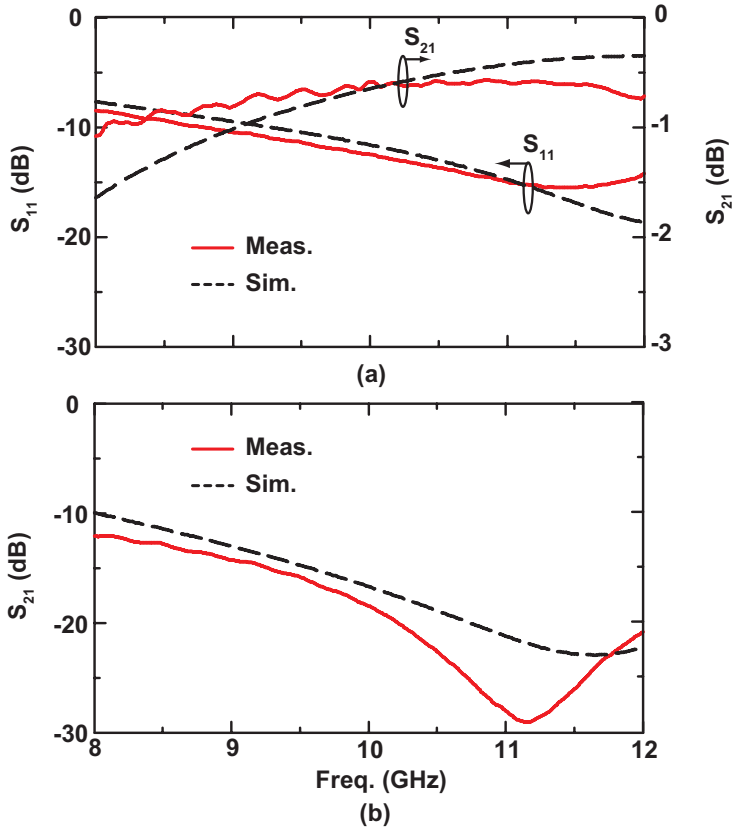

Figure 5.15: S-parameter measurements and simulation of the double series SPDT switch. (a) switch is ON, (b) switch is OFF.

5.5.3 Phase Shifter

Capacitive MEMS switches can be used to implement high-performance phase shifters. The double-series switches were used to form a 2-bit phase shifter from 8-12 GHZ (Fig. 5.16). The lange coupler was designed of a center frequency of 10 GHz along with three switched capacitor tanks to implement four different states. The equivalent circuit model of the 2-bit X-band phase shifter is shown in Fig. 5.17. Fig. 5.18 shows the different phase states and the resulting RMS phase error. The measured insertion loss shows an average loss of 1.5 dB and a return loss $> \sim$10 dB (Fig. 5.19) [56].

5.6 Acknowledgments

Chapter 5 in part is currently being prepared for submission to the IEEE Microwave and Wireless Components Letters, 2014; Hosein Zareie and Gabriel M. Rebeiz. The dissertation author is the primary author of this material.

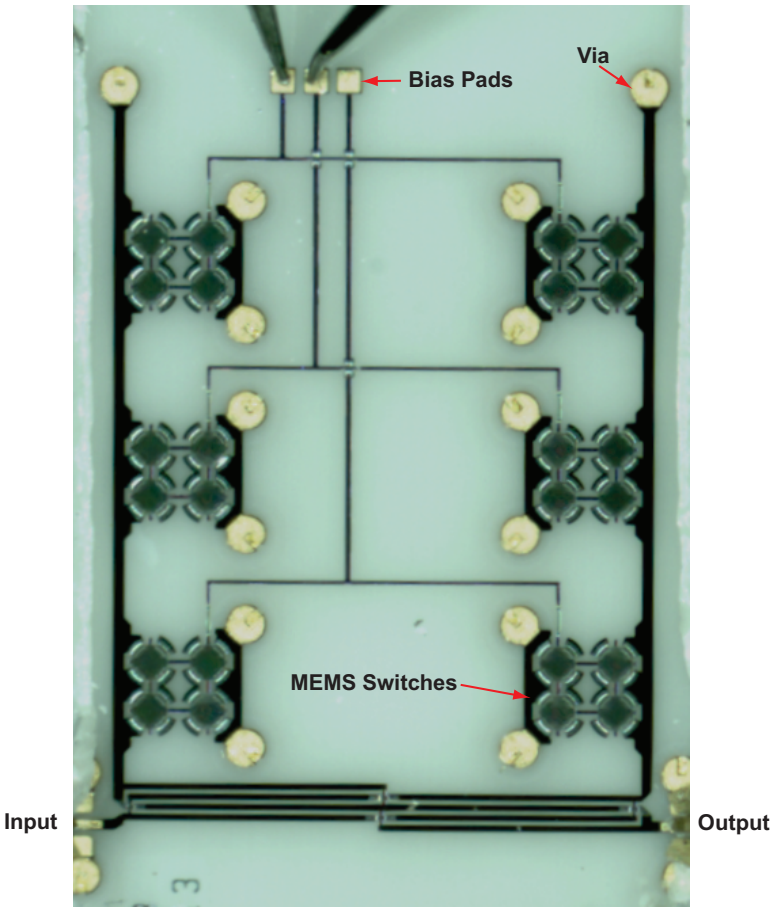

Figure 5.16: The micrograph of the 2-bit phase shifter using the double series capacitive MEMS switches.

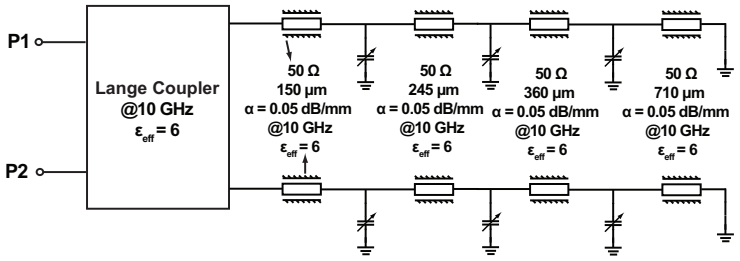

Figure 5.17: 2-bit phase shifter equivalent circuit model.

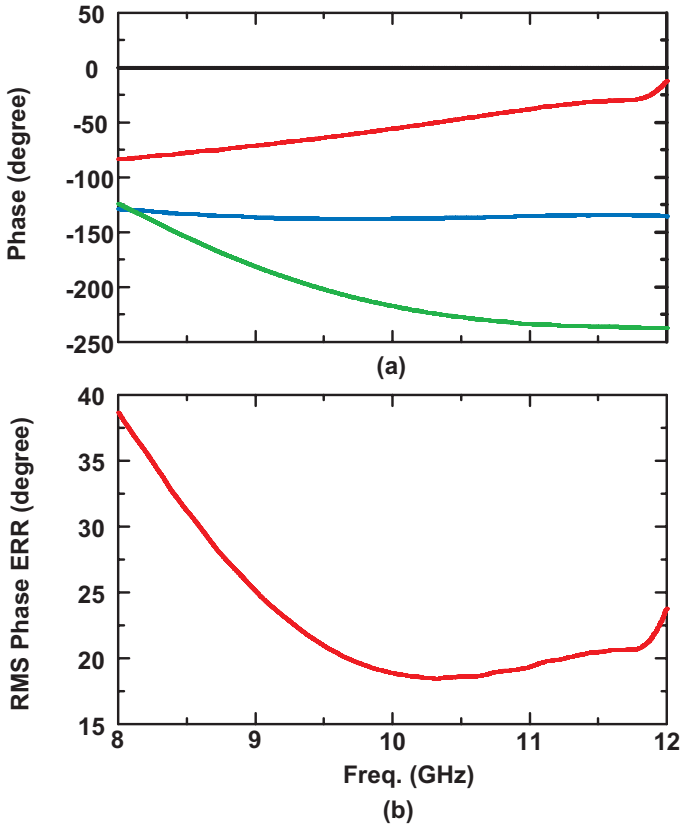

Figure 5.18: (a) The normalized phase measurements and (b) the effective RMS phase error of the 2-bit X-band phase shifter.

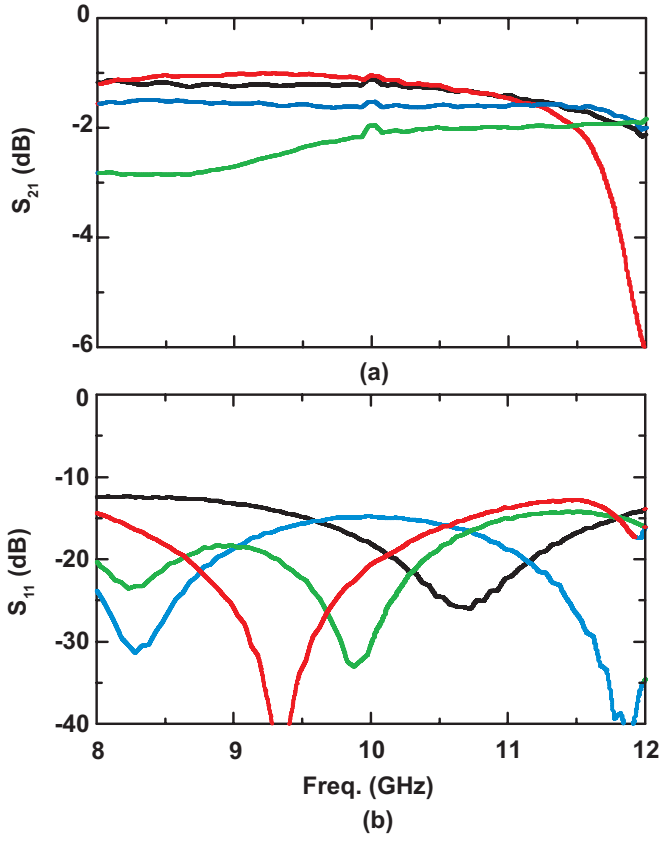

Figure 5.19: S-parameter measurements of the 2-bit X-band phase shifter: (a) insertion loss, (b) return loss.

Chapter 6

Conclusion and Future Work

6.1 Summary

This thesis represents the design and fabrication of high performance RF MEMS switches. Both capacitive switches and metal contact switches were presented with high power handling capability.

Chapter 2 represents the design and characterization of a high-power RF MEMS switched capacitor. The switch is based on a 4 μm-thick metal plate and four symmetrical springs. The design has low sensitivity to residual stress and stress gradients. S-parameter measurements result in C_u=0.01 pF, C_d=0.63 pF (C_r=6.3), a power handling $>$ 10 W using hot switching conditions, and a switching time of $\sim$20 μs. The pull-down voltage (Vp = 50-55 V) and release voltage (Vr = 25-30 V) are stable to +/-4 V over 25-125°C. The design can be arrayed for N-bit switched-capacitor networks. Applications areas are in high power phase shifters and tunable filters.

Chapter 3 presents an RF MEMS switched capacitor which has low sensitivity to both in-plane stress and stress gradients. The membrane uses a central joint to minimize the effect of stress gradient. The switch is fabricated using 4.5 μm gold electroplated membrane and a 3 μm gap. Dimples with a thickness of 0.3 μm are used to result in an air dielectric in the down-state position and this greatly improves the reliability, while still maintaining a measured capacitance ratio of 5.0. The switch is capable of handling high RF power $>$ 12 W under hot switching condition, as well as having low sensitivity to temperature variations (20mV/°C). The application areas are in high power reconfigurable filters, matching networks and antennas for modern communication systems.

Chapter 4 presents the design and characterization of compact, high power RF MEMS SPST and SP4T metal-contact switches. The SPST design results in a contact force of 1.9-2.8 mN at 80-90 V distributed over 8-contacts and using four independent quadrants for actuation. The SP4T is a derivative of the SPST and results in a contact force of 0.45-0.7 mN per switch at 80-90 V. S-parameter measurements show an up-state capacitance of 70 fF and 17 fF along with a down-state resistance of 1-2 Ω and 2-4 Ω using a Au-to-Ru contacts for the SPST and SP4T switches, respectively. The switch pull-in and release voltages are 50 V and 45 V, respectively, and the switching time is $t_{on} \sim 10$ μs and $t_{off} \sim 2$ μm. The SPST and SP4T are capable of handling 10 W and 2 W up to 100 million cycles, and the SPST has been tested with 30 W of power up to 30 million cycles before failure (all cold switched). The application areas are in compact high-power applications such as wireless communication systems and base-stations.

Chapter 5 presents the design and fabrication of a high performance capacitive switches using a thin metal process. The switch is used in different circuit configurations and the design can handle high temperature increase in the beam which is advantageous for high power applications.

6.2 Future Work

The reliability of the RF MEMS capacitive switches is important in order to commercialize them. RF MEMS capacitive switches suffer from dielectric charging which can be minimized using dimples in the down-state position and also lowering their actuation voltages by increasing the device size. The dimples can be separated from the bottom electrode to further improve the dielectric charging. Also other materials such as aluminium or nickel can be used instead of the gold to improve the creep behavior of the capacitive switch. Packaging of RF MEMS capacitive switches will improve their performance and reliability. The degradation due to humidity and contamination in RF MEMS capacitive switches can be reduced using packages.

RF MEMS metal-contact switches also should be packaged for better performances and reliability. The effect of humidity and contamination which increase the contact resistance in metal-contact switches can be reduced using hermetic packages. These devices can be made with hard metals in order to improve their power handling and prevent them from stiction in the down-state position. Both the top and bottom contacts can be made of hard metals such as ruthenium for better power handling.

Metal-contact switches can be made smaller both in size and beam thickness while adding more switches in parallel to maintain their RF power handling so that they become compatible with the CMOS top metal processes [57, 58]. The SPST design can be made more reliable by increasing the number of parallel contacts and also the circular membrane can be divided into N separate sections each with its own actuation electrode to make very compact SPNT switches.

Bibliography

[1] G. M. Rebeiz, *MEMS: Theory, Design and Technology.* Wiley, New Jersey, 2003.

[2] P. M. Zavracky, N. E. McGruer, R. H. Morrison and D. Potter, "Microswitches and mircorelays with a view toward microwave applications," *Int. J. RF Microw. Comput.-Aided Eng.*, vol. 9, no. 4, pp. 338–347, 1999.

[3] R. E. Mihailovich, M. Kim, J. B. Hacker, E. A. Sovero, J. Studer, J. A. Higgins, J. F. DeNatale, "MEM relay for reconfigurable RF circuits," *IEEE Microwave and Wireless Components Letters*, vol. 11, no. 2, pp. 53–55.

[4] Harvey S. Newman, J. L. Ebel, D. Judy and John Maciel, "Lifetime Measurements on a High-Reliability RF-MEMS Contact Switch," *IEEE Microwave and Wireless Components Letters*, vol. 18, no. 2, pp. 100–102, Feb. 2008.

[5] James Lampen, S. Majumder, Ji Chilyoung and John Maciel, "Low-loss, MEMS based, broadband phase shifters," *IEEE International Symposium on Phased Array Systems and Technology*, pp. 219–224, Oct. 2010.

[6] W. N. Allen and D. Peroulis, "Three-Bit and Six-Bit Tunable Matching Networks with Tapered Lines," *IEEE Topical Meeting on Silicon Monolithic Integrated Circuits in RF Systems*, pp. 1–4, Jan. 2009.

[7] G. H. Huff and J. T. Bernhard, "Integration of packaged RF MEMS switches with radiation pattern reconfigurable square spiral microstrip antennas," *IEEE Transactions on Antennas and Propagation*, vol. 54, no. 2, pp. 464–469, Feb. 2006.

[8] M. Daneshmand, A. A. Fomani, M. M. Fahmi, J. A. Ruiz-Cruz and R. R. Mansour, "MEMS multiport switches and switch matrices for satellite applications," *IEEE MTT-S International Microwave Symposium Digest*, pp. 1–3, June 2012.

[9] S. Majumder, J. Lampen, R. Morrison and J. Maciel, "A packaged, high-lifetime ohmic MEMS RF switch," *IEEE MTT-S International Microwave Symposium Digest*, vol. 3, pp. 1935–1938, June 2003.

[10] T. Fujiwara, T. Seki, F. Sato and M. Oba, "Development of RF-MEMS ohmic contact switch for mobile handsets applications," *European Microwave Conference (EuMC)*, pp. 180–183, Oct. 2012.

[11] H. Sedaghat-Pisheh and G. M. Rebeiz, "Variable spring constant, high contact force RF MEMS switch," *IEEE MTT-S International Microwave Symposium Digest*, pp. 304–307, May 2010.

[12] C. D. Patel and G. M. Rebeiz, "A High-Reliability High-Linearity High-Power RF MEMS Metal-Contact Switch for DC-40-GHz Applications," *IEEE Transactions on Microwave Theory and Techniques*, vol. 60, no. 10, pp. 3096–3112, Oct. 2012.

[13] C. D. Patel and G. M. Rebeiz, "RF MEMS Metal-Contact Switches With mN-Contact and Restoring Forces and Low Process Sensitivity," *IEEE Transactions on Microwave Theory and Techniques*, vol. 59, no. 5, pp. 1230–1237, May 2011.

[14] D. A. Czaplewski, C. D. Nordquist, G. A. Patrizi, G. M. Kraus and W. D. Cowan, "RF MEMS Switches With RuO2 - Au Contacts Cycled to 10 Billion Cycles," *Journal of Microelectromechanical Systems*, vol. 22, no. 3, pp. 655–661, June 2013.

[15] Wang Ye, Li Zhihong, D. T. McCormick and N. C. Tien, "A low-voltage lateral MEMS switch with high RF performance," *Journal of Microelectromechanical Systems*, vol. 13, no. 6, pp. 902–911, Dec. 2004.

[16] A. Menz and R. Hoper, "Micromechanical silicon RF switch with electroplated solid contacts for high reliability," *European Microwave Integrated Circuits Conference (EuMIC)*, pp. 453–456, Oct. 2012.

[17] F. Barriere, A. Pothier, A. Crunteanu, M. Chatras and P. Blondy, "A zero-level packaged RF-MEMS switch with large contact force," *European Microwave Integrated Circuits Conference (EuMIC)*, pp. 1229–1232, Oct. 2011.

[18] R. Goggin, J. E. Wong, B. Hecht, P. Fitzgerald and M. Schirmer, "Fully integrated, high yielding, high reliability DC contact MEMS switch technology & control IC in standard plastic packages," *IEEE Sensors*, pp. 958–961, Oct. 2011.

[19] M. Sterner, N. Roxhed, G. Stemme and J. Oberhammer, "Static Zero-Power-Consumption Coplanar Waveguide Embedded DC-to-RF Metal-Contact MEMS Switches in Two-Port and Three-Port Configuration," *IEEE Transactions on Electron Devices*, vol. 57, no. 7, pp. 1659–1669, July 2010.

[20] H. Sedaghat-Pisheh, Kim Jung Mu and G. M. Rebeiz, "A Novel Stress-Gradient-Robust Metal-Contact Switch," *IEEE International Conference on Micro Electro Mechanical Systems*, pp. 27–30, Jan. 2009.

[21] C. Goldsmith, J. Ehmke, A. Malczewski, B. Pillans, S. Eshelman, Z. Yao, J. Brank, and M. Eberly, "Lifetime characterization of capacitive RF MEMS switches," *IEEE MTT-S Int. Microwave Symp. Dig.*, pp. 227–230, June 2001.

[22] G. M. Rebeiz, K. Entesari, I.C. Reines, S.J. Park, M.A. El-Tanani, A. Grichener and A. R. Brown, "Tuning in to RF MEMS," *IEEE Microwave Magazine*, vol. 10, no. 5, pp. 55–71, Oct. 2009.

[23] M. Daneshmand and R. Mansour, "RF MEMS Satellite Switch Matrices," *IEEE Microwave Magazine*, pp. 92–109, Aug. 2011.

[24] S.P. Natarajan, S.J. Cunningham, A.S. Morris and D.R. Dereus, "CMOS integrated digital RF MEMS capacitors," *IEEE Silicon Monolithic Integrated Circuits in RF Systems*, pp. 173–176, Jan. 2011.

[25] K. Kuwabara, N. Sato, T. Shimamura, H. Morimura, J. Kodate, T. Sakata, S. Shigematsu, K. Kudou, K. Machida, M. Nakanishi, H. Ishii, "RF CMOS-MEMS switch with low-voltage operation for single-chip RF LSIs," *IEDM Tech. Dig.*, pp. 1–4, 2006.

[26] V. Joshi, Khieu Cong, C.G. Smith, C. Schepens, F. Csaszar, D. Lacey, T. Nagata, M. Renault, R. Van Kampen, R. Knipe, D. Yost, "A CMOS compatible back end MEMS switch for logic functions," *Proc. International Interconnect Technology Conference*, pp. 1–3, June 2010.

[27] J. Reinke, G.K. Fedder, T. Mukherjee, "CMOS-MEMS 3-bit Digital Capacitors With Tuning Ratios Greater Than 60:1," *IEEE Trans. on Microwave Theory and Techniques*, vol. 59, no. 5, pp. 1238–1248, May 2011.

[28] S. Fouladi and R. Mansour, "Capacitive RF MEMS Switches Fabricated in Standard 0.35-μm CMOS Technology," *IEEE Trans. on Microwave Theory and Techniques*, vol. 58, no. 2, pp. 478–486, Feb. 2010.

[29] B. Pillans, J. Kleber, C. Goldsmith, M. Eberly, "RF power handling of capacitive RF MEMS devices," *IEEE MTT-S Int. Microwave Symp. Dig.*, vol. 1, pp. 329–332, 2002.

[30] J.R. Reid, L.A. Starman and R.T. Webster, "RF actuation of capacitive MEMS switches," *IEEE MTT-S Int. Microwave Symp. Dig.*, vol. 3, pp. 1919–1922, June 2003.

[31] J.B. Rizk, E. Chaiban and G.M. Rebeiz, "Steady state thermal analysis and high-power reliability considerations of RF MEMS capacitive switches," *IEEE MTT-S Int. Microwave Symp. Dig.*, vol. 1, pp. 239–242, June 2002.

[32] I. Reines and G. Rebeiz, "A Robust High Power-Handling ($>$ 10 W) RF MEMS Switched Capacitor," *IEEE MEMS*, pp. 764–767, Jan. 2011.

[33] D. Peroulis, S. P. Pacheco and L.P.B. Katehi, "RF MEMS switches with enhanced power-handling capabilities," *IEEE Trans. on Microwave Theory and Techniques*, vol. 52, pp. 59–68, Jan. 2004.

[34] H. Sedaghat-Pisheh, R. Mahameed and G. M. Rebeiz, "RF MEMS miniature-switched capacitors with pull-down and pull-up electrodes for high power applications," *IEEE MTT-S Int. Microwave Symp.*, pp. 1–4, June 2011.

[35] J.D. Martinez, P. Blondy, A. Pothier, D. Bouyge, A. Crunteanu and M. Chatras, "Surface and bulk micromachined RF MEMS capacitive series switch for watt-range hot switching operation," *European Microwave Conference*, pp. 1237–1240, Oct. 2007.

[36] J. Muldavin, C.O. Bozler, S. Rabe, P.W. Wyatt and C.L. Keast, "Wafer-Scale Packaged RF Microelectromechanical Switches," *IEEE Trans. on Microwave Theory and Techniques*, vol. 56, no. 2, pp. 522–529, Feb. 2008.

[37] H. Yamazaki, T. Ikehashi, T. Saito, E. Ogawa, T. Masunaga, T. Ohguro, Y. Sugizaki and H. Shibata, "A high power-handling RF MEMS tunable capacitor using quadruple series capacitor structure," *IEEE MTT-S Int. Microwave Symp. Dig.*, pp. 1138–1141, May 2010.

[38] R. Mahameed and G. M. Rebeiz, "A High-Power Temperature-Stable Electrostatic RF MEMS Capacitive Switch Based on a Thermal Buckle-Beam Design," *IEEE J. MEMS*, vol. 19, pp. 816–826, Aug. 2010.

[39] C. Palego, A. Pothier, T. Gasseling, A. Crunteanu, C. Cibert, C. Champeaux, P. Tristant, A. Catherinot and P. Blondy, "RF-MEMS Switched Varactor for High Power Applications," *IEEE MTT-S Int. Microwave Symp. Dig.*, pp. 35–38, June 2006.

[40] M. A. El-Tanani and G. M. Rebeiz, "High Performance 1.5-2.5 GHz RF MEMS Tunable Filters for Wireless Applications," *IEEE Trans. on Microwave Theory and Techniques*, vol. 58, no. 6, pp. 1629–1637, June 2010.

[41] C. W. Baek, Y. K. Kim, Y. Ahn, and Y. H. Kim, "Measurement of the mechanical properties of electroplated gold thin films using micromachined beam structures," *Sens. Actuators A: Physical*, vol. 117, pp. 17–27, 2005.

[42] I. Reines, B. Pillans and G. M. Rebeiz, "Thin-Film Aluminum RF MEMS Switched Capacitors with Stress-Tolerance and Temperature-Stability," *IEEE J. MEMS*, vol. 20, no. 1, pp. 193–203, Feb. 2011.

[43] Sonnet version 12.52, Sonnet Software Inc., Syracuse NY, 1986-2012.

[44] Coventorwaretm 2010, http://www.coventor.com.

[45] R.W. Herfst, H.G.A. Huizing, P.G. Steeneken and J. Schmitz, "Characterization of dielectric charging in RF MEMS capacitive switches," *IEEE International Conference on Microelectronic Test Structures*, pp. 133–136, March 2006.

[46] X. Yuan, J. C. M. Hwang, D. Forehand and C. L. Goldsmith, "Modeling and characterization of dielectric-charging effects in RF MEMS capacitive switches," *IEEE MTT-S Int. Microwave Symp. Dig.*, pp. 753–756, June 2005.

[47] MATLAB version 7.14.0.739 Natick, Massachusetts: The MathWorks Inc., 2012a.

[48] D. Mardivirin, A. Pothier, A. Crunteanu, B. Vialle and P. Blondy, "Chargin in dielectricless capacitive RF-MEMS switches," *IEEE Trans. on Microwave Theory and Techniques*, vol. 57, no. 1, pp. 231–236, Jan. 2009.

[49] A. Grichener and G. M. Rebeiz, "High-Reliability RF-MEMS Switched Capacitors With Digital and Analog Tuning Characteristics," *IEEE Trans. on Microwave Theory and Techniques*, vol. 58, pp. 2692–2701, Oct. 2010.

[50] D. Molinero, C. Palego, S. Halder, X. Luo, A. Hallden-Abberton, J.C. Hwang and C.L. Goldsmith, "Acceleration of dielectric charging/discharging by RF power in microelectromechanical capacitive switches," *IEEE MTT-S Int. Microwave Symp.*, pp. 1–4, June 2011.

[51] Hsu Hao-Han, M. Koslowski and D. Peroulis, "An Experimental and Theoretical Investigation of Creep in Ultrafine Crystalline Nickel RF-MEMS Devices," *IEEE Trans. on Microwave Theory and Techniques*, vol. 59, no. 10, pp. 2655–2664, Oct. 2011.

[52] H. Zareie and G.M. Rebeiz,, "High-Power RF MEMS Switched Capacitors Using a Thick Metal Process," *IEEE Transactions on Microwave Theory and Techniques*, vol. 61, no. 1, pp. 455–463, J1n. 2013.

[53] J. K. Luo, M. Pritschow, A. J. Flewitt, S. M. Spearing, N. A. Fleck, and W. I. Milne, "Effects of Process Conditions on Properties of Electroplated Ni Thin Films for Microsystem Applications," *Journal of Electrochemical Society*, vol. 153, pp. 155–161, Jan. 2006.

[54] P. Zhen, C. Palego, J.C.M. Hwang, C. Moody, A. Malczewski, B.W. Pillans, D.I. Forehand and C.L. Goldsmith, "Effect of packaging on dielectric charging in RF MEMS capacitive switches," *IEEE MTT-S Int. Microwave Symp.*, pp. 1637–1640, June 2009.

[55] P. Zhen, C. Palego, J. Hwang, D.I. Forehand, C.L. Goldsmith, Cody Moody, Andrew Malczewski, B.W. Pillans, R. Daigler, J. Papapolymerou, "Impact of Humidity on Dielectric Charging in RF MEMS Capacitive Switches," *IEEE Microwave and Wireless Components Letters*, vol. 19, pp. 299–301, May 2009.

[56] A. Malczewski, S. Eshelman, B. Pillans, J. Ehmke, C.L. Goldsmith, "X-band RF MEMS phase shifters for phased array applications," *IEEE Microwave and Guided Wave Letters*, vol. 19, no. 12, pp. 517–519, Dec. 1999.

[57] Chenhui Niu and Gabriel M Rebeiz, "A miniature RF MEMS metal-contact switch with high biaxial and stress-gradient tolerance," *IEEE MTT-S International Microwave Symposium Digest*, pp. 1–3, June 2012.

[58] R. Stefanini, M. Chatras, P. Blondy, G.M. Rebeiz, "Miniature MEMS Switches for RF Applications," *Journal of Microelectromechanical Systems*, vol. 20, no. 6, pp. 1324–1335, Dec. 2011.